

Manufacturing Effects on Electromagnetic Properties of Ferromagnetic Cores in Electrical Machines

Andries Daem

Doctoral dissertation submitted to obtain the academic degree of
Doctor of Electromechanical Engineering Technology

Supervisors

Prof. Peter Sergeant, PhD - Prof. Luc Dupré, PhD

Department of Electromechanical, Systems and Metal Engineering
Faculty of Engineering and Architecture, Ghent University

March 2021

ISBN 978-94-6355-471-8

NUR 959, 971

Wettelijk depot: D/2021/10.500/19

Members of the Examination Board

Chair

Honoray prof. Ronny Verhoeven, PhD, Ghent University

Other members entitled to vote

Nele De Geeter, PhD, Ghent University

Mohamed Nabil Fathy Ibrahim, PhD, Ghent University

Prof. Leo Kestens, PhD, Ghent University

Prof. Elena Lomonova, PhD, Technische Universiteit Eindhoven, the Netherlands

Ruud Sprangers, PhD, Punch Powertrain

Supervisors

Prof. Peter Sergeant, PhD, Ghent University

Prof. Luc Dupré, PhD, Ghent University

Prologue

Word of thanks

The work that culminated in this thesis was carried out primarily in the EELab research group in the Department of Electromechanical, Systems and Metal Engineering at Ghent University. During the four years I have spent working on this research topic, I could always count on my supportive supervisors prof. Peter Sergeant and prof. Luc Dupré. They provided me with the guidance and creative autonomy for completing this project. To the PhD jury, I would like to mention that I really appreciate your efforts for reviewing my work. Thank you for pushing me to go the necessary extra mile. I thank my colleagues at the Eindhoven University of Technology, especially Reza and prof. Elena Lomonova, with whom I collaborated closely to maintain focus on our common research goals. I also had the pleasure to work together with the research group of Electromechanics at Aalto University. I will never forget the insightful discussions and fun times I had collaborating with Ravi and the rest of his group. Thanks Vincent, Tony and Marilyn for your crucial support in getting things done. When times were challenging, I found support in my dear colleagues of Building 131. A special mention of gratitude to my close colleagues - in the office and in our lab - for creating such an enjoyable, relaxing and inspiring working atmosphere. I would like to finish by stating that this thesis would never have been realized without the unwavering and implicit support of my family. Especially to Sara, I want to say that I could not imagine a more patient and comforting life companion. Also, thanks to covid19 and my cat, for unintentionally forcing me to stay focused and keeping me company while working from home, respectively.

Andries Daem, 2021

Contents

Samenvatting	vii
Summary	xi
List of Abbreviations	xv
List of Symbols	xvii
List of Publications	xxi
1 Introduction	3
1.1 Design of Electrical Machines	3
1.2 Manufacturing of Electrical Machine Cores	5
1.2.1 Electrical Steel	5
1.2.2 Shaping	8
1.2.3 Joining	12
1.2.4 Stress Relief Annealing	17
1.3 Efficiency of electrical machines	18
2 Modelling of Magnetic Materials	21
2.1 Domain Theory	22
2.1.1 Energy from externally applied field	22
2.1.2 Anisotropic Energy	23
2.1.3 Domain Wall Energy	23
2.1.4 Magnetostatic Energy	23
2.1.5 Magnetoelastic Energy	23
2.2 Hysteresis in ferromagnetic materials	24
2.2.1 Hysteresis Loop	24
2.2.2 Single Valued BH curve	27
2.2.3 3 Parameter <i>BH</i> curve model	27
2.3 Statistical Loss Theory	29
2.3.1 Hysteresis Loss	31
2.3.2 Classical Loss	32
2.3.3 Excess Loss	33

2.3.4	Loss Modelling	34
2.4	Magnetic Measurements	35
2.4.1	Basic Principles for Magnetic Measurements	36
2.4.2	Epstein Frame Method	37
2.4.3	Single Sheet Tester	39
2.4.4	Ring Core Measurements	41
2.4.5	Simplified stator geometries	42
2.5	Inverse Modelling	43
2.6	Machine Modelling Techniques	45
2.6.1	Finite Element Modelling	45
2.6.2	Magnetic Equivalent Circuit	45
2.7	Conclusion	47
3	Measuring the Impact of Manufacturing Effects	49
3.1	Impact of Cutting Technique on Magnetic Properties	49
3.1.1	Cutting effect on NO grade NO27	49
3.1.2	Cutting effect on GO grade M100-23P	50
3.2	Impact of Annealing Process on Magnetic Properties	52
3.3	Impact of Joining Process on Magnetic Properties	53
3.3.1	Effect of Interlocking on NO27	53
3.3.2	Effect of Welding on M400-50A	54
3.4	Conclusion	55
4	Modelling of Manufacturing Effects	59
4.1	Literature review	60
4.1.1	Effects of Cutting	60
4.1.2	Effects of joining	63
4.2	Separation effects in M100-23P GO steel	67
4.2.1	Experimental setup and methodology	68
4.2.2	Measurement results	69
4.2.3	Simulation results	71
4.2.4	YASA machine simulations	72
4.3	Welding effects in M400-50A stator laminations	76
4.3.1	Experimental setup and methodology	77
4.3.2	Measurement results	78
4.3.3	FEM simulation results	81
4.3.4	Full motor measurement results	81
4.4	Interlocking effects in NO27 ring cores	83
4.4.1	Experimental setup and methodology	84
4.4.2	Accuracy and repeatability	84
4.4.3	Core Loss Model	87
4.4.4	Methodology for Modelling Interlocking Effects	87
4.4.5	Interlocking Tool Characterization on NO27	90

4.4.6	Effect of anisotropy	94
4.4.7	Model Validation	95
4.5	Conclusion	98
5	Influence of Stress on Magnetic Properties	101
5.1	Relation between mechanical stress and magnetic properties in literature	102
5.1.1	Parallel stress and magnetic field	102
5.1.2	Stress parallel to stacking direction	104
5.1.3	Multi-axial stress and magnetic field	105
5.2	Magneto-elastic coupling models	106
5.3	Uni-axial measurements and analysis on M270-35A in plastic tensile region	106
5.3.1	Experimental setup and methodology	107
5.3.2	Measurement data	108
5.3.3	Core loss analysis using loss separation	110
5.3.4	Effect of increasing strain on electrical resistivity	117
5.3.5	Microstructural changes in strained electrical steel	118
5.3.6	Discussion	121
5.4	Uni-axial measurements and analysis on M270-35A in elastic tensile region	122
5.4.1	Experimental setup and methodology	122
5.4.2	Measurement Data and analysis	122
5.5	Uni-axial measurements and analysis on M270-35A in elastic compressive region	125
5.6	Effect of stacking stress on core losses of M100-23P	128
5.6.1	Experimental setup and methodology	130
5.6.2	Measurement Data and analysis	130
5.7	Conclusion	133
6	Application of Stress in Manufacturing Effect Models	137
6.1	Magnetomechanical model	138
6.2	Guidelines for Building the Magnetomechanical Model	141
6.3	Application of magnetomechanical model to welding effect models	142
6.3.1	MEC model of welded ring core	143
6.3.2	Coarse-scale stress dependent loss coefficients	145
6.3.3	Local classical loss in weld seam	145
6.3.4	Methodology	146
6.3.5	Case study on M270-35A welded stator core	147
6.3.6	Results	148
6.3.7	Effect of Increasing Weld Radius	148

6.4	Application of magnetomechanical relation to interlocking effect models	150
6.4.1	Case study on NO27 interlocked stator core	151
6.4.2	Effect of number of interlocking points	152
6.5	Conclusion	153
7	General Conclusions and Perspectives	155
7.1	Conclusions	155
7.2	Future Work	158
	Bibliography	161

Samenvatting

Wereldwijd worden steeds strengere CO₂-emissienormen vooropgesteld met als doel de klimaatverandering tegen te gaan en onze afhankelijkheid van niet-hernieuwbare energiebronnen te verminderen. Om deze doelstellingen te halen zijn inspanningen nodig op vele fronten, waaronder het verhogen van de efficiëntie van het elektriciteitsnet. De infrastructuur van het elektriciteitsnet bestaat uit machines en apparatuur voor het opwekken, transporteren, opslaan en verbruiken van elektrische energie. De machines die deze vorm van energie mogelijk maken, kunnen afhankelijk van hun toepassing worden ingedeeld in transformatoren, generatoren of motoren. Deze drie soorten machines worden doorgaans 'elektrische machines' genoemd. Sinds de eerste elektromotor in 1837 werd gepatenteerd door Thomas Davenport, hebben ingenieurs hun ontwerp voortdurend verbeterd en zijn ze erin geslaagd om de efficiëntie van deze machines tot ruim boven 85 % te duwen (voor machines met een nominaal vermogen van meer dan 1 kW). Dit continu verbeteringsproces heeft geleid tot de ontwikkeling en optimalisatie van verschillende ontwerpen, elk met verschillende geometrische, magnetische of wikkelformen. Sommige machines zijn zodanig ontworpen dat ze een magnetische flux hebben die zich radiaal door de rotor voortplant, terwijl anderen een axiale flux faciliteren. Elk ontwerp heeft zijn eigen voor- en nadelen. Afhankelijk van de stroombehoefte, efficiëntie-eisen en het budget kan een ontwerpkeuze worden gemaakt. Ondertussen evolueren de toepassingen van elektrische machines voortdurend. Dit is - althans gedeeltelijk - te danken aan de vooruitgang op het gebied van vermogenselektronica door de technologie te ontwikkelen voor steeds hogere schakelfrequenties van transistors. Snellere en efficiëntere halfgeleider-technologie maakt het ontwerpen van kleinere machines met een hoger vermogen mogelijk. Door evoluties in gebruikerspatronen zoals de toenemende elektrificatie van persoonlijke mobiliteit en de transportindustrie neemt de vraag naar goedkope, lichtgewicht elektromotoren met een hoge vermogensdichtheid toe. Wanneer kleinere machines met een hogere snelheid moeten werken, nemen de energieverliezen die verband houden met de magnetisatie van de ferromagnetische kern exponentieel toe. Tegelijkertijd worden de parasitaire elektromagnetische effecten die verband houden met de constructie van de machine proportioneel groter.

Hierdoor bieden zich nieuwe uitdagingen aan bij het modelleren van de impact van het productieproces op het materiaalgedrag.

Het doel van dit proefschrift is om de constructieaspecten van ferromagnetische kernen en de impact die ze hebben op de prestaties van elektrische machines te onderzoeken. Voor de meeste industriële toepassingen wordt de ferromagnetische kern samengesteld uit afzonderlijke dunne lamellen met een gebruikelijke dikte tussen 0.2 mm en 1 mm. Een stapel van dergelijke lamellen is superieur aan een massieve ongelamelde kern omdat men op die manier tijdens het magnetisatieproces de vorming van ongewenste wervelstroomcircuits drastisch beperkt. Bovendien hebben dunne platen een veel hogere bewerkbaarheid dan massieve stapels. De geometrie van de lamel wordt gesneden uit grote gewalste stalen rollen. Vervolgens worden de lamellen gestapeld en samengevoegd om solide stapels te vormen.

In dit proefschrift wordt de invloed onderzocht van snij- en verbindingstechnieken op de materiaaleigenschappen van verschillende industriële staal-soorten, namelijk NO27, M100-23P, M270-35A en M400-50A. De impact van het productieproces op de statorkern wordt bestudeerd met behulp van magnetische metingen om het effect op de globale ijzerverliezen te bepalen. Op basis van deze metingen wordt getoond hoe materiaalmodellen geparametriseerd kunnen worden die de impact van specifieke productietechnieken nauwkeurig kunnen simuleren. Deze materiaalmodellen kunnen worden geïntegreerd in volledige machinemodellen. Door deze integratie kunnen machineontwerpers de prestaties van de machine berekenen waarbij tegelijk rekening gehouden wordt met het effect van het productieproces.

In hoofdstuk 1 worden het ontwerp en de fabricage van deze kernen besproken en wordt een overzicht gegeven van de meest gebruikte fabricagetechnieken. Het eerste hoofdstuk wordt afgesloten door uit te leggen hoe de productie van de kern de efficiëntie beïnvloedt door gebruik te maken van de energiebalans van de hele machine.

Hoofdstuk 2 richt zich op het gedrag van het materiaal in ferromagnetische kernen. Meer specifiek wordt een intuïtieve uitleg gegeven van het magnetisatieproces in zachte ferromagnetische materialen. Die uitleg is fundamenteel om de oorsprong van het kernverlies te begrijpen. Verderop in dit hoofdstuk wordt beschreven hoe de essentiële magnetische materiaaleigenschappen kunnen worden gemeten met gestandaardiseerde of experimentele meettechnieken.

In Hoofdstuk 3 verduidelijkt een reeks experimenten hoe constructietechnieken de magnetische eigenschappen van elektrisch staal kunnen beïnvloeden. Het biedt een aantal interessante kwantitatieve inzichten over de mate van degradatie die bepaalde fabricagetechnieken veroorzaken. Bij het vergelijken van verschillend gesneden geometrieën van korrelgeoriënteerd M100-23P-staal, waren de gemeten kernverliezen in het lasergesneden sam-

ple ongeveer 40 % hoger bij een piekfluxdichtheid van 1,5 T dan in het guillotine-uitgesneden monster. In een ander experiment wordt geïllustreerd hoe de beschadigde materiaaleigenschappen gedeeltelijk kunnen worden hersteld door uitgloeien. Twee technieken voor het verbinden van lamellen, namelijk interlocking en lassen, werden bestudeerd door de magnetische eigenschappen te vergelijken op prototypes van statorkernen voor en na het verbindingsproces. Deze experimenten toonden aan dat de ijzerverliezen stijgen met 11 % en 41 %, respectievelijk door het interlocken en het lassen van de lamellen.

Hoofdstuk 4 beoogt te demonstreren hoe magnetische metingen kunnen gecapteerd worden in materiaalmodellen om de impact van productietechnieken op het ontwerp van de ferromagnetische kern vast te leggen. Dit hoofdstuk begint met een gedetailleerde literatuurstudie in de state-of-the-art van dit specifieke onderzoeksdomein. Daarna worden drie methodieken uitgewerkt die ontwikkeld zijn om de impact van snij-effecten, interlocking en lassen te modelleren. Elk van de methodologieën wordt toegepast op realistische motorprototypes in de vorm van een case study.

In Hoofdstuk 5 wordt de focus gelegd op de onderliggende oorzaken van magnetische materiaaldegradatie. De resterende mechanische spanning die door fabricagetechnieken wordt geïntroduceerd, heeft invloed op het magnetisatieproces, wat resulteert in verminderde algehele magnetisatieprestaties. De relatie tussen mechanische spanning en magnetische eigenschappen wordt gemeten in verschillende experimenten voor uni-axiale spanning en spanning in de richting van de lameldikte. Metingen lieten een daling van 60 % in magnetische permeabiliteit zien bij een piekfluxdichtheid van 1,5 T wanneer het staal M270-35A tot treksterkte werd belast. Verder onderzoek naar de magnetische eigenschappen van staal onder plastische vervorming resulteerde in nieuwe inzichten in de magnetische eigenschappen nabij de snijrand van laminaten. De microstructuur van deze vervormde samples werd bestudeerd met behulp van elektronenmicroscopie om de gemeten macroscopische magnetische eigenschappen te verifiëren.

In het zesde hoofdstuk wordt een nieuwe benadering voor het modelleren van materiaaldegradatie door productietechnieken voorgesteld. Deze benadering omvat het vastleggen van de relatie tussen mechanische spanning en magnetische eigenschappen in een magnetomechanisch model en vervolgens het toepassen van dit model in een Magnetisch Equivalent Circuit (MEC). Het MEC-model gebruikt ruimtelijke discretisatie om de gedegradeerde gebieden weer te geven, elk met specifieke magnetische eigenschappen, afhankelijk van het lokale spanningsniveau. De effectiviteit van deze nieuwe aanpak wordt gevalideerd voor interlocked en gelaste statorkernen.

Om af te sluiten biedt het laatste hoofdstuk een terugblik op de belangrijkste conclusies en een aantal richtlijnen voor toekomstig onderzoek.

Summary

Increasingly stringent CO₂ emission targets are set by governing entities worldwide with the purpose of counteracting climate change and reducing the dependence on non-renewable energy sources. Meeting these targets requires efforts on many fronts, one of which being the increase in efficiency of the electrical energy grid. The infrastructure of the electricity grid consists of machines and equipment for generation, transportation, storage and consumption of electrical energy. The machines that facilitate this form of energy can be classified into either transformers, generators or motors, depending on their purpose. These three types of machines are generally referred to as 'electrical machines'. Ever since the first electric motor was patented by Thomas Davenport in 1837, engineers have continuously improved their design and managed to push the efficiency of these machines well above 85% (for machines with a rated power output greater than 1kW). This has led to the development and optimization of several designs, each having different geometric, magnetic or winding configurations. Some machines are designed to have a magnetic flux which propagates radially through the rotor while others facilitate an axial flux. Each design has its own advantages and disadvantages. Depending on the power requirements, efficiency requirements and budget, a design choice can be made. Meanwhile, the areas of application are constantly evolving. This is due - at least in part - to the advances in the field of power electronics by providing the technology for increasingly higher transistor switching frequencies. Faster and more efficient semiconductors enable the design of smaller machines with a higher power output. For example, the electrification of personal mobility and the transportation industry increase the demand for low cost, low weight electrical motors with a high power density. When smaller machines need to operate at a higher speed, the energy losses related to the magnetization of the ferromagnetic core increase exponentially. Simultaneously the parasitic electromagnetic effects that are linked to the manufacturing of the machine become proportionally more significant. This poses new challenges in the modelling of the material and manufacturing effects.

The goal of this thesis is to investigate the construction aspects of ferromagnetic cores and the impact they have on the performance of electrical ma-

chines. In most industrial applications, the ferromagnetic core is assembled from individual thin laminations of sheet material. A lamination assembly is superior to a solid stack because it drastically limits the formation of undesirable eddy current circuits. Additionally, thin sheets have a much higher machinability than solid stacks. The lamination geometry of stator and rotor is cut from the original steel coil. Then, the laminations are stacked and joined to form solid stacks. In the thesis, it is studied how cutting and joining techniques impact the material properties of several industrial steel grades, namely NO27, M100-23P, M270-35A and M400-50A. The impact of core manufacturing is studied using magnetic measurements on stator stacks to show their effect on the global core energy losses. Based on these measurements, it is shown how material models can be parametrized that succeed accurately in simulating the impact of specific production techniques. These material models can be integrated into full machine models. This integration enables machine designers to calculate the machine performance with the effect of core manufacturing taken into consideration.

In Chapter 1, the design and manufacturing of these cores is discussed and an overview is given of the most frequently used manufacturing techniques. The first chapter concludes by explaining how core manufacturing impacts efficiency using the energy balance of the whole machine.

Chapter 2 focuses on the behaviour of the material in ferromagnetic cores. More specifically, an intuitive explanation of the magnetization process in soft ferromagnetic materials is given, which is fundamental to understanding the origin of the core loss. Further in this chapter, it is described how the essential magnetic material properties can be measured using standardized or experimental measurement techniques.

In Chapter 3, a series of experiments clarifies how construction techniques can impact the magnetic properties of electrical steels. It provides some interesting quantitative insights on the degree of degradation that certain manufacturing techniques cause. When comparing differently cut geometries of grain-oriented M100-23P steel, the measured core losses in the laser cut sample were approximately 40 % higher at 1.5 T peak flux density than in the guillotine cut sample. In another experiment, it is illustrated how the damaged material properties can partly be restored by stress relief annealing. Two techniques for joining laminations, namely interlocking and welding, were studied by comparing the magnetic properties of prototype stacks before and after joining the laminations. In these experiments, it was found that the measured core losses increased up to 11 % and 41 % due to interlocking and welding, respectively.

Chapter 4 aims to demonstrate how magnetic measurements can be combined with material models to capture the impact of production techniques in the design of the ferromagnetic core. This chapter starts with a literary deep dive into the state-of-the-art of this specific research domain. Afterwards, three method-

ologies are elaborated that were developed to model the impact of separation, interlocking and welding. Each of the methodologies are applied to realistic motor prototypes in the form of a case study.

In Chapter 5, the focus is placed on the underlying causes of magnetic material degradation. The residual mechanical stress introduced by manufacturing techniques impacts the magnetization process, resulting in decreased overall magnetization performance. The relation between mechanical stress and magnetic properties is measured in several experiments for uni-axial stress and stress in the lamination thickness direction. Measurements revealed a 60 % drop in magnetic permeability at 1.5 T peak flux density when the M270-35A steel sample was stressed up to tensile strength. Further investigation of the magnetic properties of steel under plastic deformation resulted in new insights into the magnetic properties near cut edge of laminations. The microstructure of these deformed samples was studied using electron microscopy to verify the measured macroscopic magnetic properties.

In the sixth chapter, a new approach to manufacturing modelling is proposed. This approach involves capturing the relation between mechanical stress and magnetic properties into a magnetomechanical model and consequently applying this model in a Magnetic Equivalent Circuit (MEC) model. The MEC model uses spatial discretization to represent the damaged regions, each having specific magnetic properties depending on the local stress level. The effectiveness of this new approach is validated for interlocked and welded stator cores.

To conclude the thesis, the last chapter offers a review of the main conclusions and a number of guidelines for future research.

List of Abbreviations

2D	Two Dimensional
3D	Three Dimensional
CF	Cost Function
CNC	Computer Numerical Control
CSR	Current Sensing Resistor
DAQ	Data Acquisition
DC	Direct Current
DD	Diagonal Direction
EBSD	Electron Backscatter Diffraction
EDM	Electric Discharge Machining
EMF	Electromotive Force
FEM	Finite Element Modelling
GO	Grain Oriented
ILEC	Interlaminar Eddy Currents
ISO	International Organization for Standardization
MEC	Magnetic Equivalent Circuit
MMF	Magnetomotive Force
MOKE	Magneto Optical Kerr Effect
NO	Non Oriented
RD	Rolling Direction
SEM	Scanning Electron Microscopy
SLT	Statistical Loss Theory
SRM	Switched Reluctance Motor
SST	Single Sheet Tester
TD	Transverse Direction
TEM	Transmission Electron Microscopy
TIG	Tungsten Inert Gas
XRD	X-Ray Diffraction
YASA	Yokeless And Segmented Armature

List of Symbols

Scalars, vectors and matrices

A	Magnetic Core Cross Section	m^2
α_e	current angle	$^\circ$
B	Magnetic Flux Density	T
B_p	Peak magnetic flux density	T
C_{hyst}	Hysteresis Loss coefficient	$W.s.kg^{-1}.T^{-1}$
C_{cl}	Classical Loss coefficient	$W.s^2.kg^{-1}.T^{-2}$
C_{exc}	Excess Loss coefficient	$W.s^{1.5}.kg^{-1}.T^{-1.5}$
D	Electric Flux Density	C/m^2
d	Lamination Thickness	m
δ	Degrading impact of interlocking	-
E	Electric Field Strength	V/m
E_{tot}	Total Energy	J
E_{ext}	Energy from externally applied field	J
E_{an}	Magnetic Anisotropy Energy	J
E_{dom}	Energy from interaction between magnetic domains	J
E_{MS}	Magnetostatic Energy	J
E_{ME}	Magnetoelastic Energy	J
ϵ_0	Vacuum Electrical Permittivity	$8.854 \text{ e-}12 \text{ F/m}$
ϵ_r	Relative Electrical Permittivity	-
f	Frequency	Hz
\mathcal{F}	Magnetomotive Force	A
γ	Electric Charge Density	C/m^3
H	Magnetic Field Strength	A/m
H_{ext}	External homogeneous magnetic field	A/m
H_{coer}	Coercive Field Strength	A/m
h_d	Height of degraded zone	m
i	Electric Current	A
J	Electric Current Density	A/m^2
K_μ	Correction factor for relative magnetic permeability	-
K_{hyst}	Correction factor for hysteresis loss component	-
K_{exc}	Correction factor for excess loss component	-
κ	Electrical Conductivity	S/m
l	Average magnetic path length	m
l_d	Length of degraded zone	m

l_{ud}	Length of undamaged zone	m
m	Magnetic moment	A.m ²
μ_{deg}	Relative magnetic permeability in degraded zone	-
μ_r	Relative Magnetic Permeability	-
μ_0	Vacuum Magnetic Permeability	4 π e-7 H/m
N_1	Amount of primary turns	-
N_2	Amount of secondary turns	-
P_{tot}	Total Core Loss	W/kg
P_{hyst}	Hysteresis Loss	W/kg
P_{cl}	Classical Loss	W/kg
P_{exc}	Excess Loss	W/kg
R	Magnetic Reluctance	H ⁻¹
R_{deg}	Radius of degraded zone	m
R_{weld}	Radius of welded zone	m
W_{tot}	Total core loss per cycle	J/m ³
W_{hyst}	Hysteresis loss per cycle	J/m ³
W_{cl}	Classical loss per cycle	J/m ³
W_{exc}	Excess loss per cycle	J/m ³
w_d	Width of degraded zone	m
w_{tot}	Total width	m
ρ	Mass Density	kg/m ³
ρ_{res}	Electrical Resistivity	Ω .m
σ	Mechanical Stress	MPa
σ_{ax}	Mechanical stress in axial direction	MPa
σ_{eq}	Equivalent stress	MPa
$\sigma_{eq,2}$	Equivalent stress in degraded zone	MPa
$\sigma_{eq,3}$	Equivalent stress in welded zone	MPa

List of Publications

Articles in international SCI journals

1. A. Daem, P. Sergeant, L. Dupré and M. Ibrahim "Modeling Interlocking Effects on Core Losses in Electrical Steel", *IEEE Transactions on Electrical and Electronic Engineering*, 15.12 (2020), pp.1836-1843
2. R. Sundaria, A. Daem, O. Osemwinyen, A. Lehtikoinen, P. Sergeant, A. Arkkio and A. Belahcen "Effects of Stator Core Welding on an Induction Machine - Measurements and Modelling", *Journal of Magnetism and Magnetic Materials*, 499 (2020): 166280
3. A. Daem, P. Sergeant, L. Dupré, S. Chaudhuri, V. Bliznuk, L. Kestens, "Magnetic Properties of Silicon Steel After Plastic Deformation", *Materials*, 13.19 (2020): 4361
4. A. Daem, P. Sergeant, L. Dupré, M. Ibrahim "Stress Dependent Magnetic Equivalent Circuit for Modelling Welding Effects in Electrical Steel Laminations", *Electric Power Components and Systems*, Under review.

Conference Proceedings

1. A. Daem, P. Sergeant, and L. Dupré, "Measuring Magnetic Properties in Stack Structures of Non Grain Oriented Electrical Steel Laminations", *Young Researchers Symposium - IEEE Benelux Chapter IAS/PES/PESC*, Brussels, Belgium, May 24 - 25, 2018.
2. R. Sundaria, A. Daem, A. Hemeida, P. Sergeant, A. Arkkio and A. Belahcen, "Effect of Different Cutting Techniques on Magnetic Properties of Grain Oriented Steel Sheets and Axial Flux Machines", *IECON 2019-45th Annual Conference of the IEEE Industrial Electronics Society*, Lisbon, Portugal, October, 2019

3. M. N. Ibrahim, J. Nonneman, A. H. Mohamed, A. Daem, A. Abdallh, S. Schlimpert, M. De Paepe, P. Sergeant "Directly Cooled Windings in Switched Reluctance Machines", *2020 International Conference on Electrical Machines (ICEM)*, Gothenburg, August, 2020

**MANUFACTURING EFFECTS ON ELECTROMAGNETIC
PROPERTIES OF FERROMAGNETIC CORES IN ELECTRICAL
MACHINES**

1

Introduction

Electrical machines can be geometrically designed in a variety of different ways, but their fundamental working principles are identical. A combination of controlled electric currents and magnetic fields magnetizes the ferromagnetic core to obtain the desired energy conversion. Because machine core manufacturing is the main focus of this thesis, a relevant starting point would be to describe the underlying physical phenomena in electrical machines.

1.1. Design of Electrical Machines

Generators, motors and transformers rely on the theory of classical electromagnetism which can be described by Maxwell's laws and the Lorentz force Law. These laws form a collection of relations between the physical quantities that occur during the normal operation of electrical machines. In their macroscopic differential form, Maxwell's equations are:

- Gauss's Law for Magnetic Fields

$$\nabla \cdot \mathbf{B} = 0 \quad (1.1)$$

- Gauss's Law for Electric Fields

$$\nabla \cdot \mathbf{E} = \frac{\gamma}{\epsilon_0} \quad (1.2)$$

- Ampère's Law

$$\nabla \times \mathbf{B} = \mu_0 \left(\mathbf{J} + \epsilon_0 \frac{\partial \mathbf{E}}{\partial t} \right) \quad (1.3)$$

- Faraday's Induction Law

$$\nabla \times \mathbf{E} = -\frac{\partial \mathbf{B}}{\partial t}. \quad (1.4)$$

Gauss's Laws describe the behaviour of electric and magnetic fields. (1.1) states that any outflow through an enclosing surface of a magnetic charge is zero, indicating that there is no such thing as a single magnetic charge but only a magnetic dipole. On the other hand, (1.2) specifies that the outflow of an electric field through any enclosing surface is proportional to the electric charge within this surface. Faraday's Law and Ampère's Law show how electric fields and magnetic fields influence each other. More specifically, they describe how a time varying electric current in one winding can induce a voltage in another. The electric charges in a current-carrying conductor experience a Lorentz force in the presence of an electric and magnetic field. This force generates the torque necessary for motor operation.

When the Maxwell equations are solved in realistic applications such as electrical machines, the materials in which they manifest codetermine the solution. This gives rise to the following three constitutive relations in which the specific material properties appear:

- The relative electric permittivity ϵ_r

$$\mathbf{D} = \epsilon_0 \epsilon_r \mathbf{E} \quad (1.5)$$

- The relative magnetic permeability μ_r

$$\mathbf{B} = \mu_0 \mu_r \mathbf{H} \quad (1.6)$$

- The electrical conductivity κ in [S/m]

$$\mathbf{J} = \kappa \mathbf{E} \quad (1.7)$$

These material parameters determine the densities of the electric field, the electric current and magnetic flux. In order to improve the efficiency of electric machines, ferromagnetic silicon steels are used to construct the machine core. Because of their frequent application in electrical machines, silicon steels are often referred to as electrical steels. This material can also be classified as

a soft magnetic material because it is easily magnetized and demagnetized. The relative permeability of silicon steels is several thousands of times higher than vacuum, facilitating a high magnetic flux density which makes them especially suitable for use in the core of electrical machines.

However, the high magnetic permeability of silicon steel is not a constant but rather a hysteretic, non-linear and anisotropic function of the magnetic field strength. This complex magnetic relation poses challenges in the modelling of electrical machines. A more detailed description of the causes and implications of this complex magnetic behaviour continues in Chapter 2. Additionally, the magnetic properties of an electrical steel core are influenced by the manufacturing techniques used during construction. In order to manufacture a core, several processes are involved which can create residual stress, thermal stress or plastic deformations within the material. These local changes to the microstructure of the steel increase the complexity of the modelling challenge. Especially considering the fact that this material forms the core of most generators, transformers and motors within the electrical grid system, it is important to have an accurate and reliable material model which can be used in machine models.

1.2. Manufacturing of Electrical Machine Cores

The assembly of the parts in an electrical machine has a significant influence on the final quality of the machine [58]. The machines are manufactured in distinct consecutive steps. First, the individual laminations are shaped from a coil of electrical steel. Depending on the application and the scale of production, the shaping can be done using punching, water jetting, laser cutting or electric discharge machining. After shaping, the laminations are stacked together to form the stator and rotor of the machine. The stack is then compressed until the final stack length and stacking factor is achieved. With the stack compressed, the laminations are assembled by glue bonding, welding or interlocking in order to fixate the individual laminations to form a solid stack that provides the structural torsion strength necessary for motor operation. Afterwards, the windings are inserted and the motor housing is put in place. Fig. 1.1 shows an example of a stator and rotor stack with windings before housing.

1.2.1 Electrical Steel

Electrical steels form the core material in electrical machines. The properties of this steel must meet strict requirements with respect to magnetic, mechanical and economical characteristics. Given that they will be magnetized many times per second, the core losses associated with their magnetization should



Figure 1.1: Stator and rotor stack of an electric motor with stator windings.

remain low. Due to the high electrical conductivity of electrical steel (approximately $2.17 \times 10^{-6} \text{ S/m}$), a varying magnetic flux propagating through the material will induce eddy currents. According to Lenz's Law, these eddy currents will counteract any variation in magnetic flux. With the purpose of minimizing the eddy current losses, these cores are usually laminated. This implies that many laminations need to be manufactured and consequently stacked in order to build a solid core. Fig. 1.2 illustrates the effect of core laminating on the induction of eddy currents. Each lamination is coated so that they remain electrically isolated. The quality of this coating can be tested via the Franklin test whose operating principle consists of pressing electrodes onto the coated lamination surface and calculating an equivalent coating resistance based on the measured currents flowing between these electrodes. In [44], this standardized Franklin test method is validated and it is found that it does not register important local inhomogeneities which might occur in the coated surface. Nevertheless, it is concluded that the Franklin test provides an efficient tool for comparing different coatings. The different types of coatings and their advantages are discussed in detail in [40].

The silicon component is added to the electrical steel alloy to further reduce the undesirable eddy currents. The silicon atoms act as impurities in the crystal lattice. This altered grain structure has a higher resistivity and smaller hysteresis loss, thus having lower core losses. Commercially available electrical steels typically have a silicon content between 2 % and 6 % weight percentage. A further increase in silicon content decreases the magnetic permeability and increases the brittleness, which is detrimental to the workability of the material. Each type of electrical steel is either a grain-oriented (GO) electrical steel or a non-oriented (NO) electrical steel. GO electrical steels are manufactured so that they have superior magnetic properties in the rolling direction. This type of steel was first patented by Norman Goss in 1933 and was de-

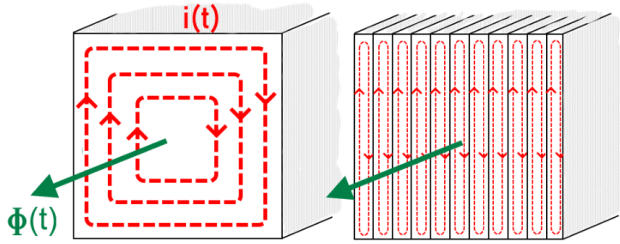


Figure 1.2: Visualisation of induced eddy currents when the flux is increasing. Laminating the core increases the electrical resistance of the eddy current circuit, resulting in lower eddy current losses.

signed to revolutionize the transformer industry due to its significantly lower energy losses when magnetized in the GO direction. Nowadays, GO steels are widely used in power transformers and, more recently, have found an application in high efficiency electric motors for the e-mobility industry (e.g. in axial flux machines). In [72], an interesting comparison is given between the application of GO and NO steel in axial flux machines. NO electrical steels are more magnetically isotropic, with almost the same magnetic properties in each direction. They are used in applications where a rotational magnetic flux occurs such as induction motors or switched reluctance motors. As demonstrated in [48] and [29] however, anisotropy is introduced in NO steels during the final cold rolling operations. Silicon steel can also be classified according to the degree to which the steel is processed. Semi processed steels are cold rolled, but are not yet annealed. This implies that the optimal magnetic properties are not yet present, and the annealing process is left to the core manufacturer. Fully processed steels are sold after annealing, have optimal magnetic properties and can be directly used by machine core manufacturers. Usually, GO steels are always fully processed steels. Electrical steels are classified by their grade. Despite the existence of an ISO norm for steel classification (ISO/TS 4949:2003), each industrial region prefers its own standard (e.g. EN10027 in the EU, AISI/SAE in the USA, JIS in Japan). In Fig. 1.3, a flowchart of a commercial electrical steel manufacturing process is shown. After the material is rolled on a coil by the steel manufacturer, the material is further processed by the machine core manufacturer. It is important to note that the variation in quality between the coils of steel significantly impacts the consistency of the efficiency of the machine. In [17], experimental core loss measurements showed that the variation in efficiency between finished generator stacks is largely related to the variation in quality of the raw coil material. This variation was larger than the variation due to the manufacturing process. In the

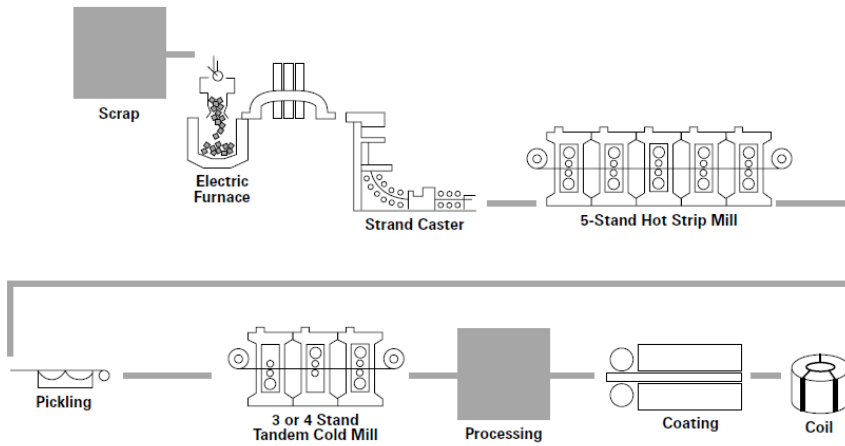


Figure 1.3: Flowchart of the production process of commercially available electrical steel at AK Steel [3]. The finished product is a coil of thinly coated steel.

following section, it is explained how the laminations are shaped and afterwards assembled. The most commonly applied techniques are described.

1.2.2 Shaping

The first stage in magnetic core manufacturing is the process of shaping. The sheets of electrical steel are processed according to the geometric design requirements of the electrical machine (Fig. 1.4). An overview of the most common shaping techniques is discussed in this section.

Punching

The lamination geometry is forced out of a larger steel sheet by means of hydraulic pressure on a punching tool (Fig. 1.5). The accuracy of this technique with respect to the achieved tolerances on the geometry dimensions is high, which is an important advantage for building electric motors with small air gaps. A high initial cost is related to this process since the punching tool geometry should be manufactured according to the lamination design. Nevertheless, punching is commonly used because of its simplicity, speed and cost-effectiveness for large batches. Two distinct types of punching can be discerned. In the first, the complete lamination geometry is shaped in one punch. Alternatively, the lamination geometry can be shaped by nibbling or nibble punching. In this case, a nibble tool is manufactured according to the specific lamination contour or tooth shape. The nibble tool is subsequently



Figure 1.4: Picture the stator lamination of an electric motor after punching (left) and sets of strips having different widths cut from the original steel sheet (right).

forced through the sheet after workpiece each rotation until the final geometry is completed (Fig. 1.6). Nibble punching is significantly slower than regular punching but requires a lower initial cost. The quality and tolerances of the workpiece are affected by the clearance and the wear of the punch/die. A worn out punching tool might result in unacceptable tolerances and large edge burrs. The recommended maximum clearance for steel punching is between 15 % and 20 % of the thickness of the sheet. In Fig. 1.7, the edge burr after nibble punching is shown. This photograph demonstrates how the punch/die clearance impacts the shape of the edge. The steel near the cutting edge is subject to mechanical stress which ultimately fractures the sheet, leaving the cut edge material in a plastically deformed state. In [14] an attempt at measuring the degradation depth near the cut edge was done by measuring the local residual stress using nano-indentation. This experiment reported a degradation depth of 0.5 mm in a 50W470 grade ring core that was punched using a clearance equal to 8 % of the material thickness. A similar experiment was reported in [35], where the microhardness was measured near cutting edges of punched laminations with a thickness of 0.35 mm. It was reported that the local hardness increased significantly towards the edge of the sample, levelling off at a distance of approximately 0.3 mm.

Laser Cutting

Laminations can be shaped by focusing a laser beam on the surface of the steel sheet. The heat generated on the surface of the sheet burns the coating and melts the steel. The molten steel then evaporates or is removed by a gas

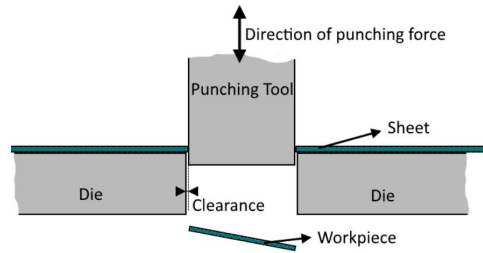


Figure 1.5: Side view of the punching process on sheets with indication of punching clearance between the punch and die.

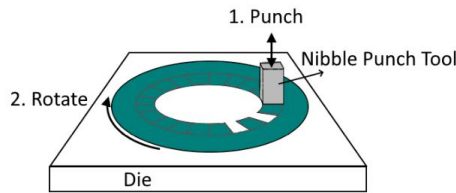


Figure 1.6: Illustration of the nibble punching process on laminations for rotating electrical machines. The nibble punch tool shapes the teeth individually. The workpiece subsequently rotates between the punches.

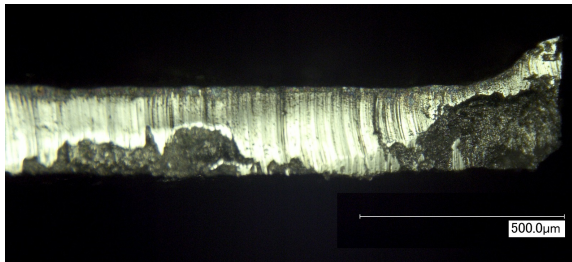


Figure 1.7: Sectional micrograph of the edge burr of a nibble punched lamination of NO27 electrical steel. Micrograph was taken using a Keyence digital microscope with 250 times magnification.

jet. The laser beam generates a large amount of heat in the steel sheet. This heat dissipates locally through the sheet, creating residual thermal stresses in the material. Instead of punching, which is a process that shapes an entire contour edge simultaneously, the laser beam cuts the material point by point (Fig. 1.8). Consequently, laser cutting is a slower process than punching and is more frequently used when prototypes or small batches of machine cores are built. When machining metals, a CO₂ type laser is frequently used. The laser

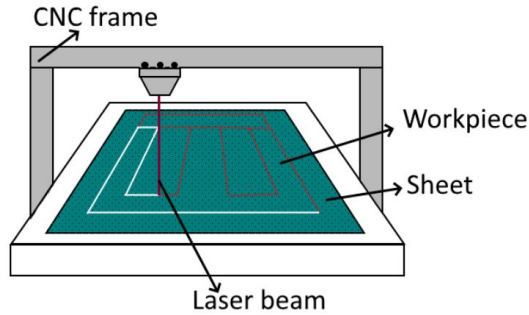


Figure 1.8: Left: Illustration of a laser cutting a lamination for an EI type transformer lamination. The laser is mounted on a CNC frame.

cut workpiece can be machined with a tolerance of $\pm 5 \mu\text{m}$, depending on the sheet thickness.

Water Jet Cutting

Similar to laser cutting, a water jet can be used for separating the workpiece from the sheet. In this process, a stream of water is forced through a thin nozzle at a pressure between 3000 and 6000 bar. The water contacts the steel sheet and through the process of erosion, the material is removed. When cutting through steel, this process can be accelerated by adding hard particles to the water (i.e. abrasive water jet cutting). The water jet nozzle is mounted on a CNC frame similar to laser cutting in Fig. 1.8. The achievable tolerance is similar to the laser cutting technique and also depends on the sheet thickness and the wear of the focus. Water jetting is a cold operation, which means that the material degradation due to heat generation is avoided. Due to the abrasive material removal process, the edge burr is also significantly less prominent than in the case of punching.

Electric Discharge Machining

In this technique, also known as EDM or spark erosion, material is removed by discharging electrical sparks from an electrode to the workpiece. The electric arc evaporates steel and breaks down the microstructure, separating the lamination from the sheet. The sparks are generated while the sheet is submerged in a dielectric liquid. This liquid also carries the debris away from the sheet.

Instead of a toolhead electrode, a wire can also be utilized for generating the sparks. This technique is called 'wire EDM' (Fig. 1.10). The electric arcs are

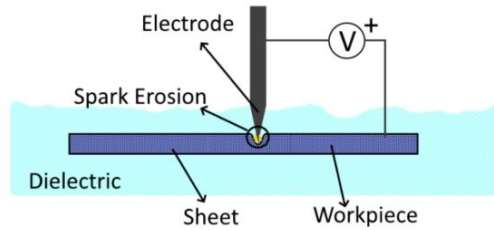


Figure 1.9: Sectional view of the electric discharge machining process.

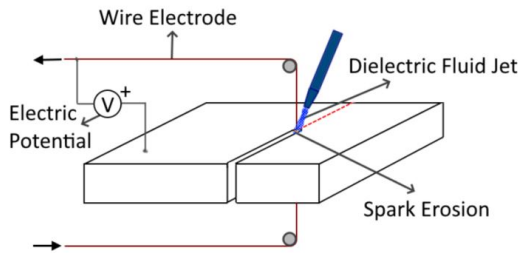


Figure 1.10: Illustration of the Wire EDM cutting process.

generated between the wire and the workpiece, while a constant distance between the wire and the workpiece is maintained by mounting the wire feed on a CNC system. The wire electrode, usually a brass alloy, also erodes and is therefore continuously fed through the workpiece on a spool. Depending on the feed rate and spark wire thickness, tolerances of $\pm 1 \mu\text{m}$ can be achieved. EDM is the preferred technique when low residual stresses are required, because there are no significant mechanical cutting forces acting on the workpiece. The dielectric also removes the heat generated in the spark. This results in significantly lower residual heating stress when compared to laser cutting. However, this is only valid when the electrical spark current is low or the duty cycle is small. This is only possible for low feed rates and consequently longer production times, which makes it unsuitable for mass production. An interesting overview of the EDM process parameters is discussed in [24].

1.2.3 Joining

After the shaping process, the individual laminations are assembled and joined into a rigid stack. Several joining techniques are available to the machine manufacturer. A technique should be chosen based on the design, ap-

plication, efficiency and the cost requirements of the electric machine. In this section, an overview is given of the most common techniques for joining electrical steel laminations.

Welding

Welding is the process of joining metals by melting and subsequently solidifying them using a heat source. This technique is commonly used in the production of magnetic cores, when the assembled stack of laminations is joined to form a rigid core. A highly concentrated heat source locally increases the temperature on the edge of the stack in a very short period of time. Simply put, the adjacent laminations melt and form a common puddle of liquid metal. Afterwards the metal solidifies to form a joined crystal lattice. Simultaneously the electrically insulating coating between the laminations is destroyed and a short circuit is created. This partially counteracts the beneficial effect of laminating the core.

There are many different welding techniques available. Factors such as the magnetic core size, required welding speed and weld joint strength determine the quality of the weld. The most common types of welds are TIG welding and laser welding. Tungsten Inert Gas (TIG) welding has been widely used in industry to join the laminated electrical steels because of the low cost and high flexibility [45]. TIG welding is a type of electric arc welding where one electrode is a tungsten rod. The other electrode is the ferromagnetic core. A shield of inert gas prevents oxidation during the welding process. Recently, laser welding is being applied as an alternative to TIG welding because of its higher welding speed and its convenience in automated production. The laser head moves along the axial length over the edge of the stack and creates a focal point where the heat is generated. Laser welding has proven to create a weld seam which is more narrow than most TIG welding seams. However, the desired welding joint strength should not be compromised. Both types of welding create residual stress and short circuits between the laminations. A consideration can be made based on the required weld joint strength and the acceptable amount of additional core losses. In [83], experimental results show that TIG welding creates a stronger weld joint strength but also creates higher additional core losses. Fig. 1.11 shows a laser welded stator stack.

The rapid local heating and subsequent cooling creates significant thermal stresses both in the weld seam and the surrounding area. This was verified experimentally in [61] and [76] using techniques such as X-Ray Diffraction and Barkhausen Noise Detection by measuring residual stress. This indicates that welding as a joining technique affects the microstructure of the steel and potentially impacts the movement of magnetic domain walls during magnetization. The welding seam forms an electrical short circuit which facilitates eddy currents. This short circuit is illustrated in the section view of Fig. 1.12.

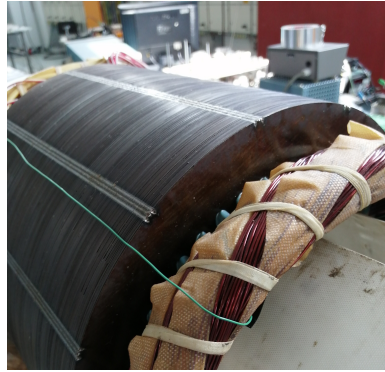


Figure 1.11: Photograph of an induction motor without rotor and housing. The stator stack was joined using laser welding.

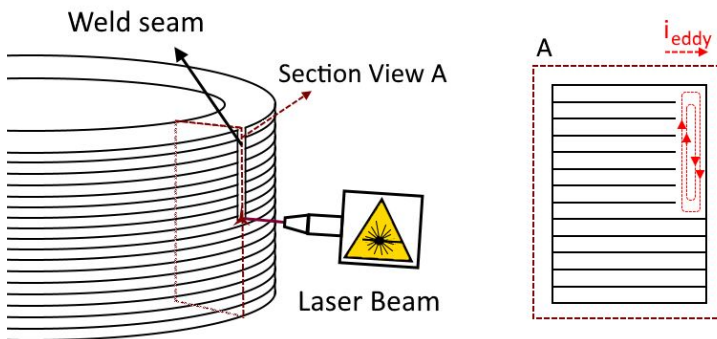


Figure 1.12: Illustration laminations formed into a rigid stack during laser welding. A section view shows the eddy current path in the weld seam when the stack is magnetized.

Interlocking

Another technique for joining laminations is often referred to as 'interlocking'. This is a variation on the tongue and groove method. In the individual laminations, local indentations are made which protrude on one side. Then, the indented laminations are pressed together to form a solid stack by means of a form fitting. Fig 1.13 shows a rotor and stator stack which have been joined using interlocking. The production of the indentations is often combined with the punching process described earlier in section 1.2.2. The shape of the lamination is punched out of the steel sheet, and the indentations are made simultaneously. This process evidently creates plastic deformations and local residual stress which is known to negatively impact the magnetic properties of the material. Similar to the welding technique, the electrical isolation

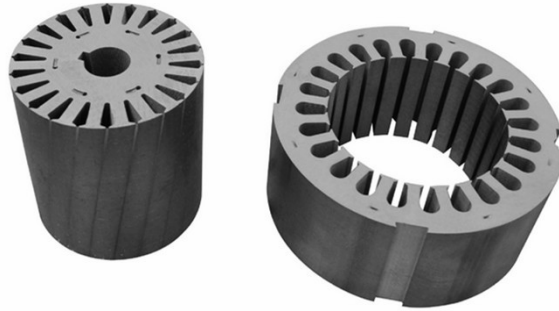


Figure 1.13: Interlocked stator and rotor laminations pressed into a rigid stack.

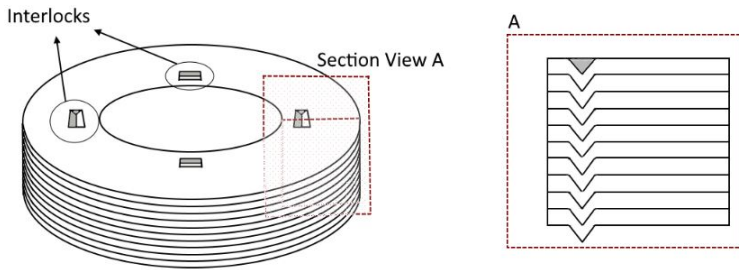


Figure 1.14: Illustration and cross section view of an interlocked stack of laminations.

between the laminations might be compromised by interlocking. The indentation and subsequent pressing of the laminations might break the isolating coating, enabling interlaminar local eddy currents to flow. Interlocking is frequently applied in mass production. The indentation of the interlocking dowel can be done together with the punching process. Afterwards, only a pressing of the laminations is needed, which makes the combination of punching and interlocking time and cost effective.

Clamping

The loose stack of laminations can be joined using an external mechanical force. This can be achieved by means of a bolt and nut joint, such as displayed in Fig. 1.15. These kinds of joining techniques are usually not preferred due to the increased stack length, outer diameter or negative impact on the yoke geometry. Additionally, they require sophisticated automated or manual assembly.

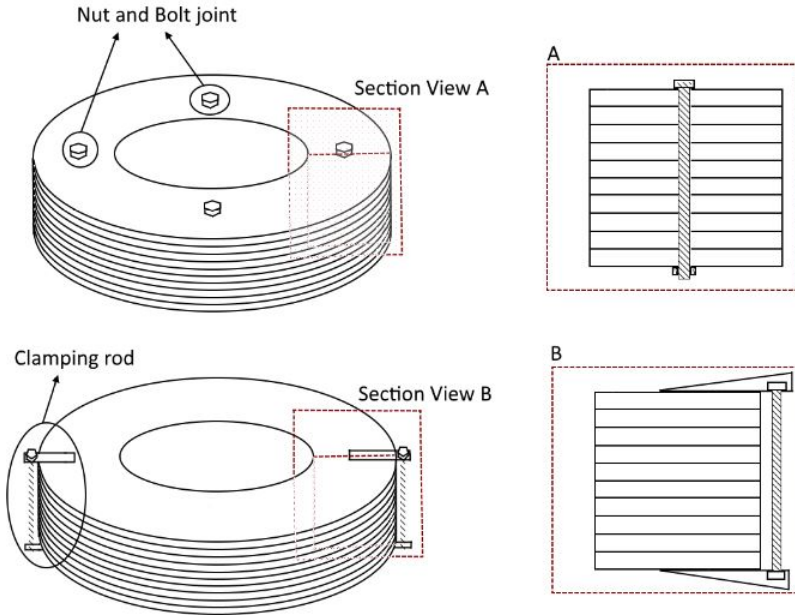


Figure 1.15: Illustration of a clamped stack of laminations using a nut and bolt mechanism.

Bonding

Laminations can also be joined using a bonding agent such as varnish or glue. These agents are typically added on individual laminations and, after stacking, on the stack surface as a type of coating (Fig. 1.16). Some isolating coatings for fully processed steels have adhesive properties which eliminate the need for a separate coating process before stacking. However, it has been reported that laser cutting might evaporate the coating, leaving some parts of the lamination exposed and potentially creating interlaminar short circuits near the cutting edge [35]. After the coating is applied the bonding is thermally activated, i.e. it needs to be cured in an oven for the coating to gain its adhesive strength. During this curing, the adhesive expands and hardens. This joining technique is known to produce only a small amount of additional stress to the laminations due to the compressive force exerted on the stack during the application of the coating. This pressure is needed to ensure flat contact between the laminations. In [63], the effects were compared between adhesive bonding and welding on the magnetic properties of ring core samples of silicon steel with a thickness of 0.5 mm. It was found that glue bonding increases the core losses by approximately 6 % and 2 % at 1 T and 1.5 T, respectively. Welding is comparatively more detrimental to the magnetic properties than

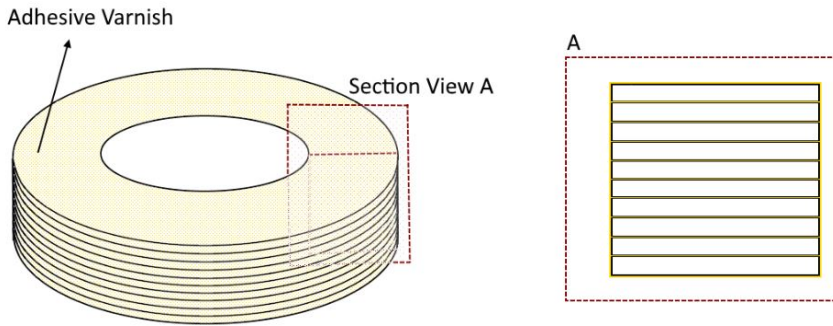


Figure 1.16: Illustration of stack of laminations assembled with adhesive varnish.

glue bonding even if only two welding seams were applied. Alternatively, in [73], the favourable magnetic degradation as result of glueing over interlocking or welding was shown. In this paper, the core losses are 25 % higher in the interlocked stack than in the glued stack - at 1.5 T and 400 Hz excitation.

1.2.4 Stress Relief Annealing

The annealing process is well known among metallurgists and refers to the process of heating a material to above its recrystallization temperature and subsequently slowly cooling it down. During this recrystallization, the microstructure of the material is reassembled. Depending on the heating and cooling rates, this heat treatment decreases the amount of dislocations and residual stress. For electrical steel stacks, annealing is often done after shaping and stacking the laminations in order to relieve the stress that has invaded the steel during manufacturing. This process is therefore used for the purpose of (at least partly) restoring the magnetic properties of the steel. The stack is placed in a furnace with controlled temperature. However, the contact between the surface of the steel and the atmosphere can enable oxidation or nitration. This can be avoided by controlling the atmosphere during annealing using an endothermic gas. In [51], experimental results are shared of the impact of temperature and atmosphere composition on the beneficial effects of stress relief annealing in NO electrical steel with 2 wt% silicon. Reportedly the core losses decreased as much as 0.2 W/kg when the temperature ranged between 750 °C and 800 °C. It should be noted that the atmospheric conditions in the furnace play a mayor role in the degree of nitration or oxidation, potentially completely counteracting the restoring capabilities of this process. From production perspective, annealing is costly (both in time and energy) because it has to be done under a controlled atmosphere at higher furnace

temperatures for a long period of time (up to 24 hours). When annealing the laminations, a proper coating should be applied to the laminations. This coating should be able to resist high annealing temperatures and maintain the electrical isolation between the laminations. Machine manufacturers should compare the added cost of this process and relatively long processing time to the added benefit of the restored magnetic properties and consider it as an engineering choice or investment decision.

1.3. Efficiency of electrical machines

The total power input of an electrical machine is transformed into either an electrical power output (in the case of a transformer or generator) or a mechanical power output (in the case of a motor). As with any machine there are energy losses associated with this conversion. Those losses can be divided into several categories, depending on their physical origin (Fig. 1.17). Copper losses are the resistive losses in the conductors, also called Joule losses. The mechanical losses are a result of air friction and bearing friction of the rotating part of an electrical machine. The iron loss originates from the energy that is lost during the magnetization cycle of the electrical steel in the machine core. Traditionally, these losses are estimated based on data provided by the electrical steel supplier. However, the iron losses are significantly impacted by the manufacturing process of the machine. Because of this, another loss category can be added which includes all the additional losses related to the manufacturing of the machine core. In this thesis, an investigation of the influence of several manufacturing processes on the energy losses in ferromagnetic cores is done with the purpose of gaining a more detailed understanding of the effects of manufacturing on the quality of electrical machines.

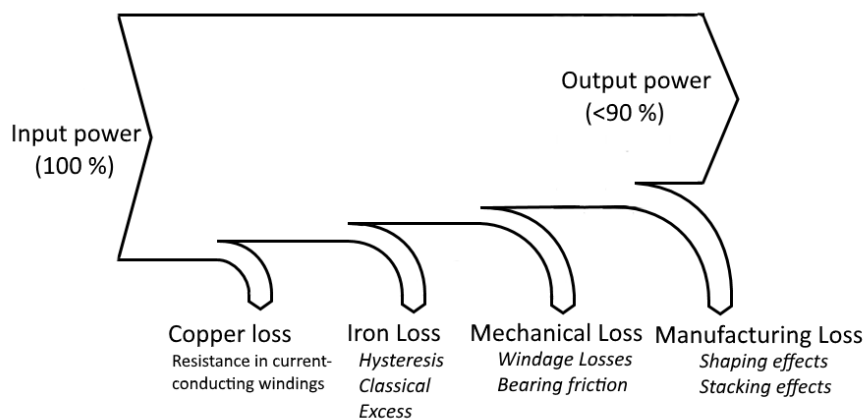


Figure 1.17: Overview of the power losses in rotating electrical machines.

2

Modelling of Magnetic Materials

Silicon steels play a crucial role in electrical engineering applications. The thickness, relative permeability and energy losses are the main technical parameters used to benchmark different grades of soft magnetic materials. Their complex physical properties and the wide range of excitation regimes in their application create a difficult challenge to build a material model. In the past few decades, several approaches have been proposed to solve this problem. This was possible through detailed investigation of the physical nature of the magnetization process which is, by its nature, stochastic. Although the complete description of magnetization in ferromagnetic materials is a monumental work in progress, it is the task of engineers to work around the incomplete physical models and provide workable and accurate solutions to build applications. This is why, in the field of engineering, empirical models are often preferred for their relatively low computational workload. Based on measurements and observation, phenomenological models can be developed which identify the key variables and relate them accurately to the energy losses. Nevertheless, having an accurate understanding of the magnetic behaviour of this material is necessary for applying these models. In this chapter, the microstructural phenomena and energy losses related to the magnetization process in ferromagnetic materials are discussed. Afterwards, a detailed de-

scription is given of how this behaviour can be modelled empirically using magnetic measurement techniques and an inverse problem methodology. In order to gain an understanding of soft ferromagnetic behaviour, the paradigm of Domain Theory provides a good point of entry.

2.1. Domain Theory

The microstructure of electrical steel is polycrystalline, which implies that it consists of several grains. The average grain size depends on the heat profile during the crystallisation process. Within the grains, the microscopic crystal structures consist of domains each having a uniform magnetic moment equal to the saturation magnetization. The fundamental origin of this moment is described in the field of quantum mechanics. When the alloy cools down below the Curie temperature (which is approximately 760°C for silicon steel), the material transitions from the paramagnetic to the ferromagnetic state which corresponds to the formation of a domain structure. This phenomenon gives the steel its ferromagnetic properties and allows it to be classified among the soft magnetic materials. For NO steels, the distribution of the magnetization direction domains is random. On the contrary, GO electrical steel is manufactured in such a way that improved magnetic properties exist parallel to the rolling direction of the sheet. In this case, the magnetic orientation of the domains is not random. Domain Theory, which was first proposed by Pierre Weiss in 1907 [79], considers the microscopic areas with uniform magnetic moment as domains which are separated by domain walls. The average magnetization of the material is determined by the vectorial sum of magnetization of all the individual domains. The domain structure present in the material is a result of the equilibrium between different energetic sources inherent to the domains. The total energy in the system (often referred to as the Gibbs free energy) is the sum of its sources:

$$E_{tot} = E_{ext} + E_{an} + E_{dom} + E_{MS} + E_{ME} \quad (2.1)$$

where E_{ext} is the energy from the externally applied field, E_{an} is the energy related to magnetic anisotropy, E_{dom} is the energy originating from interaction between neighbouring domains, E_{MS} is the magneto-static energy and E_{ME} is the magneto-elastic energy.

2.1.1 Energy from externally applied field

An externally applied magnetic field will act upon the magnetic domains as they tend to align their magnetic moment with this external field. The energy added to this system during this interaction can be calculated as

$$E_{ext} = - \sum_{i=1}^n \mathbf{m}_i \cdot \mathbf{H}_{ext} \quad (2.2)$$

where \mathbf{H}_{ext} is the external homogenous magnetic field, and \mathbf{m} is the magnetic moment of each domain.

2.1.2 Anisotropic Energy

This energy term is minimized when the domains are oriented parallel to the 'easy' magnetization direction. In a single crystal of body centered cubic iron, this easy magnetization direction is parallel to the cube edge of the crystal. The anisotropic energy is minimized when the magnetic moment of the domain is aligned with the one of the easy magnetization direction. When an external magnetic field is applied parallel to any other direction (e.g. parallel to the diagonals of the cube), a higher magnetic field strength will be needed to saturate the material. Any deviation from this 'easy'-alignment will correspond to an increased energy of the system.

2.1.3 Domain Wall Energy

The domain wall energy originates from the energy exchange within the domain wall between adjacent domains. This energetic term is minimized when the orientation of magnetic dipoles of two adjacent domains is parallel, which means that the magnetic orientation changes 180° within the domain wall from edge to edge. Depending on the thickness of the sample, two types of 180° domain wall reorientations can occur, namely the Bloch wall and the Néel wall.

2.1.4 Magnetostatic Energy

This energy is equal to the magnetic field necessary for demagnetization of the domain (demagnetization field). It describes how large magnetic domains break down into smaller domains in order to eliminate stray fields and achieve a lower overall magnetostatic energy. This process leads to the creation of 180° and 90° domain walls, marking the dividing lines between adjacent domains. Without any externally applied magnetic field, a single ferromagnetic crystal forms a domain structure as displayed in Fig. 2.1.

2.1.5 Magnetoelastic Energy

The magnetoelastic energy relates the elastic properties to the magnetic properties of electrical steel. This energetic term is particularly interesting for this

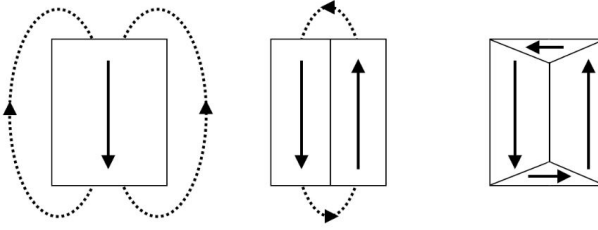


Figure 2.1: Minimization of the magnetostatic energy by the division of large domains into smaller subdomains with the creation of 180° and 90° domain walls.

thesis as it describes the deformation of the material and its impact on the magnetic properties. When external load is applied, the magnetic domain structure of the material changes.

The distribution of the magnetic dipoles in the material under externally applied field is determined by the balance between interacting terms in the energy equation (2.1). By its nature, the total free energy of the system will strive towards minimization.

Due to the presence of imperfections in the crystal lattice, the motion of the domain walls during the magnetization process is hindered. Sources of imperfections may be irregularities in the lattice such as intruding atoms (inclusions) or structural dislocations. These irregularities can lead to domain wall pinning. Around this pinning site, the atoms in the lattice show a significantly higher resistance to a 180 degree magnetization reorientation.

2.2. Hysteresis in ferromagnetic materials

2.2.1 Hysteresis Loop

Domain theory describes how the magnetization of each microscopic domain is always in saturation, uniform and (ideally) oriented either parallel or anti-parallel to an externally applied magnetic field. On a larger scale, this behaviour translates into a more continuous transition of the magnetization when the ferromagnetic structure is excited with an external field. When ferromagnetic materials are wielded in electrical machines, they are exposed to varying magnetic fields. These fields originate from electric currents running through excitation coils or by the movement of permanent magnets attached to rotating parts of the machine. The domain structure alters significantly under the influence of these external fields while the material strives to maintain its minimal energy state. In Fig. 2.2, it is shown how soft magnetic materials exhibit hysteretic behaviour. At point *a*, the material is in a demagnetized

state in which all domains are randomly oriented. When a uniform external field (H) with increasing magnetic field strength is applied, the magnetic flux density (B) also increases following a virgin magnetization curve. This simultaneous increase happens in three stages. First, between points a and b , 180° domain wall motion occurs so that domains parallel to the field gain volume at the expense of antiparallel domains. In the second stage, between point b and c , the 90° domain wall motion takes place until the entire domain is uniaxially magnetized. The 180° and 90° domain wall motions develop at low excitation fields and are hindered by dislocations within the material structure. These dislocations result in pinning of the domain walls and, once overcome, cause a sudden and irreversible change of the magnetization state known as a Barkhausen jump. On a macromagnetic level, these jumps can be detected in the form of Barkhausen noise. The last stage, between points c and d , is introduced when domain rotation occurs towards the direction of the external magnetic field. Any further increase of the magnetization requires the magnetic domains to be rotated away from their easy magnetization direction, which requires more energy from the external magnetic field. In this final stage, the increase in B requires drastically more H . The material approaches its saturation flux density. Beyond this point, any further increase in magnetic flux density is only due to increases of H . At point d , the material is in saturation. When the external magnetic field decreases, the magnetic domain structure will not return to its original state. A different path is followed, described by the curve from point d to point e . At $H = 0$, the material will retain a certain remanent magnetization. This feature indicates that domain wall motion is an irreversible process, while domain rotation is not. The remanent magnetization enables soft magnetic materials to be used in memory storage applications, but is usually undesirable in electric machines. From point e to f , the magnetic field strength orientation is reversed to the coercive field strength H_{coer} . This is the magnetic field strength necessary to counteract any remanent magnetism so that the total flux density equals zero. The crystallographic defects and impurities in the lattice that were initially overcome by the external field are now the main contributors to the value for H_{coer} . With a further decreasing field, the curve can be described by phenomena similar to the ones describing the virgin magnetization curve, albeit with a different starting point. When the reversed saturation is reached, the process repeats itself. The initial magnetization state can only be reached with a demagnetization procedure or by heating the material to above its Curie temperature and subsequently cooling it down.

It is clear from this virgin curve that the magnetization behaviour of ferromagnetic materials is non-linear. The constitutive relation between B and H is described as

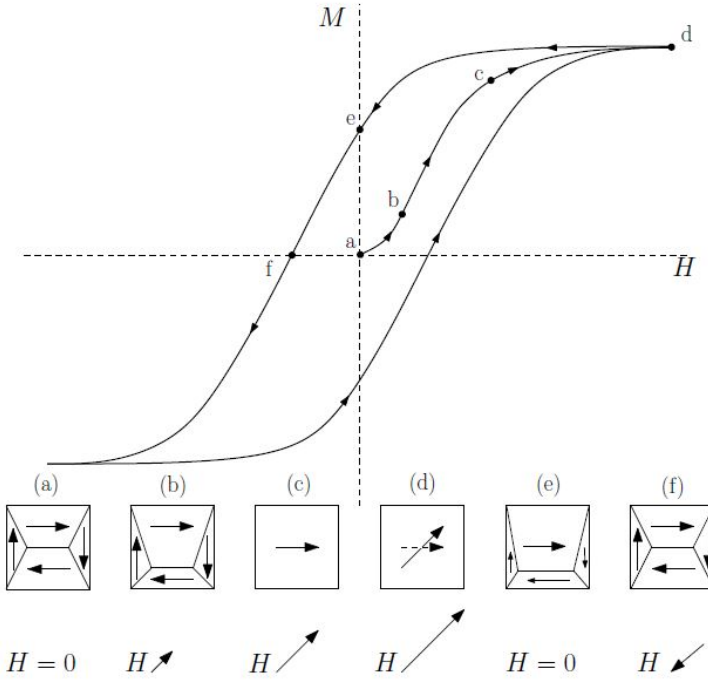


Figure 2.2: Illustration of a typical hysteresis loop with virgin magnetization curve and corresponding evolution of the domains under the influence of the external field [67].

$$\mathbf{B} = \mu_0 \mu_r(H) \mathbf{H} \quad (2.3)$$

where μ_0 is the permeability constant of vacuum ($4\pi e^{-7}$ H/m) and μ_r is the relative permeability. Ferromagnetic materials feature non-linear and saturation behaviour, which explains why μ_r in this expression is a function of the magnetic field strength H .

When considering the hysteresis loop as a system, the magnetic field strength $H(t)$ would be the input and the flux density $B(t)$ would be the output. In Fig. 2.2, a typical hysteresis loop is shown where the input of the system is purely sinusoidal with a constant amplitude and frequency. In realistic applications, the input may not be purely sinusoidal depending on the type of application and considered location on the steel. When the $H(t)$ input is not sinusoidal but unidirectional or when it contains higher order frequencies, the complexity of the system is further increased. In this case, properties such as higher order loops, wipe-out (or memory due to consecutive extreme input values), congruency and accommodation all contribute to the determination of the system

output. Many models have been proposed that model the complete hysteresis loop and its properties, the most popular among them being the Preisach Model. This model assumes the existence of elementary dipoles (or hysterons) which represent the magnetic domains. These dipoles can only be magnetized to saturation in either the negative or positive direction. However, the magnetic field values for which the output value switches from positive to negative, or vice versa, are unique for each hysteron. The total magnetization is defined by the weighted sum of the hysteron magnetizations. This model succeeds accurately in simulating the wipe-out property and congruency. In practice, the identification of the Preisach model parameters requires a large collection of first order reversal curve measurements.

2.2.2 Single Valued BH curve

It is clear that hysteretic behaviour is quite complex and difficult to model. A simple and frequently used alternative for modelling the permeability or BH curve of a material is the quasi-static normal single valued BH curve. This curve is based on measurements of several quasi-static hysteresis loops with incrementing peak magnetic field strength (Fig. 2.3). The peak values for the BH -pairs are then used to construct the single valued curve. It must be noted that this constructed curve doesn't exactly represent the actual quasi-static states occurring in the material. A more accurate single valued relation is known as the anhysteretic curve [1]. The BH datapoints on this curve are obtained by demagnetizing the material with an input magnetic field which has an incrementally increasing DC bias. This approach yields a more physically accurate representation of the anhysteretic material states in a given grade of electrical steel. However, it requires a significantly longer time to obtain the data points and the results are only marginally more accurate than the normal single valued BH curve. Throughout the rest of this thesis, BH curves are consistently constructed corresponding to the normal single valued BH curve.

2.2.3 3 Parameter BH curve model

According to [55], a convenient model for describing the single valued BH relation is a three parameter model. The three parameters are B_0 , H_0 and ν

$$\frac{H}{H_0} = \left(\frac{B}{B_0} \right) + \left(\frac{B}{B_0} \right)^\nu \quad (2.4)$$

According to this model, the relative permeability can be expressed as a function of B by

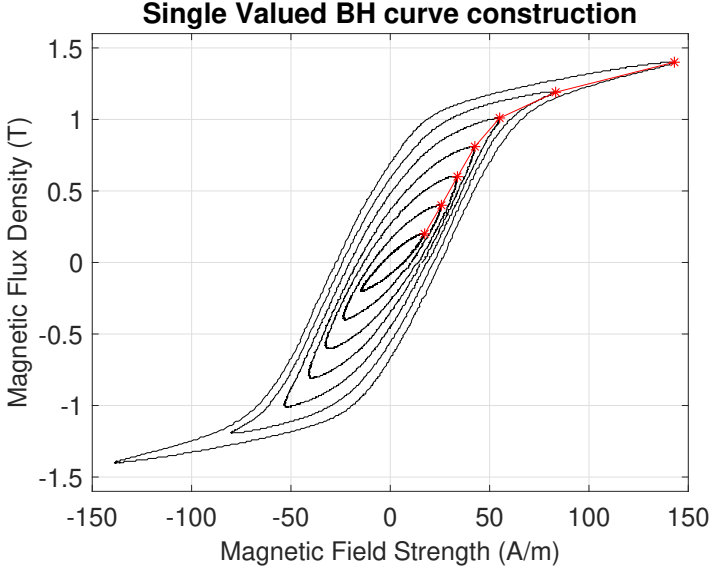


Figure 2.3: Measurements of M100-23P quasi-static hysteresis loops with incrementing peak magnetic field strength and subsequently constructed single valued BH -curve (asterisks).

$$\mu_r(B) = \frac{B_0}{\left(H_0\mu_0 \left(1 + \left(\frac{B}{B_0}\right)^{\nu-1}\right)\right)} \quad (2.5)$$

With the purpose of implementing the 3 parameter model to FEM simulations, it is necessary to express the BH curve properties in such a way that the relative permeability in (2.5) and its B -derivative are continuous and smooth functions. This is true for the 3 parameter model, so when the FE-simulation is run, the solution will be smooth without any numerical instabilities that could lead to local inaccuracies in the simulation. For a typical NO steel grade, the BH -pairs of a single valued curve might look like Fig. 2.4. The model parameters corresponding to this curve are $B_0 = 1.33$, $H_0 = 97.88$ and $\nu = 20.07$. It must be noted that this model does not accurately model the magnetic permeability at low values for magnetic field strength because it linearizes the Rayleigh zone. In Fig. 2.5, this shortcoming is displayed. The Rayleigh zone refers to the area on the BH curve near the demagnetized state. In Fig. 2.2, the magnetic properties in this zone are noticeable between points a and b . Here, the initial increase in magnetization is slower with increasing H . When the material is in the demagnetized state, and the H -field is slightly increased, the B -field will

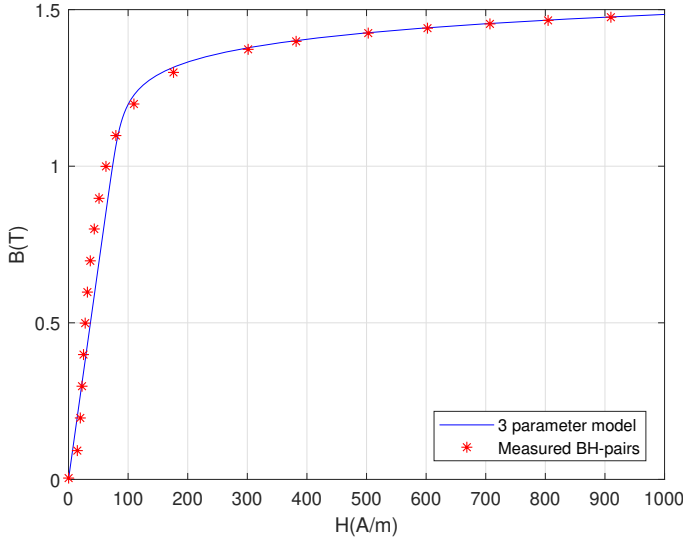


Figure 2.4: Datapoints obtained for constructing a single valued BH curve for NO27 grade electrical steel. The full line is plotted using the 3 parameter model with fitted coefficients.

initially be reluctant to increase do to fact that the 180° domain wall motion is impeded by pinning sites.

2.3. Statistical Loss Theory

Due to its simplicity, the most popular model describing power losses in magnetic cores under sinusoidal external magnetization is the Steinmetz's equation (2.6). This equation formulates the total core losses as a function of the excitation frequency and the peak magnetic flux density. k , a and b are material coefficients. These coefficients are usually fitted empirically.

$$P_{tot} = k f^a B^b \quad (2.6)$$

However, it is well known that a better and more physically accurate way to describe the total losses is to consider the magnetization process on two separate levels, namely the static losses and the dynamic losses. The static losses are related to the energy dissipated in the material when the excitation magnetization is quasi-static (i.e. with very low frequency, ideally below 1 Hz). The dynamic losses contribute to the total losses when the excitation frequency increases. This approach was found to yield better results and it acknowledges the different physical processes during magnetization. A physically reason-

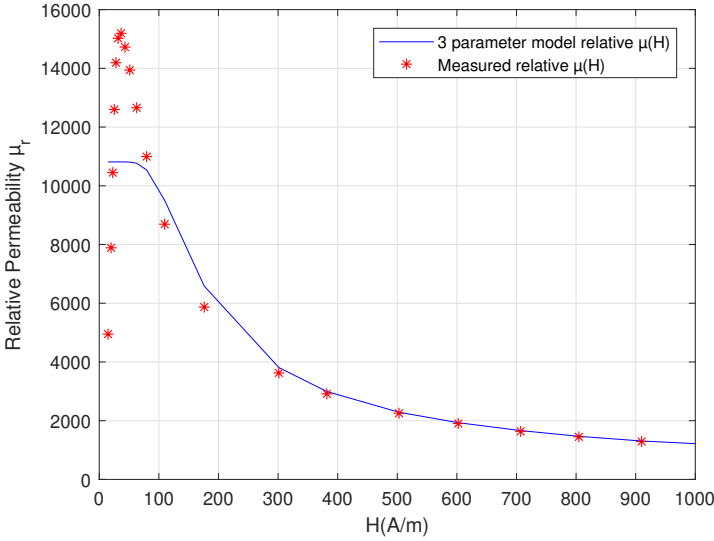


Figure 2.5: A comparison of the measured and modelled relative magnetic permeability as a function of magnetic field strength H for NO27 grade electrical steel.

able and universally adapted theory of understanding and modelling these losses is often referred to as the Statistical Loss Theory (SLT), which was developed by Bertotti et al. [11]. This theory supports the separate contributions of the static and dynamic losses to the total loss, but also further differentiates the dynamic losses into classical (eddy current) losses and an additional excess loss. The statistical approach to the magnetization process is not just an empirical model, but describes the space-time evolution of the fundamental Barkhausen jumps and the irregular movement of the domain walls. The importance of this model is difficult to underestimate, because it provides a robust and well-founded framework for understanding the power loss phenomenon in soft magnetic materials and its relation to frequency, induction level as well as microstructural magnetic properties such as grain size and magnetic domain size. In addition, the SLT acknowledges the stochastic nature of the magnetization process due to the domain wall motion and magnetization reversal. SLT elaborates the separation of losses principle and states that iron losses can be divided into three components,

$$P_{tot} = P_{hyst} + P_{cl} + P_{exc} \quad (2.7)$$

When analysing the total core losses experimentally, different loss components are discernible. Fig. 2.6 shows the relation between the frequency and

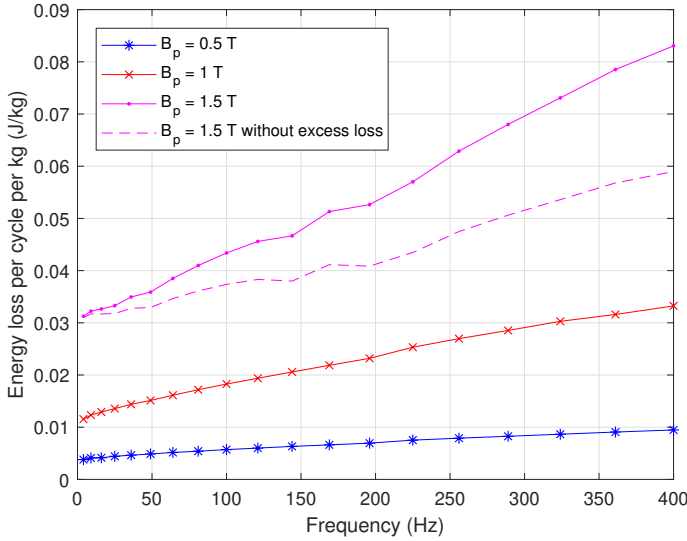


Figure 2.6: Core loss data from NO27 grade steel at several frequencies and peak flux density values. For $B_p = 1.5$ T, the theoretical total loss is also plotted without considering the excess losses.

the total losses in J/kg for NO27 grade electrical steel, which has a lamination thickness of 0.27 mm and an electrical resistivity of $5.9 \times 10^{-7} \Omega \cdot \text{m}$. At quasi-static excitation frequency, only the hysteresis component is prominent. With increasing frequency, the total core losses increase. However, this increase can not be explained only by the classical (eddy current) loss. An additional excess loss component is needed to complete the theory. In Fig. 2.7, the different relations between the loss components and the frequency is highlighted. It should be noted that in Figs. 2.6 and 2.7, the core loss is expressed in terms of energy loss per cycle per kg, and not in Watt per kg as is the case in the other graphs displaying loss data.

2.3.1 Hysteresis Loss

The hysteresis loss P_{hyst} originates from the microscopic domain wall movement occurring during Barkhausen jumps. These jumps cause locally induced electric currents (commonly called eddy currents). The energy stored in these eddy currents during a magnetization cycle is very quickly dissipated and is related to the resistivity of the material and the velocity and amplitude of the domain wall motion. Barkhausen jumps are, by their nature, discontinuous and randomly distributed in the material structure which makes them

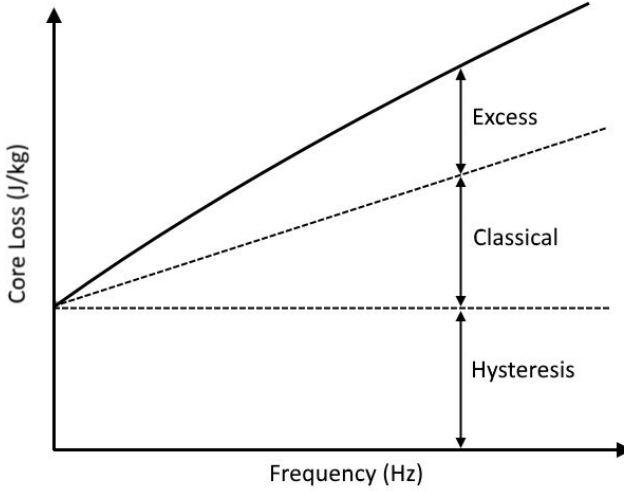


Figure 2.7: Core losses per cycle to indicate the different loss components and their relation to the excitation frequency.

well suited for a statistical description. The hysteresis energy loss can be calculated from the area of the quasi-static BH loop, multiplied by the excitation frequency:

$$P_{hyst} = W_{hyst}(B_p) f \rho^{-1} \quad (2.8)$$

In this expression, W_{hyst} is a material related parameter.

2.3.2 Classical Loss

The classical (also called the Foucault or Eddy Current) loss term explains the eddy currents on a macroscopic level. These eddy currents tend to counteract any change in the average magnetization of the material and are therefore circulating throughout the entire material structure. Consequently they manifest themselves at a larger spatial scale and time scale where the material can be considered homogeneous and uniformly magnetized. In case the induction waveform is sinusoidal, the classical loss can be calculated as

$$P_{cl} = \frac{B_p^2 f^2 \kappa d^2 \pi^2}{6\rho} \quad (2.9)$$

with B_p the peak flux density, f the excitation frequency, κ the electrical conductivity and d the electrical steel lamination thickness. This expression is only valid when the magnetic flux density can be considered homogeneously distributed over the material cross section. However, with increasing magnetization frequency, the skin effect disturbs this homogeneous distribution and (2.9) becomes

$$P_{cl} = \frac{B_p^2 f^2 \kappa d^2 \pi^2 F(\zeta)}{6\rho} \quad (2.10)$$

with the correction term $F(\zeta)$ defined by

$$F(\zeta) = \frac{3(\sin(h\zeta) - \sin(\zeta))}{\zeta(\cos(h\zeta) - \cos(\zeta))} \quad (2.11)$$

with ζ defined as

$$\zeta = \frac{d}{\sqrt{\frac{2}{\omega\kappa\mu}}} \quad (2.12)$$

where $\omega = 2\pi f$ and μ the magnetic permeability.

2.3.3 Excess Loss

Hysteresis loss and classical loss both have their contributions to the total core loss in the material, but numerous researchers have observed that there is a deviation between the total losses and the losses calculated from hysteresis and classical eddy current effects. Also, the frequency dependency of this loss deviation appeared to be different than the frequency dependence of classical loss. This additional loss term is referred to as the excess loss and its origin can be situated between the microscopic area of the hysteresis loss and the macroscopic area of the classical losses. A physical interpretation of these losses was given by Bertotti based on the interaction between moving domain walls. It is the dynamic contribution to the total core losses which originates from the elementary domain magnetization reversals. The excess loss can be expressed for a sinusoidal flux pattern as described in [34]

$$P_{exc} = 2B_p f (\sqrt{(n_0 V_0) + 16\kappa G S V_0 B_p f} - n_0 V_0) \rho^{-1} \quad (2.13)$$

where n_0 and V_0 are microstructural parameters, κ is the conductivity, G is a dimensionless constant (≈ 0.1356), and S is the sample cross section. The microstructural parameter V_0 has the dimensions of a magnetic field and is known to vary at higher values of B_p . n_0 represents the amount of simultane-

ously active magnetic objects at quasi-static frequency under magnetic field V_0 .

2.3.4 Loss Modelling

A practical and accurate loss model acknowledges the principle of loss separation and considers the specific relation between each loss component to the peak flux density B_p and frequency f [9]. Each component is also related to the total loss using loss coefficients according to

$$P_{tot} = C_{hyst} B_p^\alpha f + C_{cl} B_p^2 f^2 + C_{exc} B_p^{1.5} f^{1.5} \quad (2.14)$$

This model characterizes the core losses specific to an electrical steel grade based on 4 parameters, namely α , C_{hyst} , C_{cl} and C_{exc} . For a typical grade of electrical steel, the relation between the peak flux density and total core losses for different frequencies is shown in Fig. 2.8. For this material, the core loss parameters when loss values are expressed in W/kg are $\alpha = 1.68$, $C_{hyst} = 0.0172$, $C_{cl} = 1.57e-4$ and $C_{exc} = 5.18e-4$. In this example, the parameters were identified using an inverse problem approach using the MATLAB *fmincon* toolbox. The graph shows an accurate correspondence between the measured core losses and the simulated losses when the model in (2.14) is fitted with the loss parameters.

However, it must be noted that the approach used here is the frequency-approach of the Bertotti model. This means that the separation of loss model - which uses the peak magnetic flux density as a variable - is only valid when the magnetic flux density waveform is sinusoidal. In realistic applications however, purely sinusoidal excitation rarely occurs. Especially for the hysteresis component, the version of the Bertotti model used in this thesis will result in an underestimation when the magnetic flux density waveform is not sinusoidal. When this waveform contains minor loops as a result of local extreme values of the magnetic field strength, the hysteresis loss component will be higher than expected in the purely sinusoidal model. To accommodate non-sinusoidal waveforms, alternative models exist in which the classical and excess loss component depends not on the peak magnetic flux density, but on its time-derivative. Also, when minor loop can occur, the hysteresis loss component should be calculated differently, e.g. by using the Preisach model. For the work presented in this thesis, it could be argued that the difference between both model types is not especially relevant because the goal is to investigate manufacturing effects on the core losses. It will become clear in the following chapters that manufacturing techniques mostly impact the hysteresis loss component and the excess loss component. The electrical conductivity is not likely to change as a consequence of - for example - punching or welding. Therefore, it could be argued that the impact of applying non-sinusoidal

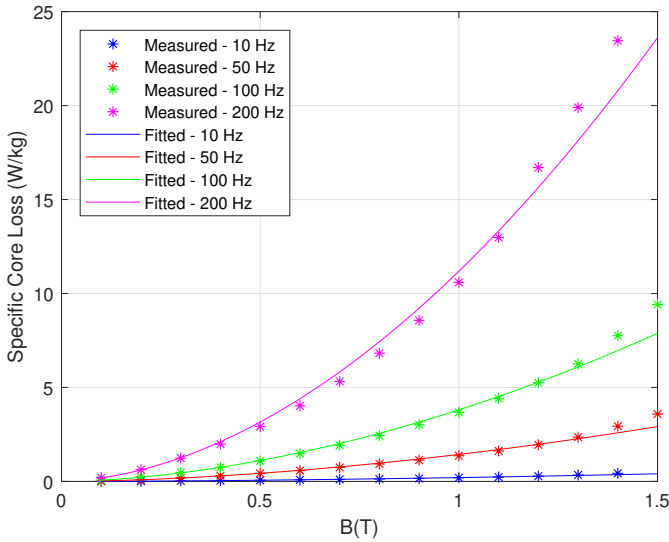


Figure 2.8: Measured core losses (datapoints) at several excitation frequencies compared to simulated core losses (datacurves) with fitted loss coefficients for NO27 grade electrical steel.

waveforms – with the exception of minor loops – would have a rather limited impact on the conclusions that were mentioned in the thesis.

2.4. Magnetic Measurements

Each grade of electrical steel has its own specific magnetic and loss properties. Commercially available electrical steels are classified according to these properties. In order to identify the specific properties, magnetic measurements are needed. 'Magnetic measurements' is the collective term for measurements related to the material specific magnetic properties such as magnetic permeability, quasi-static hysteresis loop and specific core losses. These measurement data can then be used for modelling the magnetic material behaviour of the steel grade. It is necessary to achieve a high measurement accuracy in order to achieve an acceptable model parameter identification. In this section, the basic principles for obtaining magnetic measurements data are described. Afterwards, several variations on magnetic measurement techniques are described. The standardized technique for performing magnetic measurements is the Epstein frame method. When alternative material geometries are available, variations to the Epstein frame method can also be used. An overview

will be given of the different material geometries that can be characterized using global magnetic measurements.

2.4.1 Basic Principles for Magnetic Measurements

The magnetic properties are derived from the simultaneous measurement of the magnetic flux density and the magnetic field strength. In a closed magnetic circuit, these quantities can be measured by winding a primary and secondary conducting coil as displayed in Fig. 2.9. The electric current through the primary winding generates a homogeneous magnetic field in the magnetic circuit. Assuming there is no air flux, the average magnetic field strength in the core of the circuit is determined by measuring the primary coil current $i(t)$ and applying Ampère's law

$$H_a(t) = \frac{N_1 i(t)}{l} \quad (2.15)$$

with l the average magnetic path length and N_1 the amount of turns in the primary winding. The imposed magnetic field strength excites the ferromagnetic material which in turn amplifies the magnetic flux density in the core. The magnetization of the steel and the magnetic field strength constitute the total magnetic flux. A time varying magnetic flux generates a voltage in the secondary coil. This voltage can be measured and, according to Faraday's law, is related to the average magnetic flux density in the core by

$$V_2(t) = -N_2 A \frac{dB_a(t)}{dt} \quad (2.16)$$

with B_a the average magnetic flux density over the magnetic core cross section A and N_2 the amount of turns in the secondary winding. Consequently, B_a is determined as

$$B_a(t) = \frac{-1}{N_2 A} \int^t V_2(t) dt \quad (2.17)$$

Measuring the magnetic properties essentially implies measuring B_a and H_a simultaneously. The double coil setup results in global average values of the magnetic properties as this measurement technique assumes uniform magnetic field values across the circuit cross section. In this context, these measurements are referred to as global magnetic measurements because they yield no information about the local magnetic properties in the magnetic circuit or the magnetic flux distribution in the cross section.

Performing magnetic measurements can be done using a data acquisition (DAQ) system which can control the (primary winding) excitation current and at the same time measure the voltage in the secondary winding. Fig. 2.10

shows an schematic overview of a setup used for magnetic characterization based on global magnetic measurements. A current control signal is created using MATLAB software and transmitted to the amplifier. This amplifier generates the current waveform for the primary winding in the magnetic circuit. Using the current sensing resistor (CSR), a feedback signal for the excitation current is sent to the DAQ control system. The secondary voltage is measured either directly and afterwards digitally integrated to compute the magnetic induction B_a or integrated analogously using an operational amplifier circuit. In this thesis, all magnetic measurements were done using a National Instruments DAQ-card connected to a CPU running MATLAB software for Magnetic Measurements which was developed at Ghent University. A Kepco 50V/8A Bipolar Operational Amplifier was used for generating the controlled excitation field. Fig. 2.11 displays two waveforms measured on NO27 grade electrical steel at 1 Hz excitation frequency. The power losses (W/kg) specific to the magnetization of the core can be calculated as

$$P_{tot} = \frac{1}{T\rho} \int_0^T H_a(t) \frac{dB_a(t)}{dt} dt \quad (2.18)$$

The hysteresis loop appears when both waveforms $B_a(t)$ and $H_a(t)$ are plotted against each other as is shown in Fig. 2.12. At quasi-static excitation frequency, it can be assumed that the core losses only consist of the hysteresis energy losses. In this context, the hysteresis energy losses (J/m³) can be approximated by the surface of the quasi-static hysteresis loop:

$$W_{hyst} = \oint H_a(B_a) dB_a \quad (2.19)$$

2.4.2 Epstein Frame Method

The Epstein test has been standardized in the IEC norm 60404-2. It is the most ubiquitous way of characterizing magnetic properties of electrical steel. It applies the principles described in the previous section on an Epstein frame with standardized dimensions (Fig. 2.13). Strips of electrical steel need to be manufactured with a fixed width of 30 mm and length of at least 280 mm. A multiple of four strips should be placed in the frame and the corner regions should be alternately overlapping. In order to reduce the airgap between the strips in the overlapping regions, weights should be placed on the corners.

There are some disadvantages related to the Epstein frame. The principles of global magnetic measurements assume uniform magnetic properties and homogeneous magnetization in the sample. However, in the overlapping regions of the Epstein frame, the magnetic flux temporarily travels through the

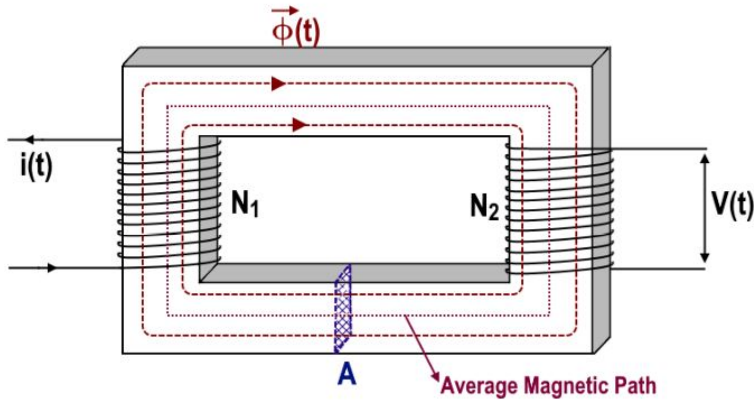


Figure 2.9: A closed ferromagnetic circuit with primary excitation winding and secondary pickup coil.

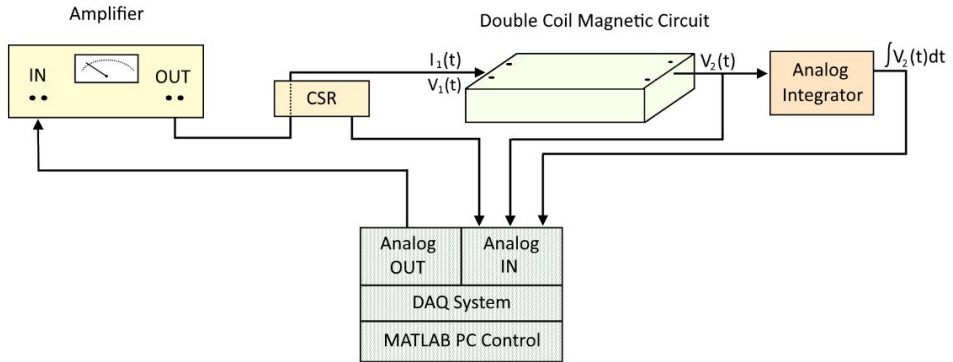


Figure 2.10: Setup for performing magnetic measurements using a DAQ control system, power amplifier, current sensing resistor (CSR) and analog integrator circuit.

air gap. This implies that the voltage in the secondary coil is affected by the magnetization of this air gap.

It is well known that the properties of GO and NO electrical steel are anisotropic. For GO steels, this is obvious since they are tailored specifically with optimized properties in the grain oriented direction. For NO steel, this effect is unintentional but nevertheless present in most commercially available steels. This anisotropy is introduced during the final cold rolling operations. The magnetic permeability is usually higher and the core losses are

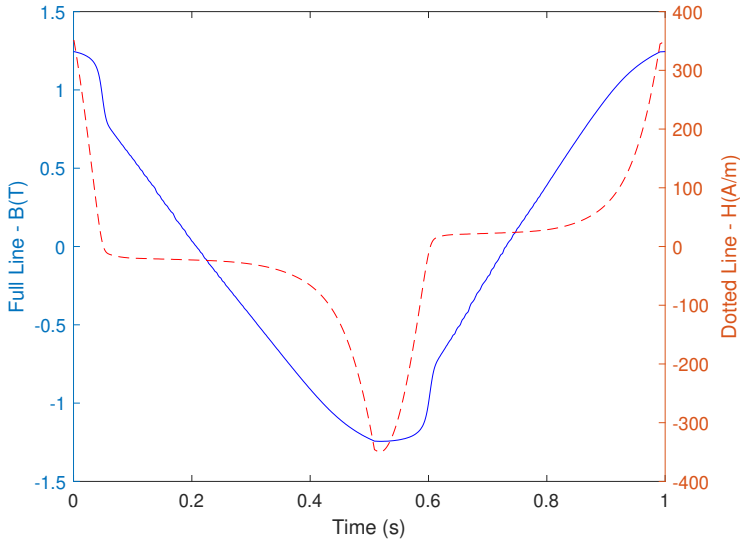


Figure 2.11: Typical measured waveforms for magnetic field strength $H(t)$ and magnetic induction $B(T)$ obtained at 1 Hz. These waveforms are obtained using the magnetic measurement setup when the magnetic circuit core consists of soft ferromagnetic material.

lower in the rolling direction (RD) than in the perpendicular (transverse) direction (TD). When measuring the magnetic properties of NO steel using an Epstein frame, a good practice is to insert both strips that were cut in RD and in TD in equal amounts. This way, the effect of anisotropy is averaged in the measured global magnetic properties.

The determination of the average magnetic path length, which is a key variable in the calculation of the magnetic field strength (2.15), is fixed to 940 mm in the Epstein method. However, it is well known that this average magnetic path length is not fixed but depends on the peak flux density, excitation frequency and anisotropy.

2.4.3 Single Sheet Tester

Although the principles of global magnetic measurements are the same as for the Epstein method, the single sheet tester provides some key advantages and opportunities. In this configuration, only one test sample is needed. The sample is placed in a double concentric coil and fixed between two U-shaped ferromagnetic yokes at the ends. One coil will act as the excitation (primary) coil while the other is the secondary coil. The double yoke formation is necessary for closing the magnetic circuit and ensuring that a minimum amount of mag-

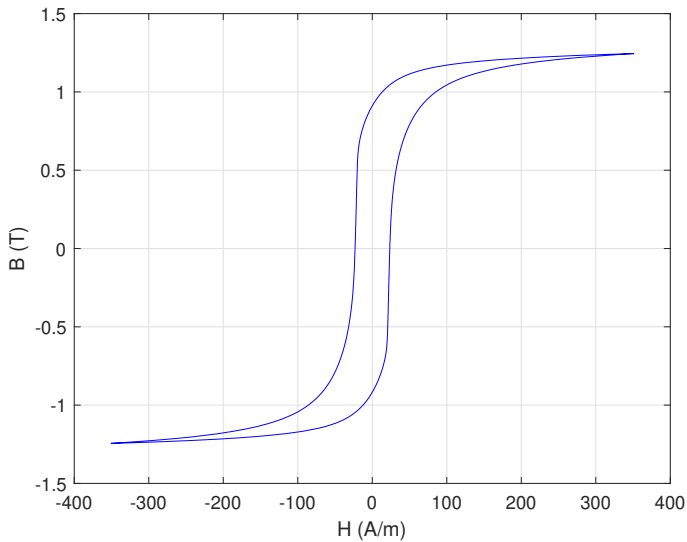


Figure 2.12: Typical hysteresis loop constructed by plotting the B - and H -waveforms from Fig. 2.11.

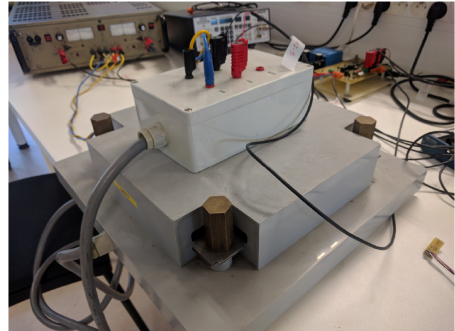
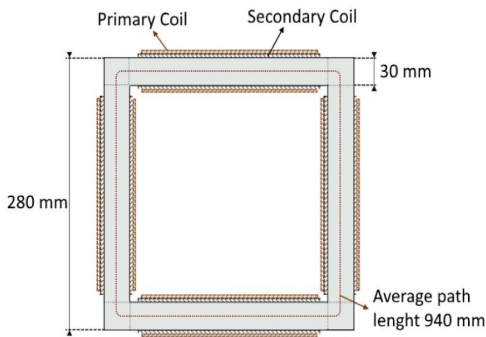


Figure 2.13: Dimensions and actual picture of a standardized Epstein frame. The strips of electrical steel are placed in the frame with the corners overlapping as shown in the photo.

netic flux travels through air. An illustration of the cross section is displayed in Fig. 2.14. Additionally, a separate concentric coil might be placed in series with the coils in the setup. This extra coil should not enclose any material and act as an air flux compensator for the setup. The air flux compensation coil should preferably be placed out of the near vicinity of the yoke and the electrical steel sheet so that the magnetic field generated in this coil is not influenced by

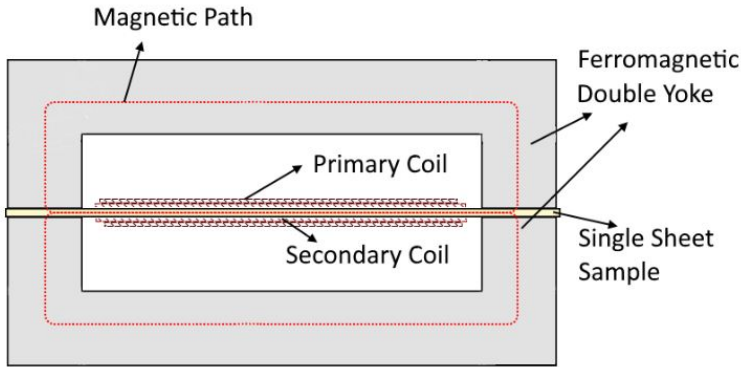


Figure 2.14: Single sheet tester setup with concentric excitation and secondary coil and double yoke.

ferromagnetic material and only encloses the air. This way, the measurements results exclude any effects of magnetization of the air.

When using the SST, only the magnetic properties along the central axis of the sample are measured. When the double yoke configuration is positioned accurately and with the least amount of air gap possible, the parasitic effects of corner overlapping can be tackled. The SST setup allows easy access to the sample when the effect of stress on the magnetic properties is measured.

One of the main disadvantages of using the SST is the difficulty that arises in determining the average magnetic path length. Commonly, this path length considered is equal to the length of the sample between the double yokes. However, the value depends on several factors which makes it difficult to validate the accuracy of the SST setup.

2.4.4 Ring Core Measurements

In IEEE standard 393-1991, an alternative measurement setup is described. In this standard, global magnetic measurements are obtained using toroidal samples wound with a double concentric coil. A ring core setup is shown in Fig. 2.15. This technique relies on the same principles as the previous two techniques. However, in this case the air gap is avoided and the magnetic flux path closes entirely through the material under investigation. One significant drawback to this technique is the need for a custom winding for each sample. Preparing the setup requires manually winding the primary and secondary coils. Any number of samples may be stacked before winding. The ring core geometry is well suited for the investigation of NO electrical steels since it

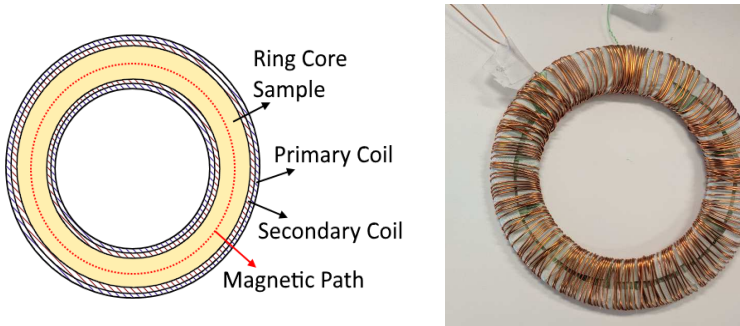


Figure 2.15: Illustration and actual ring core sample with concentric excitation and secondary coil.

inherently averages any anisotropy there might exist in the material. The average magnetic path length is defined along the circumference of the circle with diameter equal to the average of the inner and outer diameter of the ring core sample. This type of setup closely resembles the stator yoke geometry typically found in electrical motors and is therefore convenient for studying manufacturing effects such as interlocking or welding.

2.4.5 Simplified stator geometries

Although the previously described geometries for magnetic measurements are standardized and provide a useful benchmark for material researchers when comparing different grades of steel, it could be argued that these geometries are rather unrelated to realistic electrical machine geometries. For example, in the Epstein frame, the magnetic flux path is interrupted in the regions where the strips overlap. Therefore, the measured magnetic properties are not entirely derived from flux travelling through material. A similar problem arises when using the SST setup. Furthermore, the issue of anisotropy between different cutting directions for the SST might lead to over- or under-estimations of magnetic properties. However, in the ring core setup, both of these problems are addressed. The magnetic flux follows a path continuously flowing through the steel and in all 360° directions. Consequently, this setup would yield averaged results which are more closely related to the actual material properties of the steel. Despite this improvement and the relatively simple geometric shape of the ring core setup, there can still be a discrepancy between the setup and the realistic material as is occurs in machines due to a difference in cutting effect. Also, a set of ring cores might not always be available or can not be manufactured. In those cases, it is possible to use the complete stacked stator geometry for modelling its magnetic properties. This

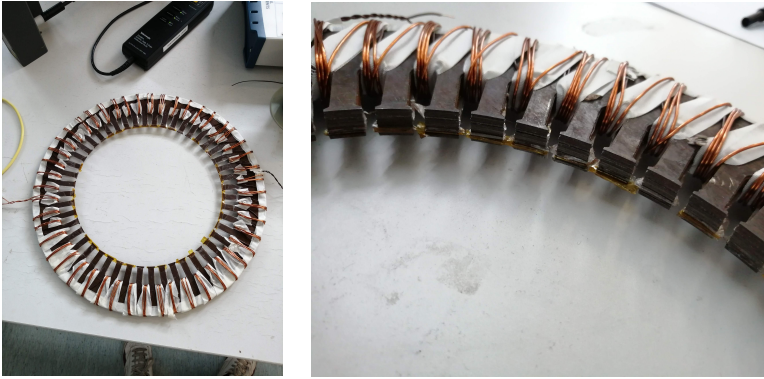


Figure 2.16: Illustration and wound stator core stack with concentric excitation and secondary coil for performing magnetic measurements.

can be achieved by means of a concentric double coil wound around the outer edge of the stator yoke and between the teeth, as was done in Fig. 2.16. The same field-metric measurement principles as in the previous geometries are still valid. Measuring magnetic properties this way entails the incorporation of any cutting or joining degradation in the material properties. Similar to the ring core geometry, the average magnetic path length can be derived from the average circumference of the outer and inner yoke diameter. However, it must be noted that this is only an estimation and the actual average path length is slightly higher due to the presence of the teeth. In the yoke areas where a tooth is present, the flux density locally decreases and the magnetic path elongates, as demonstrated in the simulation in Fig. 2.17.

2.5. Inverse Modelling

The previously described measuring techniques result in global values for the magnetic properties in electrical steel laminations. Measurement data in itself provides interesting information about the behaviour of the material under certain circumstances. However, added value can be derived from measurement data when they can parametrize a predefined model for a more complex application. When designing electric machines, the simulations are usually solved using predefined material parameters corresponding to a built-in material model. With the goal of incorporating the manufacturing effects into the design stage of electrical machines, it is necessary to have a robust technique for accurately parametrizing the models which describe magnetic material behaviour. The underlying physical relations between the effects of manufacturing and magnetic properties of steel are complex and far from com-

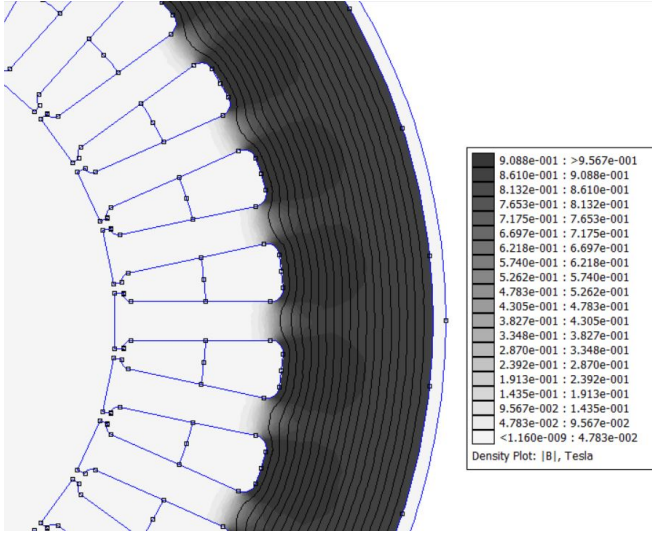


Figure 2.17: Finite Element Simulation of wound stator geometry with flux lines displayed. Near the teeth, a local minimum appears in the flux density distribution.

pletely described in literature. However, measurement data on these effects is abundant. It is therefore evident that the process of inverse modelling is appropriate in solving these problems. Inverse modelling is a general technique for determining model parameters when only observation data (i.e. magnetic measurement data) is available.

In practice, applying an inverse modelling methodology for fitting the model parameters implies iteratively simulating the model and afterwards comparing the simulation data to the measurement data. After each iteration, the deviation between the measured and simulated data is quantified in an error function. Subsequently the model parameters are updated and the simulation is repeated until the error function reaches a minimal required value and the model parameters are optimized.

Depending on each specific type of problem, the most appropriate optimization technique can be chosen. The optimal parameter set γ should be found for which the simulations correspond most accurately to the measurements. The least squares optimization technique for calculating the error function is well suited for this purpose. A general expression for this error function is

$$E(\gamma) = \sum_{n=1}^N ||x_{simulated}(k_n, \gamma) - x_{measured}(k_n)||^2 \quad (2.20)$$

The simulation data in this thesis will be based on variations of the three-parameter BH -curve model (2.4), the separation loss model (2.14) or obtained from numerical electromagnetic simulations. In [1], a detailed investigation is done on inverse problem algorithms for electromagnetic applications.

2.6. Machine Modelling Techniques

The dimensioning of the electrical and magnetic circuits for an electrical machine can be done in several ways. Analytical functions can be found in literature for predicting the performance and behaviour of specific types of machines, but they are often too general and do not allow the investigation of the effect of every design parameter. Especially when the core material is anisotropic and has locally varying magnetic properties, global analytical functions are not applicable. Alternatively, machine designers use numerical techniques which are equipped with tools for more detailed geometrical and material models.

2.6.1 Finite Element Modelling

Finite Element Modelling (FEM) software provides helpful tools for calculating machine behaviour based on a full 2D or 3D geometric model of the machine. For electric motors, the field solution enables the calculation of the torque of the machine under various excitation regimes. FEM also allows the designer to assign individual material properties to each section of the machine. The field solution consequently depends on the specific magnetic properties in each part of the machine, making this technique especially useful for modelling manufacturing effects and simulating their effect on the performance of the machine. Commercial software packages (such as COMSOL, Ansys Maxwell, Altair Flux2D, Flux3D, Infolytica or JMAG) offer easy-to-use tools for building 2D and 3D electromagnetic machine models which can solve both electrostatic or dynamic simulations. Most of the simulations in thesis are executed using an open-source alternative called FEMM. However, FEM simulations can be computationally intense, especially when they are iterated multiple times in solving inverse problems.

2.6.2 Magnetic Equivalent Circuit

Magnetic Equivalent Circuit (MEC) modelling offers some advantages regarding computation time. Similar to the abstraction of electrical circuits into equivalent circuits, the magnetic core in electric machines can also be modelled using magnetic equivalent circuits. Each region of the machine is modelled with magnetic reluctances with specific geometric and material proper-

ties. These reluctances essentially define flux tubes for the propagation of the magnetic flux. The circuit diagram determines the connections between the reluctances in the network. However, in order to calculate machine performance indicators such as torque or core losses, analytical models should be used. The simplified Switched Reluctance Motor (SRM) prototype with aligned rotor can be modelled using MEC as displayed in Fig. 2.18. Each section of the machine is modelled using a magnetic reluctance. In the air gap, fringe flux may occur which can be accounted for using correction factors (i.e. Carter coefficients). The reluctances are related to the geometric dimensions of the machine. With each segment defined with a length l and cross section A , the reluctance is

$$\mathcal{R} = \frac{l}{\mu_0 \mu_r A} \quad (2.21)$$

The windings around the teeth generate a magnetomotive force (MMF) \mathcal{F} in the stator. According to Ampère's circuital law, this MMF is related to the reluctance proportional to the number of turns in the winding N and the current i applied

$$\mathcal{F} = N_1 i = \phi \mathcal{R} \quad (2.22)$$

Determining the machine performance under various excitation regimes implies solving the MEC model to determine the flux density in each segment and afterwards applying analytical formulae such as the core loss model (2.14).

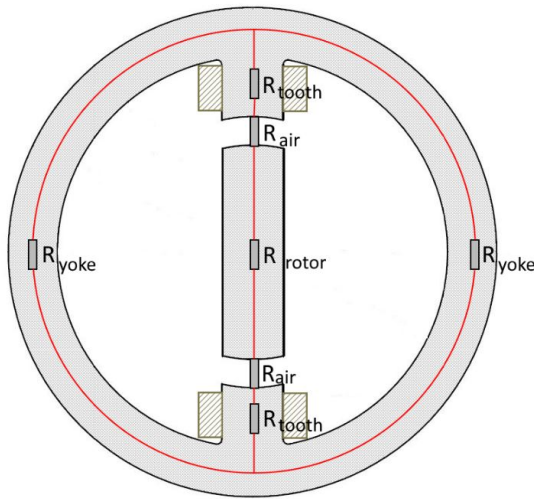


Figure 2.18: A simple MEC model of a Switched Reluctance Motor (SRM) with aligned rotor position.

2.7. Conclusion

This chapter contains a description of the underlying principles necessary for understanding the technique and value of magnetic measurements. A brief introduction to domain theory provides the necessary background to magnetization in soft ferromagnetic materials. A model is presented for characterizing the single valued BH curve of any specific electrical steel grade using 3 parameters. The method for characterization was demonstrated for M100-23P. Together with the single valued BH curve, the specific core loss is a fundamental value for characterizing any electrical steel. The specific core losses are typically modelled by dividing the total core losses into its components according to the SLT. A 4 parameter model can be used for capturing the relation between the total core losses P_{tot} , the peak magnetic flux density B_p and the excitation field frequency f . To demonstrate its practicability, the loss model parameters were fitted for NO27 grade steel using an inverse modelling approach.

A significant part of this chapter focused on techniques for performing magnetic measurements. The basic measurement principles are explained, followed by a series of measurement setups such as the Epstein frame, the SST and the ring core measurement setup. Alternatively, it is described how a realistic or simplified stator core can be used directly for measuring the average yoke properties. To conclude the chapter, two common machine modelling techniques are discussed. Both techniques are used in modelling applications further in this thesis.

3

Measuring the Impact of Manufacturing Effects

Each manufacturing process degrades the magnetic properties of the ferromagnetic core in a specific way. This is why it is difficult to generalize the degrading impact of, for example, laser welding on the core energy losses of an electrical machine. The added core losses depend on the steel grade, laser power, amount of welding seams and - as shown in [78] - welding speed. Nevertheless, in this chapter it is demonstrated using case studies how manufacturing effects affect the ferromagnetic core properties quantitatively for different stages of the manufacturing process. This way, a coarse estimation is given of the degree of degradation for various processes.

3.1. Impact of Cutting Technique on Magnetic Properties

3.1.1 Cutting effect on NO grade NO27

The degrading effects of cutting techniques on the magnetic properties can be measured using stator cores. For this experiment, the core geometry is a prototype switched reluctance motor with only two stator teeth (Fig. 3.1). Three variations of exactly the same geometry were manufactured using dif-

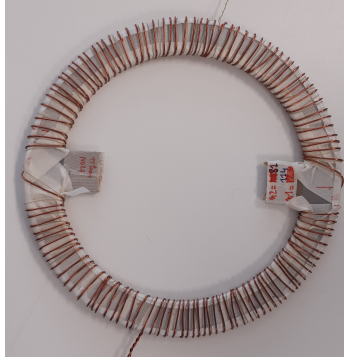


Figure 3.1: NO27 ring core geometry with two salient teeth and applied primary and secondary windings.

ferent cutting techniques. Two cores were laser cut by two different suppliers (Raytech and LCD Lasercut). The other core was created using a nibble punching process by Metagra. The nibble punching process produced a much lower geometric accuracy than the laser cutting process. The yoke outer and inner diameters are 200 mm and 160 mm, respectively. In Fig. 3.2, the impact of cutting is demonstrated using magnetic measurement results. The data indicates that nibble punched stator cores produce less core losses and have a higher relative permeability than the laser cut stator cores. Even though they were supplied by different manufacturers, both laser cut stators performed similar. At peak flux density level 1.5 T, the core losses are approximately 25 % lower in the nibble punched stator core than in the laser cut cores. The relative difference in core losses decreases when the material approaches magnetic saturation.

3.1.2 Cutting effect on GO grade M100-23P

In this experiment, the effects of various cutting techniques are measured on M10023P, a grain oriented grade electrical steel. Three different sets of Epstein strips were manufactured from the same mother coil. One set was laser cut by Raytech, one set was guillotine punched in the workplace at EELAB, and the last one was cut using water jetting by L&D Waterjet. The sole difference between each set of strips was the cutting technique. The observed differences in magnetic properties can consequently be attributed to this cutting technique. The strips are cut parallel to the grain oriented direction and placed in an Epstein frame with 700 primary and 700 secondary turns (Fig. 3.3). In Fig. 3.4, the results show the impact of cutting on the magnetic permeability and core losses. When measured using Epstein strips, water jet cutting has the least degrading impact on the magnetic properties of M100-23P. The permeability is

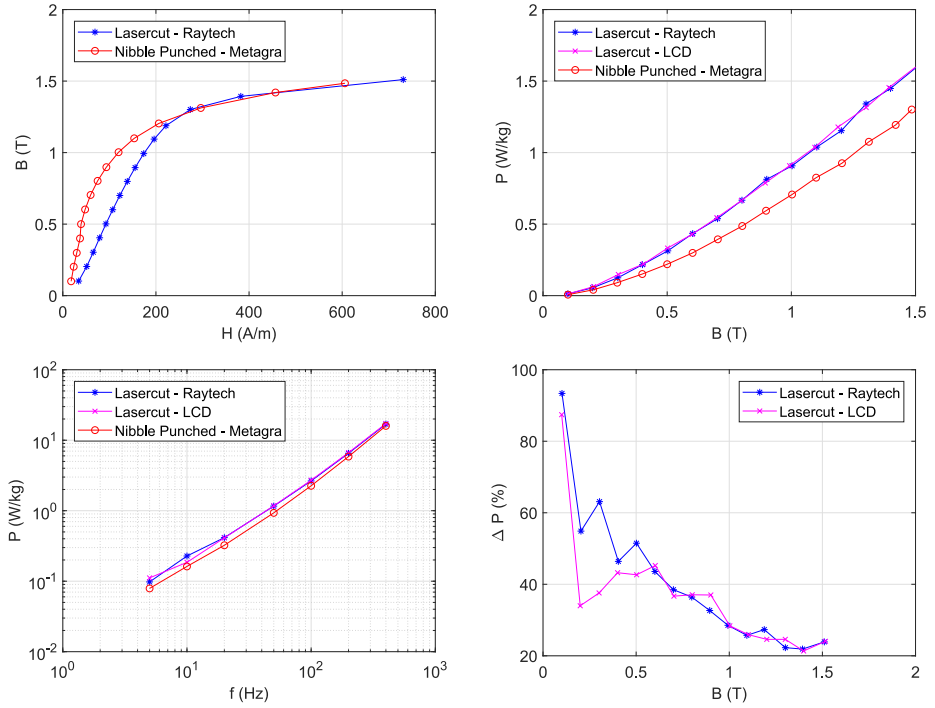


Figure 3.2: NO27 ring core geometry magnetic measurement data. Top left: Single valued BH curves. Top right: Core loss (at 50 Hz excitation field frequency) as a function of peak flux density. Bottom left: Core loss as a function of excitation frequency at 1 T peak flux density. Bottom right: Difference in core losses between both lasercut stator cores with respect to the nibble punched stator core. The core loss values were obtained at sinusoidal flux density waveform.

higher and the core losses are lower than for the laser cut or guillotine cut strips. Guillotine cutting causes only marginally larger degradation. The core losses are approximately 10 % to 20 % higher when the material is shaped with guillotine cutting than with water jet cutting. Laser cutting produces the largest magnetic degradation. At peak flux density level 1.5 T, the core losses are 37 % higher in the laser cut sample than in the guillotine cut sample. The comparison between laser cut and punched samples has been reported frequently in literature. An overview of these comparisons is given in the next chapter.

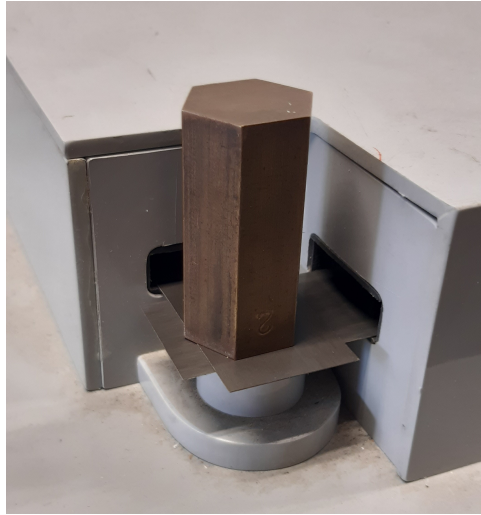


Figure 3.3: M100-23P 30 mm x 270 mm strips placed in an Epstein frame.

3.2. Impact of Annealing Process on Magnetic Properties

In this experiment, the effects of stress relief annealing are measured on M270-35A stator cores. Four stator cores are manufactured from the same mother coil. Two cores are laser cut, two cores are punched. One of the laser cut cores and one of the punched cores was treated with stress relief annealing. Each core was shaped and annealed by Protolam LLC. The geometry of the stator core is shown in Fig. 3.5. The yoke outer and inner diameters are 193.8 mm and 147.6 mm, respectively. This kind of geometry is suited for induction machines or permanent magnet synchronous machines. The primary and secondary windings are applied around the stator yoke and between the teeth. For each core, the primary winding consists of 120 turns and the secondary winding contains 30 turns. Only the magnetic properties of the stator yoke are measured. Assuming that the cutting process primarily impacts the edge material, the degrading impact will be larger in the tooth area. Nevertheless, this experiment shows the difference between cutting techniques and the annealing treatment in the yoke area. The main magnetic measurement results are shown in Fig. 3.6. The measurement data show that magnetic properties are least favourable in the laser cut stator core that has not been treated with stress relief annealing. The best magnetic properties (i.e. highest permeability and lowest core losses) are present in the punched and annealed stator core. It can also be concluded from these data that the process of stress relief annealing has the highest restoring capacity of the magnetic properties in the laser cut core. Depending on the level of peak flux density, the core losses decreased

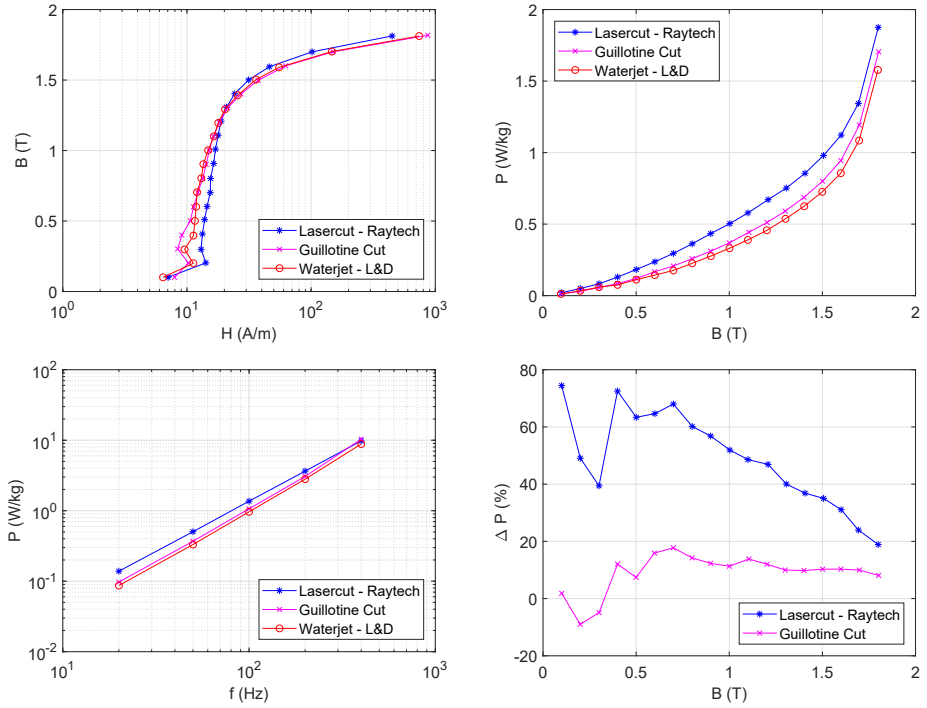


Figure 3.4: M100-23P Epstein strip magnetic measurement data. Top Left: Single Valued BH curves. Top right: Core loss as a function of peak flux density at 50 Hz. Bottom Left: Core loss as a function of frequency at 1 T peak flux density. Bottom right: Difference in core loss as a function of peak flux density obtained at 50 Hz when compared to the waterjet sample.

up to 25 %. For the punched stator cores, the annealing process improved the magnetic properties only slightly.

3.3. Impact of Joining Process on Magnetic Properties

3.3.1 Effect of Interlocking on NO27

In this experiment, the impact of interlocking on a single lamination of NO27 steel is measured. Windings were applied on two laminations, only one of which has undergone an interlocking process. The geometric properties of the lamination are identical to the geometry described in 3.1.1. In Fig. 3.7, the indentation necessary for interlocking laminations is shown. The interlocking process specifications are described in more detail in the next chapter. The measurement data is shown in Fig. 3.8. This experiment shows that interlock-

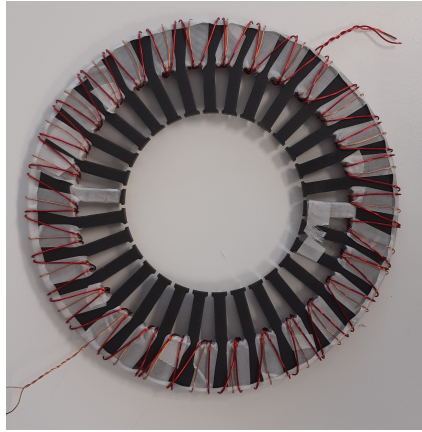


Figure 3.5: M270-35A stator core geometry with applied primary and secondary windings.

ing clearly has a negative impact on the permeability and core losses, although the degradation is rather limited. The degree of degradation is presumably strongly related to the size of the interlocking tool and width of the magnetic path length. The measured core losses increased up to 11 % due to interlocking when the magnetic excitation field frequency is 50 Hz. At peak flux density 1 T, interlocking caused the global average measured permeability to decrease by approximately 50 %.

3.3.2 Effect of Welding on M400-50A

The effects of welding on the yoke magnetic properties are measured on a M400-50A stator core. Two stator stacks are manufactured from the same mother material, one of which was welded with 13 welding seams equidistantly positioned around the yoke. Welding was done with a solid state laser fiber welding technique, more specifically using a Trumpf Trulaser Cell 3000. The laser welding seam and stator core are shown in Fig. 3.9. Each stack was wound with 144 primary and 144 secondary turns. The outer and inner diameter of the stator yoke were 311 mm and 273 mm, respectively. The measurement data is shown in Fig. 3.10. Laser welding the stator stack significantly decreases the magnetic permeability (up to 60 % at 1.1 T) and increases the core losses up to 25 %. Increasing the frequency decreases the additional relative core losses from 41 % at 10 Hz to 24 % at 200 Hz.

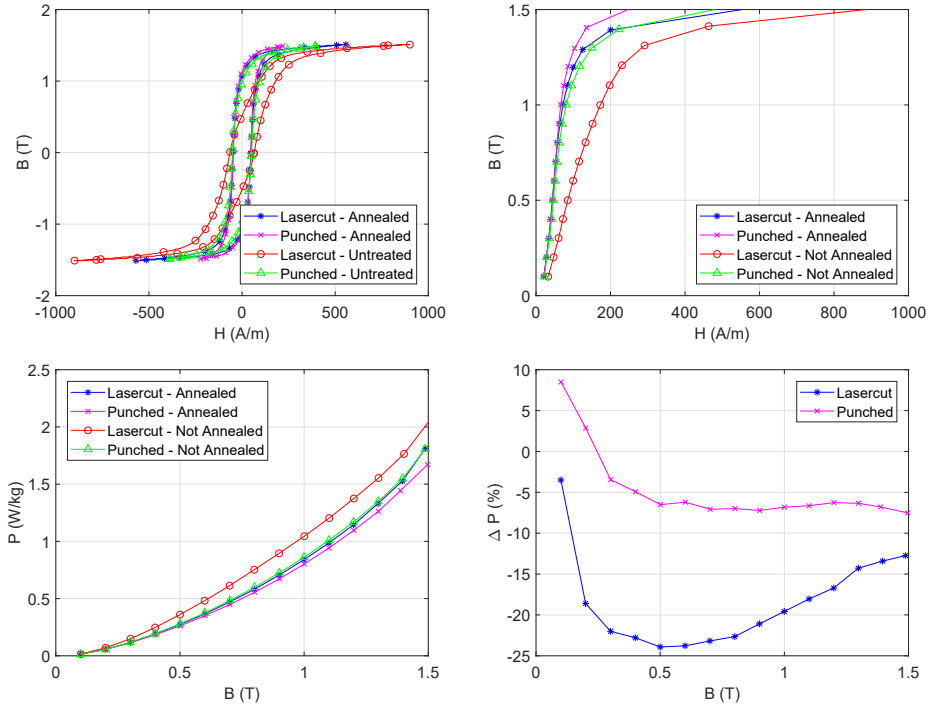


Figure 3.6: M270-35A stator core magnetic measurements. Top Left: Hysteresis loops obtained at 50 Hz. Top right: Single Valued BH curves. Bottom Left: Core loss as a function of peak flux density. Bottom right: Difference in core loss as a function of peak flux density obtained at 50 Hz between the cores before and after stress relief annealing.

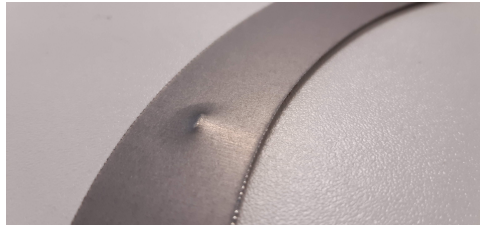


Figure 3.7: Close up picture of interlocked area located centrally on the yoke of a NO27 ring core.

3.4. Conclusion

In this chapter, it was shown how magnetic measurements can be used for obtaining a quantitative estimation of the impact of cutting and joining tech-

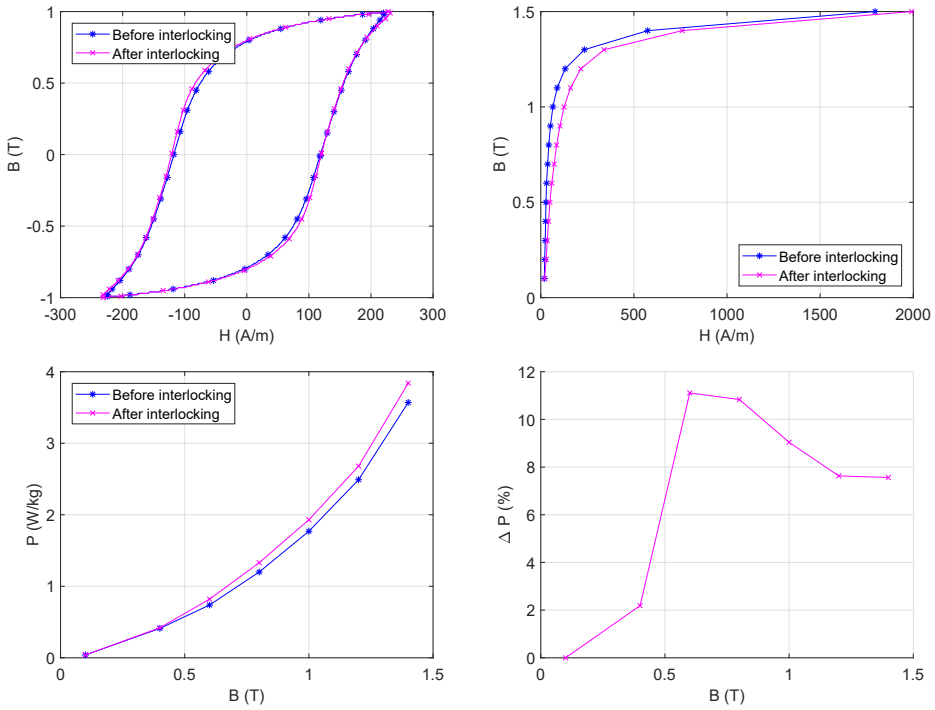


Figure 3.8: NO27 ring core geometry magnetic measurement data. Top Left: Hysteresis loops obtained at 50 Hz. Top right: Single Valued BH curves. Bottom Left: Core loss as a function of peak flux density. Bottom right: Impact of interlocking on the core loss as a function of peak flux density obtained at 50 Hz.



Figure 3.9: Left: Close up picture of laser welding seam. Right: Welded stator core with applied measurement windings.

niques on the magnetic properties of electrical steels. The degrading effects of two different cutting techniques, namely laser cutting and nibble punch-

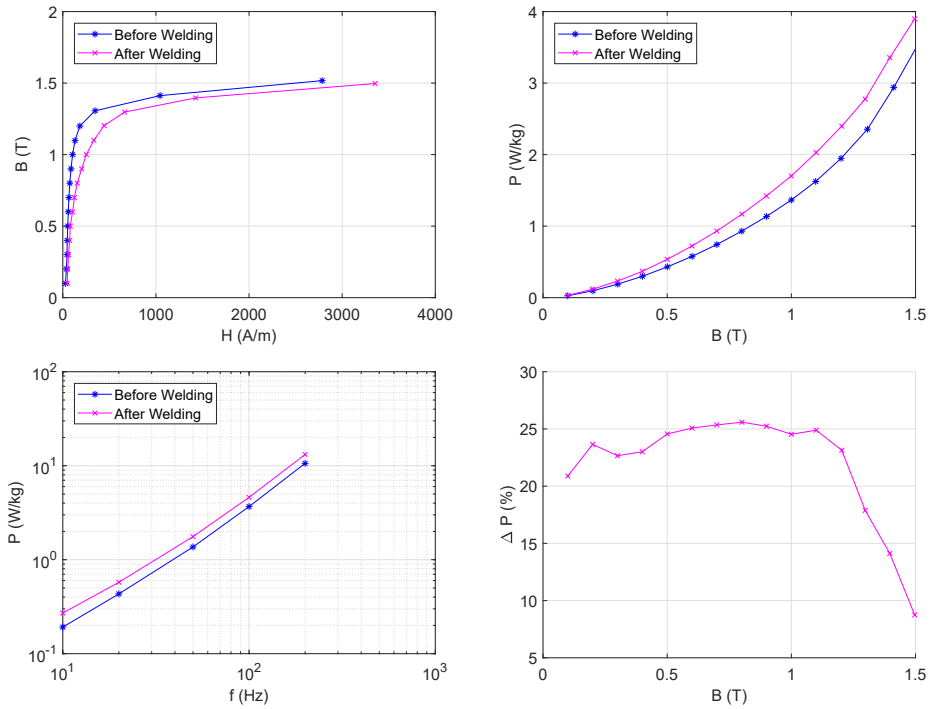


Figure 3.10: M400-50A stator core geometry magnetic measurement data. Top left: Single Valued BH curves. Top right: Core loss as a function of peak flux density. Bottom Left: Core loss as a function of excitation frequency at 1 T peak flux density. Bottom right: Difference in core loss as a function of peak flux density obtained at 50 Hz due to welding.

ing, were compared in terms of average relative permeability and stator core losses. This experiment was done using a NO27 ring core geometry and it was found that the average core losses were approximately 30 and 20 % higher in the laser cut samples than in the nibble punched samples when the peak flux density is 1 T and 1.5 T, respectively. In another experiment, the impact of waterjet cutting, laser cutting and guillotine cutting on M100-23P GO steel was measured using sets of Epstein strips. In this case, the waterjet cut sample had the lowest average core losses, followed by the guillotine cut sample and the lasercut sample. In both experiments, the laser cutting process proved to introduce the most magnetic material degradation. The heat generated on the lamination edge during the laser cutting process introduces large residual stresses which results in a higher average magnetic core loss. The degraded magnetic properties can partly be restored, as was shown in a third experiment using stress relief annealing. In this setup, four M270-35A stator cores were com-

pared, two of which were treated using a stress relief annealing process. After measuring each stator core, it was found that the annealing process reduced the measured core losses at 1.5 T and 50 Hz by 13 % in the lasercut sample and by 7 % in the punched sample. Similarly, the impact of joining techniques can be studied using magnetic measurements. In two experiments - on interlocked NO27 ring core steel and on M400-50A welded stator core steel - the impact of joining was investigated by measuring the core magnetic properties before and after the joining process. In both cases the joining technique decreased the magnetic permeability and increased the average measured core losses. The degree of degradation strongly depends on the process-specific parameters and the electrical steel grade which makes it difficult to define the negative impact using an empirical expression or rule-of-thumb.

4

Modelling of Manufacturing Effects

Accurately modelling the parasitic effects of manufacturing has been in the interest of machine designers and researchers for many years. Gaining a better understanding of these manufacturing effects can lead to improved motor design, efficiency and performance prediction. From the design perspective of electrical machines, this kind of research usually focuses on changes in the macroscopic magnetic properties such as magnetic permeability and specific iron losses. The changes in domain structure and micromagnetic properties are interesting from a scientific point of view, but are not easily translated into useful macroscopic parameters of machine design. Consequently, the link between micromagnetic domain structure and manufacturing effects is often avoided by proposing empirical models that combine existing machine models with manufacturing correction factors (i.e. building factors). In order to improve machine design, a breakdown of these building factors is necessary. Many approaches have been used to tackle this problem. Therefore, an literature review of the most common modelling techniques is provided in this section. Afterwards, these techniques are applied on machine prototypes for the effects of separation and joining.

4.1. Literature review

4.1.1 Effects of Cutting

In the past few decades, the majority of the research on the manufacturing process of electrical machines was focused on the effects of lamination shaping. This was generally assumed as the most degrading part of the complete manufacturing process. The general hypothesis in this field of research is that deterioration near the cutting edge changes the local magnetic properties of the material. Because of its widespread application and preferred use in mass production, punching is the most frequently studied separation technique. Due to limited manufacturing tool availability, steel samples are sometimes manufactured using shear cutting or guillotine cutting as a substitute for industrial punching. As an alternative to punching, laser cutting, EDM and water jetting are also commonly investigated.

With the goal of quantifying the effects of cutting, the geometry for the samples is chosen in such a way that they can be placed in an Epstein frame, a SST, or by measuring ring core geometries. Cutting these samples using EDM typically produced the least amount of magnetic degradation, causing the EDM cut samples to be used as 'degradation free' reference cases against other cutting techniques (such as in [49] and [25]). Water jet cutting also produces very little damage to the magnetic properties of the steel ([65], [62]). However, EDM and water jetting are less of interest to electric machine builders due to their low cutting speed and unsuitability for high volume manufacturing.

In [35], [48], [68], [25], [65], [73] and [13], the degradation due to punching and laser cutting is compared on identical geometries. In Table 4.1, an overview is shown of the reported measurements. The difference in measured core losses between the punched and laser cut samples is listed at three different excitation regimes. In every experiment, the core losses increased more when the samples were laser cut than when they were punched. Measurements of BH curves in these papers all indicate a similar trend: after the separation stage, the global magnetic permeability decreases and the core losses increase. The degree of degradation not only depends on the choice of cutting technique, but also on specific process parameters. In [22], three sets of samples were punched using punching tools with increasing amounts of wear. The measurement results showed that sharp tools produce less magnetic degradation than worn, blunt tools.

It is difficult to accurately predict the degrading effects of separation because of the many factors involved. Lamination thickness, steel grade type, grain size, yield strength, punching process parameters, laser cutter process parameters and sheet geometry all have an impact on the resulting magnetic property degradation.

A systematic approach is necessary for accurately modelling the degradation due to separation. In order to control the degree of degradation, the samples are prepared in sets with varying amounts of longitudinal cuts, as illustrated in Fig. 4.1. This way, the amount of cutting degradation between the sets is controlled. In [21], this control variable was defined as the amount of cut edge length per mass. Between the sets in Fig. 4.1, the cut edge length per mass doubles between set 1 and 2 and triples between set 1 and 3. These sets are typically measured using SST or Epstein frame setups. Once the global magnetic properties are measured, the results are defined as a function of the variable which is presumably related to the degree of degradation. This approach was applied in [80], [26], [20], [8], [13] and [75]. With the magnetic properties defined as a function of the total width and cutting degradation, magnetic material models are built as a function of the width of the test strip and the severity of the cutting degradation.

In most cases found in literature, the modelling challenge revolves around the identification of the degradation depth and a degradation distribution. This degradation depth refers to the distance from the edge and marks a volume which is considered magnetically degraded. Within this volume, a certain degradation distribution is assumed which is either exponential or homogeneous (Fig. 4.2). After obtaining the global magnetic measurements at several induction levels and frequencies, the BH -curve models and core loss models are adapted correspondingly with cutting effect correction factors, such as in [41], [75] and [68]. These models can be fitted accurately and succeed in estimating the global magnetic properties after separation.

Once the modified material models are fitted, they can be applied in FE-models of full machines. Some models are characterized by assigning separate material characteristics to each region of the machine [13], [75], by defining a cutting edge region with degraded but homogeneous properties [8], or by defining several edge layers with increasing levels of degradation towards the outer edge layer, as in [71] and [7]. In the stator tooth regions near the air gap, the cutting effect can be seen as an additional 'extended' air gap due to its worsened magnetic permeability, as was proposed by [56].

However straightforward this modelling challenge may seem, the fitted model parameters not only depend on the assumptions, but also on the specific cutting process parameters. The definition of the degraded zone and its specific degradation distribution are not linked to the actual microstructural state of the edge material. This is why, in several papers, electrical machine researchers have used a multidisciplinary approach and collaborated with metallurgists. By applying techniques for microstructural analysis such as Magneto Optical Kerr Effect (MOKE), Scanning Electron Microscopy (SEM), Electron Backscatter Diffraction (EBSD) and X-Ray Diffraction (XRD), insight is gained into the changes in microstructure near the lamination edge after cut-

ting. On a more macroscopic level, nano-indentation and Vickers hardness tests are performed as a measure to investigate the degree and depth of plastic deformation near the edge. [80] used EBSD data on punched laminations to calculate local dislocation densities and found a 500 % increase when approaching the cut edge. The increase was noticeable in the area up to 0.5 mm from the cut edge. [49] correlated a 20 % core loss increase after punching to MOKE measurements indicating an impeded domain wall displacement near the edge. Residual stress was measured using nano indentation by [15], and an increased residual compressive stress of approximately 350 MPa was found up to 0.5 mm from the edges of punched laminations. [60] observed the grain structure near cut edges with SEM and could identify a degradation depth between 0.15 and 0.2 mm, depending on the grade. The silicon content of the steel also appears to have an impact on the degree of degradation due to cutting. [12] studied the effect of cutting on two grades with a different thickness and concluded that steel grades with thinner lamination gauge and lower silicon content seem to degrade less.

Stress relief annealing is a popular technique for restoring the magnetic properties of laminations after separation. The effects of annealing have been investigated by comparing measured magnetic properties on samples before and after annealing in [15], [21] and [37]. In [16], two identical switched reluctance motors (SRM) were manufactured, but only one of them was manufactured with laminations that were annealed after assembly of the stack. The annealing process resulted in a 25 % higher torque at nominal speed and an increase in machine efficiency at higher torque loads.

From literature, the following can be concluded regarding the effects of separation on the magnetic properties in electrical steel;

1. The cutting effects on the edge are related to stress induced near the cut edge. This stress changes the local magnetic domain structure.
2. The grain size diameter and orientation are altered, the material experienced plastic stress which has led to permanent material strain.
3. The resulting effects on the global magnetic properties are strongly related to three main qualities, namely 1) the lamination geometry, 2) the cutting technique applied and 3) the initial properties of the electrical steel grade.
4. This results in local magnetic degradation, which tends to push the magnetic flux towards the center of the lamination. Consequently, the material in the center of the lamination saturates before the material near the edges.
5. With decreasing total sheet width, the portion of the degradation depth becomes larger and the overall degrading effect of cutting becomes more significant. Therefore, the effects of cutting are more critical in the teeth of stator or rotor laminations than in the yoke.
6. For mechanical cutting, the degradation is caused by residual mechanical stresses in the crystal lattice due to the forceful disruption of the punch. For

Table 4.1: The increase in measured core losses at three excitation regimes between laser cut and punched lamination geometries in reported experimental results. For each case, the laser cut sample had a higher core loss than the punched sample.

	<i>Geometry</i>	<i>Grade</i>	<i>400 Hz 1 T</i>	<i>50 Hz 1 T</i>	<i>50 Hz 1.5 T</i>
[35]	Epstein strips	n.a.	10 %	n.a.	n.a.
[48]	Ring cores	0.35 mm, 2.8% Si	23 %	21 %	15 %
[68]	SST, cut in 4 mm strips	0.3 mm, 2.4% Si	n.a.	35 %	5 %
[25]	SST, cut in 6 mm strips	M330-35A	17 %	25 %	10 %
[65]	Epstein strips	35W270	6 %	17 %	3 %
[73]	Ring cores	n.a.	29 %	n.a.	n.a.
[13]	Epstein strips, cut in 10 mm strips	M400-50A	n.a.	20 %	10 %

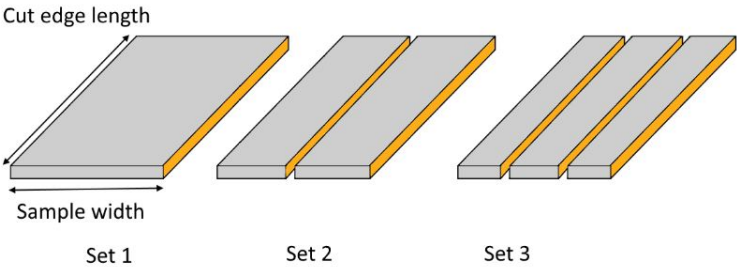


Figure 4.1: Sample preparation for investigating the effect of cutting.

- laser cutting, the heat generated by the focused laser beam causes thermal residual stress near the cut edge.
7. Stress relief annealing can partly restore the magnetic properties after cutting.

4.1.2 Effects of joining

The most prominent industrial techniques for joining laminations are welding, interlocking or adhesive varnish baking. Correspondingly these are the techniques most studied in literature. The effect of joining is typically investigated by comparing magnetic measurements on identical stacks of geometries before and after joining. In [5], as a general design guideline, it is mentioned that the total core losses increase by about 1 % for each welding point. How-

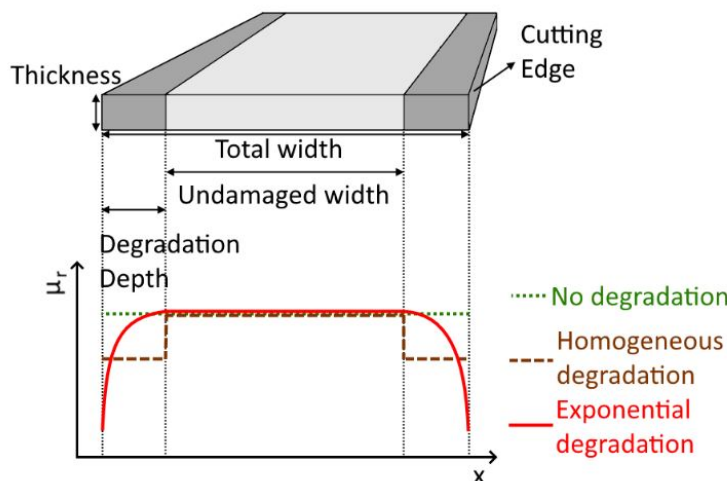


Figure 4.2: Definition of degradation depth and common degradation distributions.

Table 4.2: The added core losses after the joining operation on experimental stacks of electrical steel found in literature.

	Geometry	Grade	Number of welds or interlocks	Added core loss at 50 Hz, $B_p = 1\text{ T}$
[5]	Stator core	M680-50A	12 weld points	6 %
[36]	Ring core	n.a.	8 weld points	$\pm 20\%$
[63]	Ring core	n.a.	4 weld points	20 %
[27]	Ring core	M400-50A	8 interlocks	33 %
[77]	Ring core	B27ahv1500	6 weld points	24 %
[13]	Epstein strips	M400-50A	10 weld points	50 %

ever, it appears that this is too rough a generalization which is not valid for every joined stack. In Table 4.2, an overview is given of the effect of joining on the core losses for several geometries and grades found in literature. These papers report on the increase in core losses after joining by measuring the global magnetic properties of prototype setups. Prior to joining the laminations, the stack is usually slightly compressed in the axial direction. For interlocking, this is done to ensure a strong form fitting of the subsequent indentations. For welding, stack compression leads to a close contact between the adjacent laminations. When small air gaps exist between the laminations, this might lead to incomplete formation of the weld seam.

Similar to separation techniques, the effects of joining are complex and depend on the considered geometry, the steel grade, the specific process param-

eters and the location and amount of joining points. In [17], the magnetic core losses on a large number of manufactured stators was studied and the variability in magnetic properties was measured. The goal of this study was to relate variations in measured core losses to variability in build quality. It was concluded that in this specific manufacturing process, on average, the core losses increased by 5 % due to the welding process. More interestingly, it was found that the magnetic degradation due to welding on two identical batches which were measured on the same day, depended on the person who welded the stator stack. It appeared that the specific welding technique varies between welders and this variation has an impact on the resulting magnetic degradation. In other papers, the influence of several welding process parameters on the magnetic properties and local microstructure was examined. [78] studied the effect of welding speed on the magnetic properties and found that lower welding speed results in higher additional iron losses, noting that the range of the appropriate welding speeds is constrained by the torsion strength and the magnetic property requirements of the stack. In [61] it was demonstrated that pores are formed due to laser welding when gaseous decomposition products of the coating are entrapped by the solidification of the molten pool. Further, it was also shown that with increasing welding speed this undesirable pore formation increases. [63] mentioned that residual stresses from welding heat can influence substantially the magnetizing behaviour of NO electrical steel. In both [33] and [76], the residual stress near welding seams in electrical steel was measured and it was found that tensile stress appears within the weld seam while compressive stress appears in the heat affected region near the weld seam. In Fig. 4.3, the residual stress distribution near welding seams in steel plates is shown. These data are measured using the Magnetic Barkhausen Noise technique. In both papers, this measured distribution was also found using X-Ray Diffraction. Additionally, [36] noted that the welding process destroys the thin insulation layer between the lamination sheets, introducing local short circuit paths, resulting in increased eddy current losses.

Efforts to formulate welding models were done either numerically or analytically. In [77], an analytical model is presented that shows the exponential increase of classical losses when the weld bead radius increases. In [36], a 2D FE model that incorporates welding effects was used to simulate the influence of welding on a slotless permanent magnet machine prototype.

As an alternative to welding, interlocking creates residual mechanical stress due to local plastic deformation which degrades the magnetization properties of the steel. It can also abrade the insulation coating, potentially creating short circuits between laminations which enable local eddy current circuits. In combination with edge burr contacts due to cutting, these circuits can facilitate large induced interlaminar eddy currents (ILEC) that further increase the core losses. [37] studied additional core losses of interlocking on samples that have

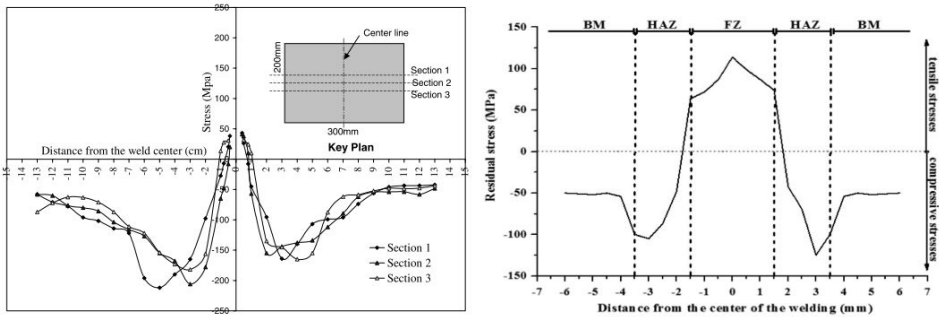


Figure 4.3: Two independent literature results showing the residual stress distribution near welding seams in steel plates. Both results were obtained using the Magnetic Barkhausen Noise Technique. Left: Local residual stress near the welding seam (center line) on three different sections [76]. Right: Local residual stress near welding seam where the areas are divided into the Fusion Zone (welded zone), the Heat Affected Zone and the Base Metal [33].

been subjected to stress relief annealing, isolating the effect of ILEC. In this work, it was reported that interlaminar eddy currents due to interlock short circuits and electrical contact between burr edges can increase the core losses up to 20 %. When considering interlocking, the type of coating used plays an important role. [47] studied samples with different coating thickness and observed that the thickness of the coating, which consisted of a mixture of organic and inorganic insulation, affects the interlocking fastening strength, and that sheets with a thin coating are more favourable in terms of interlocking performance than sheets with a thick coating due to the lubricating effect of the resin in the coating. [27] shows experimentally that the influence of ILEC is negligible in the increase of iron losses, but note that this conclusion depends on the type of coating material used for the laminations.

Various attempts have been done to model the effects of interlocking. In [38], the impact is studied of various stacking processes and their effects, including the effect of ILEC caused by interlocking, with FEM analysis and equivalent electric circuit models. It was found that the additional eddy current losses increase linearly with the amount of electrically connected laminations in the stack. [64] applied the 2D FEM technique to simulate the different effects of interlocking on the different loss components.

As an alternative to welding and interlocking, manufacturers can stick the laminations together using an adhesive glue coating. The magnetic effects of glueing were compared to welding in [63] and it was concluded that glueing, from a magnetic point of view, was much more favourable than welding. The core losses appeared to be only marginally increased.

The impact of lamination joining on the magnetic properties of the stack are case specific. It is difficult to generalize the degree of degradation quantitatively. However, the results from literature can be summarized qualitatively as follows:

1. Lamination joining degrades the magnetic properties of electrical steel stacks. The degree of degradation depends on lamination geometry, joining technique process parameters and the electrical steel grade.
2. The interlocking process introduces residual mechanical stress in the material due to plastic deformation.
3. The type of coating used to insulate the laminations influences both the fastening strength and the degradation effect of interlocking.
4. When applying interlocking, an effort should be made to choose the appropriate coating which enables a sufficient joining strength and simultaneously avoids the creation of interlaminar electrical contact points.
5. Welding introduces residual thermal stress in the area around the welding seam, which is known to change the local magnetic properties. This residual stress is typically tensile in the weld seam and compressive in the heat affected zone directly adjacent the weld seam.
6. Welding creates an interlaminar short circuit over the entire stack length. Consequently, local eddy current circuits are formed in the welding seam.
7. Glueing as a joining technique has proven to cause the least amount of degradation. However, additional manufacturing steps are needed after applying the glue and the type of adhesive coating is crucial in order to create sufficient joining strength.

4.2. Separation effects in M100-23P GO steel

In this section, the effects of several cutting techniques are described on the magnetic properties of GO electrical steel. Compared to the effect of cutting on NO steels, the literature on the relation between cutting degradation and magnetic properties of GO steels is relatively scarce. The material under investigation is M100-23P, a grain oriented steel with a thickness of 0.23 mm and a mass density of 7.65 kg/dm³. The approach frequently found in literature for NO steel is utilized. Standard Epstein strips are cut into several thinner strips in order to control the degree of cutting degradation between the sets. The sets of strips are separated from the same mother coil using guillotine cutting, laser cutting (1.5kW CO₂ laser) and water jet cutting. Magnetic measurements results are used to identify the parameters of a cutting degradation material model. This model is afterwards applied to a MEC model of a Yokeless and Segmented Armature (YASA) motor (Fig. 4.4) with the purpose of comparing the effect of different cutting techniques on the efficiency of this specific machine.

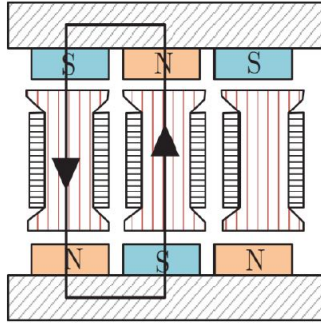


Figure 4.4: Yokeless and segmented armature (YASA) double rotor axial flux machine [70].

4.2.1 Experimental setup and methodology

The test samples are manufactured starting from standard Epstein strips. These samples are cut into several thinner slices parallel to the GO direction with widths given in Table 4.3, and named sample A, B, C, D. Then, the strips are recombined so that the total width of the material placed in the Epstein frame is 30 mm (Fig. 4.5). The single valued BH curve for each set is constructed and the core losses are measured at 20, 50, 100, 200 and 400 Hz. Based on these measurements, analytical functions are fitted for defining the local magnetic permeability and core loss density as a function of the distance to the closest edge. An exponential degradation model is assumed with increasing core losses and decreasing permeability towards the edge. The specific coefficients are fitting parameters. The relative permeability in this model is defined as

$$\mu(H, x) = \mu_n(H) - \Delta\mu(H)e^{-a(H)x} \quad (4.1)$$

where x is the distance to the closest cutting edge and μ_n represents the permeability of the undamaged region. The undamaged material properties are derived from the measurements on the least degraded sample in the set which is water jetted set D. Fitting parameter a is a function of the global average magnetic field strength. The core loss model which accounts for cutting effects is based on the separation of losses principle. In this model, the hysteresis and excess loss component increase locally in the degraded zone due to residual cutting stress. Hence, both components depend on the distance to the cut edge and the local magnetic flux density $B(H, x)$. The material resistivity is assumed to be unaffected by this stress. Therefore, the classical loss component remains independent from x . This assumption is widely accepted in literature and will be verified experimentally in the next chapter.

Table 4.3: Details of each sample set used in the separation experiment.

Sample Name	Single strip width (mm)	Number of strips per coil	Total sample width (mm)
A	5	6	30
B	10	3	30
C	15	2	30
D	30	1	30

$$P(B, x) = C_{hyst}(B, x)B^{\alpha(B)}f + C_{cl}(B)B^2f^2 + C_{exc}(B, x)B^{3/2}f^{3/2} \quad (4.2)$$

$$C_{hyst}(B, x) = C_{hyst,0} + \Delta C_{hyst}(B)e^{-b(B)x} \quad (4.3)$$

$$C_{exc}(B, x) = C_{exc,0} + \Delta C_{exc}(B)e^{-c(B)x} \quad (4.4)$$

The parameters α , C_{cl} , $C_{hyst,0}$ and $C_{exc,0}$ are considered independent of the distance to the cutting edge. The material properties as defined by (4.1) and (4.2) are assigned to the non linear reluctances in the sliced MEC model of a YASA machine (Fig. 4.6). Each node in the model is characterized by its distance to the nearest edge. For example, in Fig. 4.6 at node $n_{x=3,y=1}$ and node $n_{x=4,y=1}$, the x -values in equations (4.1), (4.2), (4.3), and (4.4) equal the distances D_1 and D_2 respectively. In order to improve the local accuracy of the model, the nodes can be further discretized. In the tangential direction, n_{x1} , n_{x2} and n_{x3} are discretized into 8 elements, n_{x4} into 10. In the radial direction, n_{y1} , n_{y2} and n_{y5} are discretized into 3 elements, while n_{y3} , n_{y4} and n_{y6} are divided in 2. This model is explained in further detail in [23]. It should be noted that in this proposed model, the skin effect is not considered. The classical loss equation without considering the skin effect is only valid when the strip width is at least 20 times larger than the sheet thickness. Thus, neglecting the skin effect might lead to inaccurate predictions of the classical loss component when the strip width becomes too small. However, in this experiment, the smallest strip width was 5 mm, which was more than 20 times larger than the sheet thickness of 0.23 mm.

4.2.2 Measurement results

The measured BH curves and core losses for each set are shown for guillotine cutting, laser cutting and water jetting in Fig. 4.7, Fig. 4.8 and Fig. 4.9. Regardless of the separation technique it is clear that with increasing cut edge length per mass, the magnetic properties degrade. A decrease in the magnetic

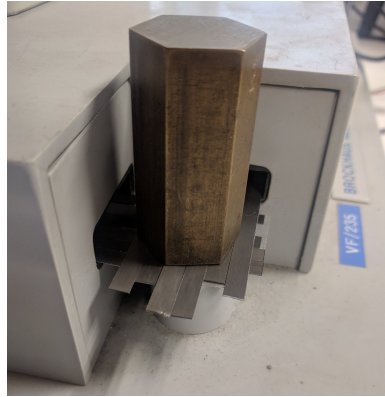


Figure 4.5: Sample set A placed in the Epstein frame.

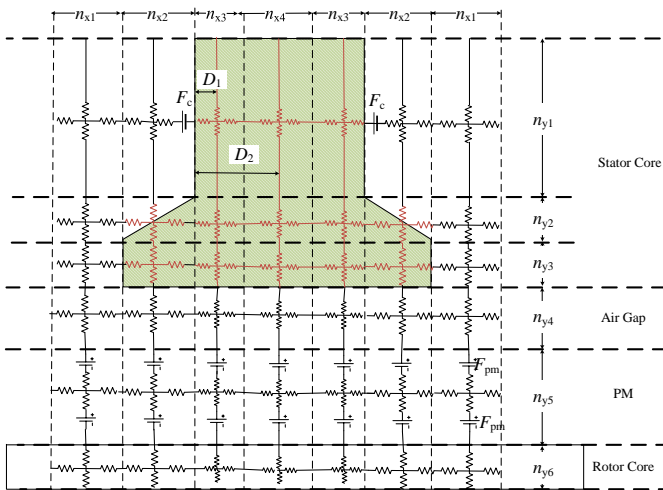


Figure 4.6: A radial slice of the stator tooth in a YASA machine with corresponding MEC model [70].

permeability and increase in core losses is measured. This trend in the core losses is maintained at higher excitation frequencies. When comparing the BH curves for each cutting technique, the difference in the degree of degradation becomes clear (Fig. 4.10). It appears that, from a magnetic point of view, water jet cutting introduces the least degradation to the material. Laser cutting causes significantly more damage than both water jetting and guillotine punching. On the widest strip (set D), the core losses after water jet cutting at 1.5 T and 50 Hz are approximately 14 % and 60 % lower when compared to punching and laser cutting, respectively. A similar trend is noticed when

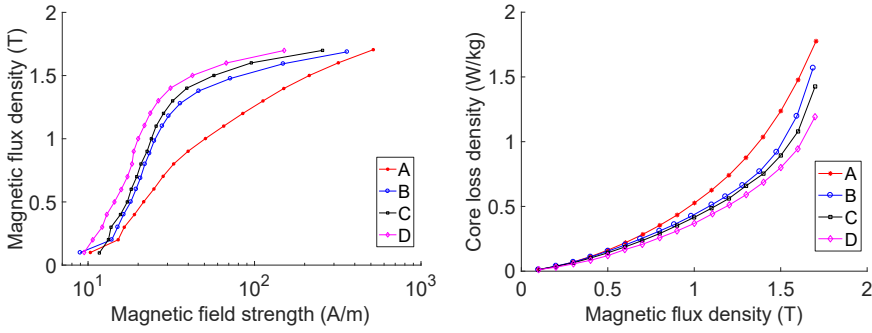


Figure 4.7: Measured BH curve and core losses at 50 Hz on sets of M100-23P guillotine cut Epstein strips.

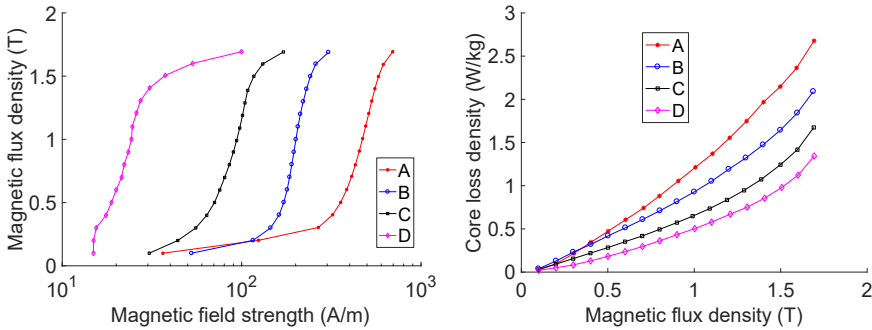


Figure 4.8: Measured BH curve and core losses at 50 Hz on sets of M100-23P laser cut Epstein strips.

comparing the core losses in Fig. 4.11 and Fig. 4.12. The water jetted sample *D* proved to be the least degraded after cutting. The measurement data corresponding to this sample will be used as the non degraded reference for identifying the model parameters unrelated to degradation, namely α , C_{cl} , $C_{hyst,0}$ and $C_{exc,0}$.

4.2.3 Simulation results

The material model which accounts for the separation effects can be fitted based on the global measurements. Sets A, B, C and D are assumed to have uniform magnetic properties related to their distance to the cut edge according to Table 4.4. Using the non degraded material parameters and the mea-

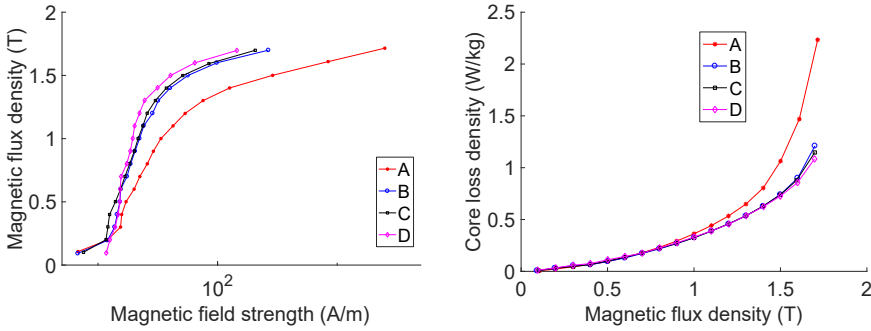


Figure 4.9: Measured BH curve and core losses at 50 Hz on sets of M100-23P water jetted Epstein strips.

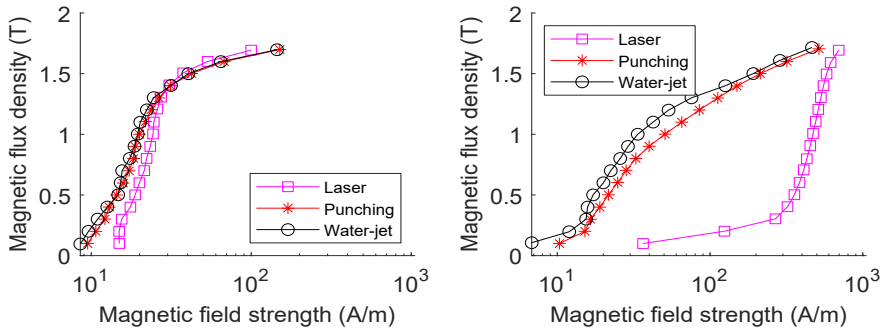


Figure 4.10: Comparison of measured BH curves for three different separation techniques on set D (left) and set A (right).

surement data for the sets of thinner strips, the cutting model can be fitted. The fitted model enables extrapolation of local magnetic material properties at any distance x from the cut edge. In Figs. 4.13, 4.14 and 4.15 the local properties are shown for different distances to the cut edge in the case of laser cutting, punching and water jetting respectively. In the fitted model simulations, the superiority of water jetting over laser cutting and punching is expressed.

4.2.4 YASA machine simulations

The MEC model is simulated with the cut edge material model on a 4kW YASA motor. Detailed machine parameters are summarized in Table. 4.5. The main machine characteristics can be simulated for different cutting techniques

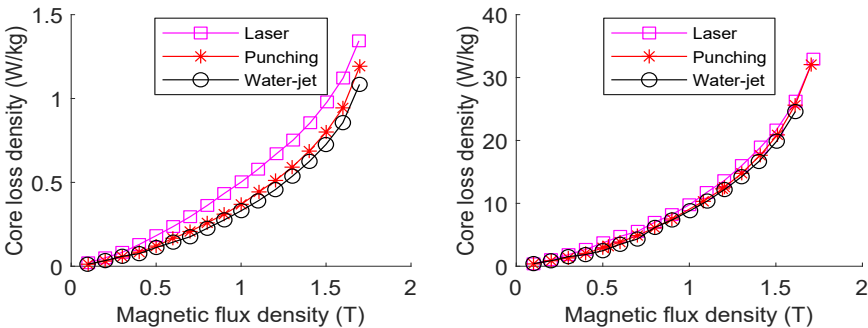


Figure 4.11: Comparison of measured core losses for three different separation techniques on set *D* at 50 Hz (left) and 400 Hz (right).

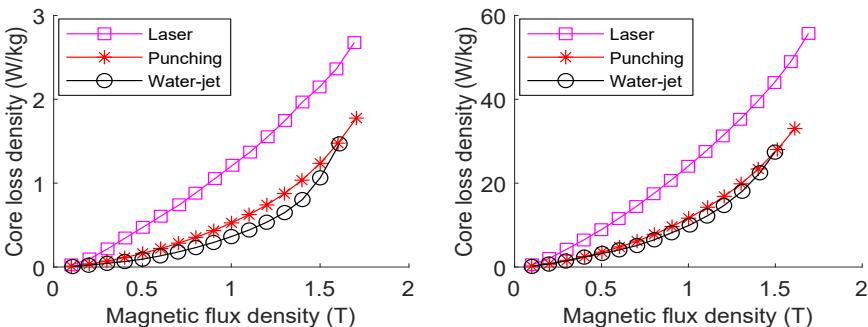


Figure 4.12: Comparison of measured core losses for three different separation techniques on set *A* at 50 Hz (left) and 400 Hz (right).

Table 4.4: Assumed distance to the cutting edge of the measured samples.

Sample Name	Assumed distance to nearest cutting edge (mm)
A	2.5
B	5
C	7.5
D	15

by calculating the sliced MEC model parameters at different time-stepped current excitation regimes and afterwards post processing the solution to obtain average values for the entire machine. In these simulations, 6 slices were considered and each excitation period was divided into 50 time steps. The non de-

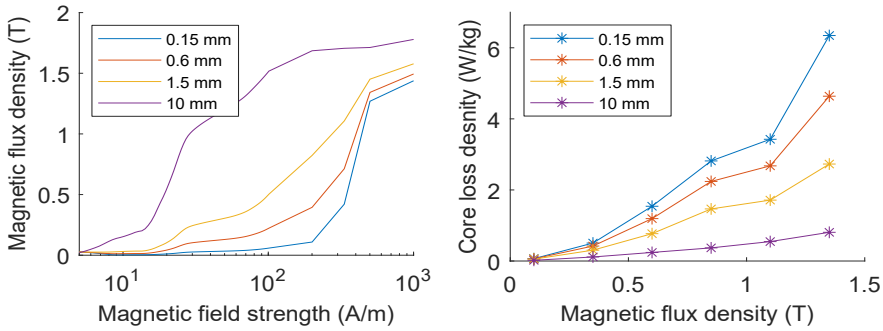


Figure 4.13: Simulated local BH curves (left) and 50 Hz core loss curves (right) for laser cut steel at different distances to the nearest edge.

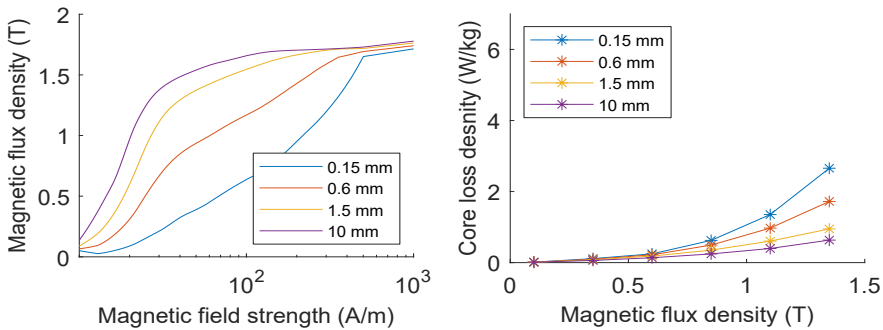


Figure 4.14: Simulated local BH curves (left) and 50 Hz core loss curves (right) for punched steel at different distances to the nearest edge.

graded material properties are derived from the least damaged sample (water jetted sample *D*). In Figs. 4.16, 4.17 and 4.18, the calculated average electromotive force (EMF), total core losses and torque are plotted for various current angles. The effect of cutting degradation on the total core losses in the machine correlates with the measured losses on Epstein strips. A 120% to 180% increase in core loss due to laser cutting is found. The additional core losses due to punching (40% to 50%) and water jetting ($\pm 6\%$) are significantly lower. These additional losses are calculated against the reference case with no cutting effect (i.e. all material properties are derived from the waterjet cut sample *D*). EMF and machine torque are only slightly influenced by cutting degradation. In [50], a comparison on the effect of cutting techniques on GO steels

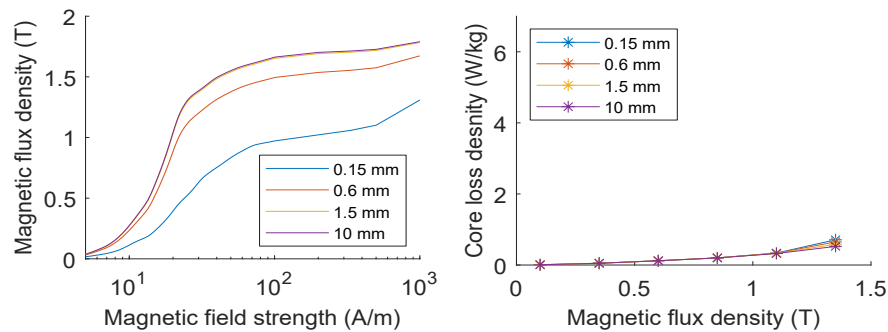


Figure 4.15: Simulated local BH curves (left) and 50 Hz core loss curves (right) for water jetted steel at different distances to the nearest edge.

Table 4.5: Specifications of YASA test machine

Parameter	Value
Rated Power	4kW
Number of stator slots	15
Number of pole pairs	8
Stator outer diameter	150 mm
Stator inner diameter	100 mm
Connection	Star

shows a similar result, indicating that the core losses in laser cut samples is approximately 2 times higher than in the punched samples.

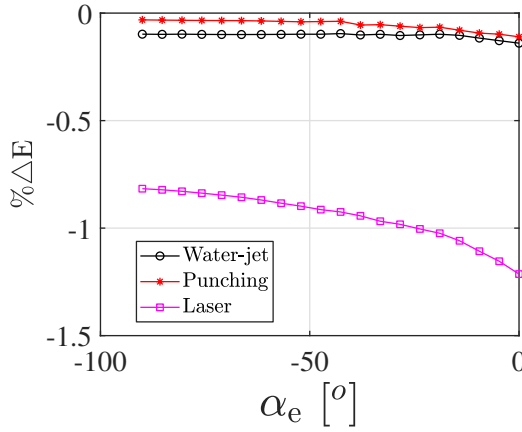


Figure 4.16: Decrease in electromotive force (EMF) at different current angles for all three cutting techniques. The EMF decrease is relative to the motor model without cutting degradation.

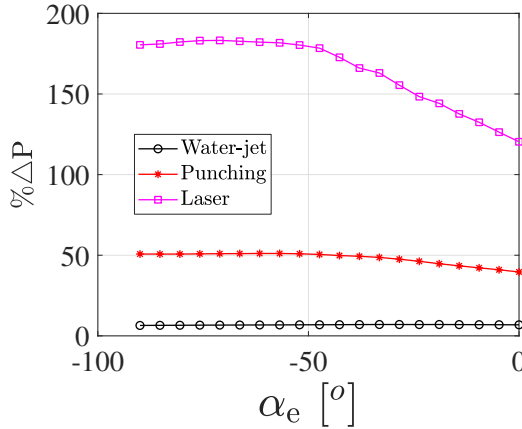


Figure 4.17: Increase in core losses at different current angles for all three cutting techniques. The loss increase is relative to the motor model without cutting degradation.

4.3. Welding effects in M400-50A stator laminations

In the literature review (4.1.2), the most prominent effects of welding on the properties of electrical steel stacks were mentioned. Thermal stress locally changes the magnetization behaviour in the area of the welding seam, and an electrical connection is formed which counteracts the benefits of building a ferromagnetic core. In this section, experimental global measurements on laser welded stator cores are analysed and a general methodology for mod-

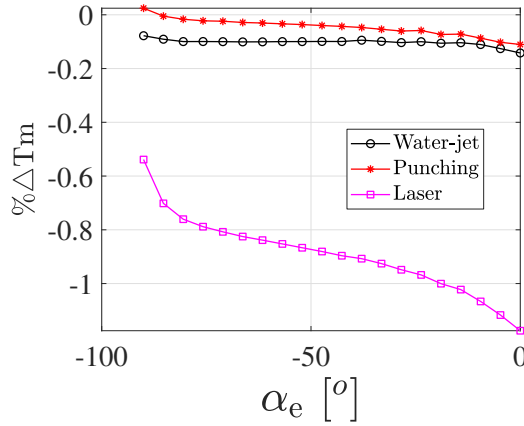


Figure 4.18: Decrease in torque at different current angles for all three cutting techniques. The torque difference is relative to the motor model without cutting degradation.

elling these effects in full FE motor models is described. As an attempt to validate this methodology, measurements are performed on a 4-pole 37 kW induction motor with 48 stator slots. The stator laminations were joined using laser welding (Fig. 4.19). The test motor was fitted with a blocked rotor stack so that the loss measurements did not include any friction losses. Also, the stator was not shrink fitted in a housing frame hence the corresponding losses due to compressive stresses were not included in the measurements and simulations. This way, only the effect of stator welding was discriminated in the analysis.

4.3.1 Experimental setup and methodology

The impact of welding is investigated by quantitatively comparing the core loss measurements on two stacks of NO M400-50A stator laminations. With the goal of minimizing the interference of welding and cutting effects, the stator laminations were manufactured using EDM. Undamaged material properties are derived from the first stack, which consists of 10 loose sheets. The 'damaged' welded material properties are derived from the second stack, which consists of 10 sheets laser welded together on 13 equidistant locations around the stator outer edge (Fig. 4.19). The laser welding was done using a Trumpf Trulaser Cell 3000 solid state fiber laser. Two concentric coils were wound around the yoke of the stator stacks and the double-coil field metric method was used for obtaining global magnetic measurements. The loss model utilized here is adapted from (2.14) with parameter α set equal to 2. This approximation is commonly found in literature and is only valid for relatively

low values of B , when the material is not extremely saturated. The simplified model has three loss coefficients C_{hyst} , C_{cl} and C_{exc} and serves to characterize the core losses for the welded and unwelded stack

$$P_{tot} = C_{hyst} B_p^2 f + C_{cl} B_p^2 f^2 + C_{exc} B_p^{1.5} f^{1.5} \quad (4.5)$$

Although the steel grade is identical, the global material properties for the welded stack and unwelded stack are modelled with different BH curves and loss coefficients. Effectively two separate materials are considered. In the FE model, each material is assigned to a specific part of the machine geometry. This methodology is a coarse generalisation because it disregards the local degradation effects near welding seams. However, there is value in verifying the accuracy of this approach because it requires only few measurement data which are then fitted to a simple loss model.

A time-stepping 2D FE analysis of the 37 kW induction machine is performed. One symmetric pole is considered and the mesh consists of 1516 second-order elements with 3085 nodes. The model is elaborated further in [69]. This simulation was executed twice. The first time, the unwelded material parameters were assigned to the yoke and teeth regions. The second time, the welded material parameters were assigned to the yoke region (Fig. 4.20) while the tooth region was modelled using the unwelded material parameters.

4.3.2 Measurement results

With the purpose of identifying the loss coefficients in (4.5), the measured core losses are obtained at several excitation frequencies under sinusoidal flux density waveform with increasing peak flux density (Fig. 4.21). An increase in core losses due to welding is consistently noticed in the range of measured frequencies. The core loss coefficients are obtained using least square curve fitting and the results are summarized in Table 4.6. The results shown in this table are found using a fitting procedure and seem to indicate that welding of the stator primarily impacts the excess loss component. However, it is not recommended to interpret these fitting results as physically accurate due to the error that might be introduced through the fitting procedure. From a practical point of view, the resulting fitting coefficients can be used further in FE simulations and will yield accurate results when modelling the total core losses.

The effect of welding degradation is also remarkable in the BH curves (Fig. 4.22). Welding clearly decreases the global magnetic permeability in the stator yoke.

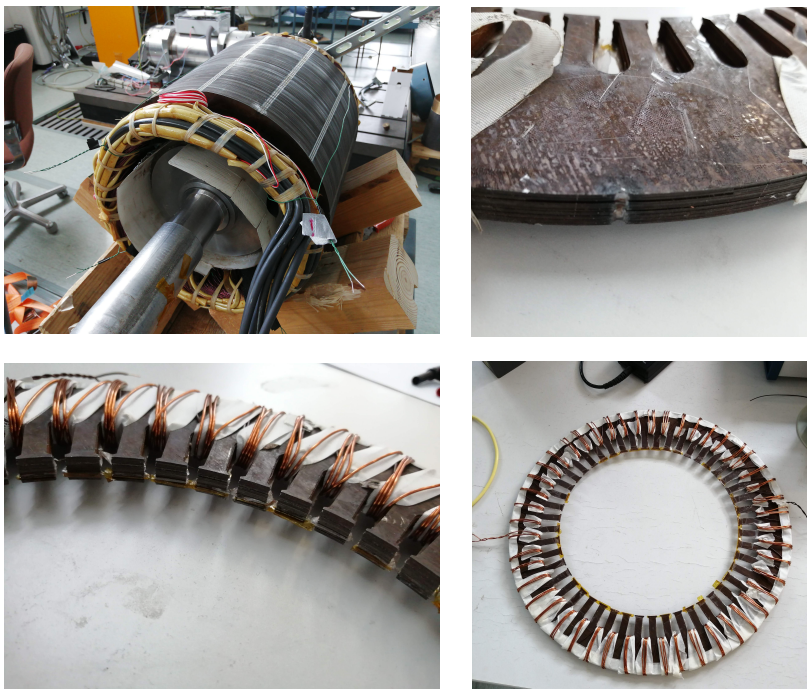


Figure 4.19: Pictures of setups for welding experiment: 37 kW induction machine with blocked rotor (top left), close-up of laser welding seam on sample stack (top right), stator stacks with double winding (bottom).

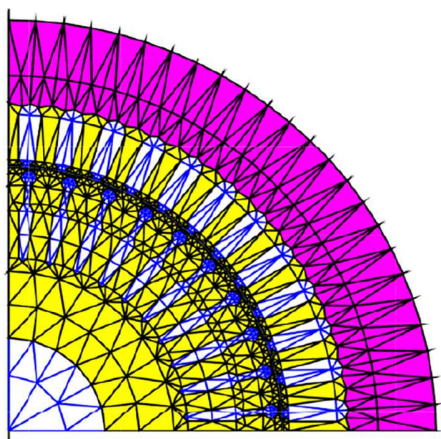


Figure 4.20: FE model mesh of an induction machine with laser welded stator. The stator has different material properties for the yoke and the teeth.

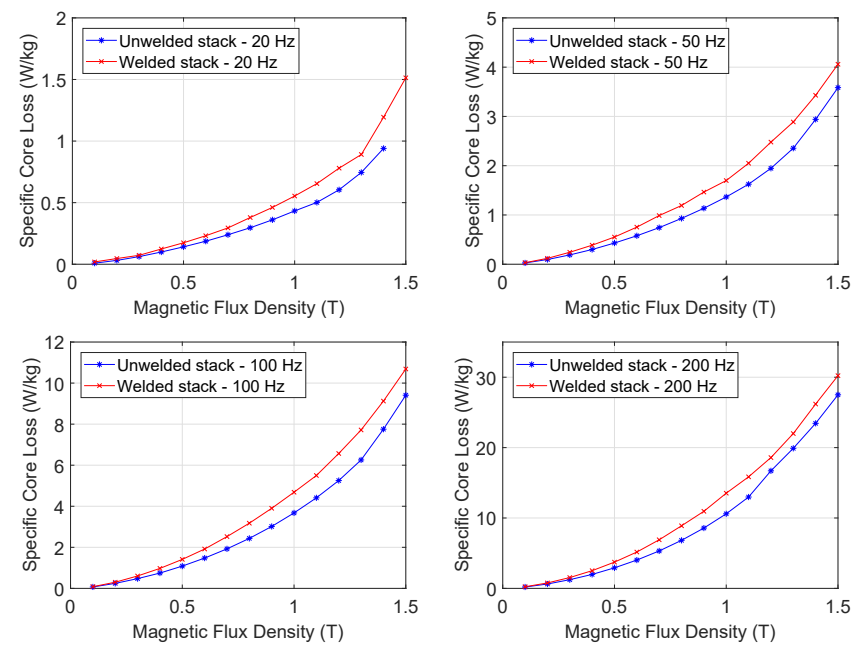


Figure 4.21: Measured core losses at 20, 50, 100 and 200 Hz excitation frequency for the welded and unwelded stator stack.

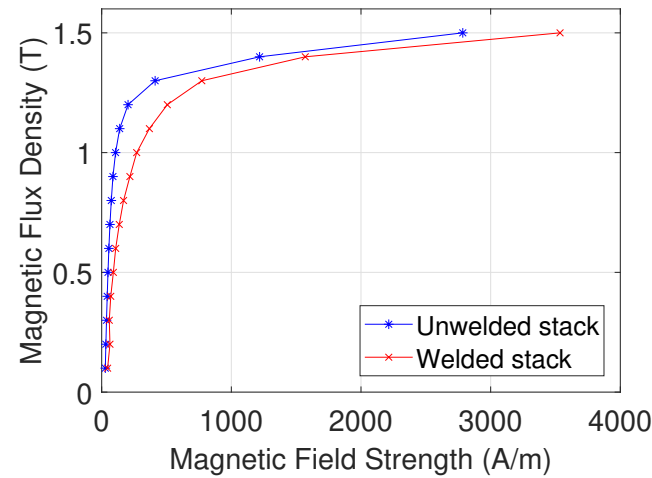


Figure 4.22: Single valued BH curves for welded and unwelded stack.

Table 4.6: Core Loss Coefficients of Welded Stator Core

	Unwelded	Welded	% Difference
C_{hyst}	0.020	0.021	5
C_{cl}	$1.5e^{-4}$	$1.8e^{-4}$	20
C_{exc}	$2.7e^{-4}$	$8.0e^{-4}$	196

4.3.3 FEM simulation results

A time-stepping FE analysis of a 37 kW cage induction motor is performed at two different load conditions, i.e. no load and full load. The effect of welding on the yoke material is considered in terms of BH curves and core loss coefficients, which were obtained from the welded stator core measurements. The effect of welding on motor performance parameters such as supply current I_s , stator core losses P_{cs} , total core losses P_{tot} and torque T is analysed. The results of this FE simulation are summarized in table 4.7 for the no load condition and table 4.8 for the full load condition. The no load current increased about 4 % due to decreased permeability of the welded stator core. At full load condition, this increase is much less significant (0.8 %). However, an increase in the range of about 10 % has been observed in the stator core loss for both load conditions.

Table 4.7: Welding effect on induction motor at no load condition

	Unwelded	Welded	% Difference
I_s (A)	32.0	33.4	4
P_{tot} (W)	332	359	8
P_{cs} (W)	256	285	10

Table 4.8: Welding effect on induction motor at full load condition

	Unwelded	Welded	% Difference
I_s (A)	67.45	68.00	0.8
T (Nm)	230.1	230.2	0.04
P_{tot} (W)	390	421	8
P_{cs} (W)	297	328	10

4.3.4 Full motor measurement results

The simulation results have indicated that welding impacts mainly the core losses, and to a lesser degree the other motor performance parameters such

as torque or full load current. Therefore, this paragraph focuses on reliable and accurate measurements of the stator core losses of a blocked rotor setup, shown in the top left of Fig. 4.19. A Fluke Norma 4000 power analyser was used for measuring supply voltage, current, frequency and power which was provided using a controlled transformer. With a blocked rotor (and no squirrel cage), the total measured power consists of copper losses and core losses. The total core losses are calculated by subtracting the copper losses from the total losses. Finally, the stator core losses are obtained by subtracting the simulated rotor core losses from the total core losses. There is a clear increase of approximately 10 % in the simulated stator core losses as a result of the welding effect (Fig. 4.23). In Fig. 4.24, a comparison is made between the simulated and the measured stator core losses. From this comparison, it becomes clear that the used approach yields only moderately accurate results. At rated supply voltage (400 V) and overrated supply voltage (450 V), the error between the simulated and measured stator core losses in the welded stator is relatively high. This might be due to the limited range of stator core measurements (up to 1.5 T) when the machine flux density can locally increase up to 1.8 T, especially in the stator teeth. This local saturation becomes apparent in the FE-simulation result of the flux density distribution, shown in Fig. 4.25.

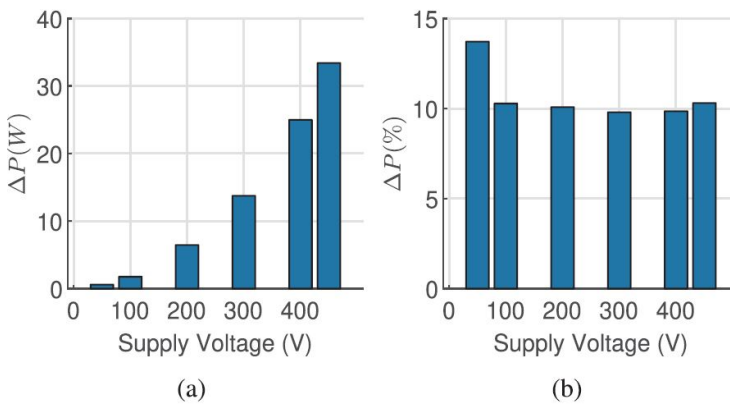


Figure 4.23: Increase in simulated stator core losses of blocked rotor setup due to the welding effect at 50 Hz and different supply voltages, both in absolute values (a) and relative values (b).

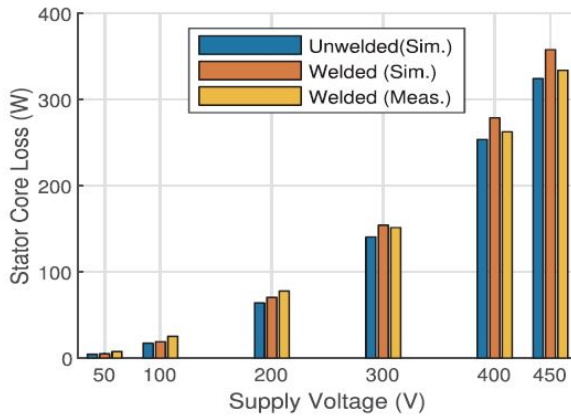


Figure 4.24: Simulated and measured core losses of the blocked rotor setup at 50 Hz excitation frequency for increasing levels of supply voltage.

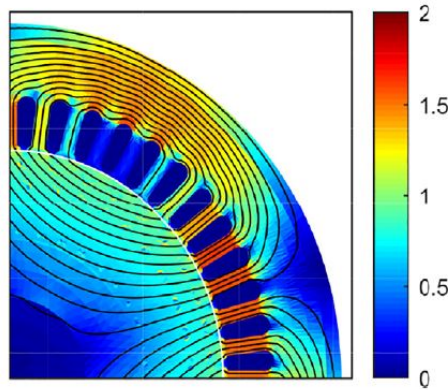


Figure 4.25: FE-simulation result showing the flux density distribution (T) of the induction machine at 400 V supply voltage and 50 Hz excitation frequency.

4.4. Interlocking effects in NO27 ring cores

The magnetic properties of electrical steel locally deteriorate near the interlocked region. Additionally, when the electrically insulating coating between laminations breaks, parasitic eddy current circuits further increase the core losses. Without considering these eddy current circuits, a general methodology is described which uses only Epstein strip measurements to parametrize an accurate model of the effects of interlocking on the local magnetic properties in electrical steel laminations. The model is afterwards validated on re-

alistic stator laminations to show the transferability of the methodology to alternative geometries.

4.4.1 Experimental setup and methodology

In this methodology the effect of interlocking is systematically modelled using magnetic measurements on 3 sets of Epstein strips, as shown in Fig. 4.26. Each set consists of only four strips, so no strips are stacked in this setup, thus eliminating the possibility of interlaminar eddy currents. Each set consists of 2 strips that were cut in rolling direction, and 2 strips in transverse direction. This way, the effect of magnetic anisotropy with respect to the rolling direction is averaged out. Due to the various types of interlocking damage, each set has different magnetic properties, which will be confirmed by the difference in measured BH -curves. Set a consists of undamaged Epstein strips, where no interlocking is applied. Set b has 4 strips with line defect interlocking damage. This line defect forces the total magnetic flux to pass through the damaged region. By comparing the BH -curves of set a and b , information about the magnetic properties of the interlocked zone will be gained. Set c consists of 4 strips with point defect interlocking damage. This point defect represents realistic interlocking damage as it is commonly applied in the stator and rotor of electrical machines. The interlocking damage in set b and c was applied using a punching process illustrated in Fig. 4.27. The strip was locked in a fixed structure that allows space for the downward deformation of the material. The line defect interlock in set b was manufactured with the same tool used for producing set c by performing several consecutive punches in line from edge to edge on the Epstein strip. The interlocking damage in set b and set c is not confined to the visually deformed region. The material near the interlocking deformation is also exposed to mechanical stress, as illustrated in Fig. 4.28. The methodology accounts for these adjacent stress zones by incorporating them in the damaged zone. The methodology proposed here only models the effect of mechanical stress due to interlocking on the local magnetic properties of the electrical steel. In this paper, the methodology is demonstrated on NO27 grade electrical steel. The width and length of the tool used for producing set c were 1 mm and 4 mm, respectively.

4.4.2 Accuracy and repeatability

The methodology requires accurate measurements of the effect of interlocking on the magnetic properties of Epstein strips. Therefore, it is important that the original strips have identical magnetic properties so that any change in magnetic properties can be attributed to the applied interlocking damage. All Epstein strips originate from the same mother coil and are shaped by shear-

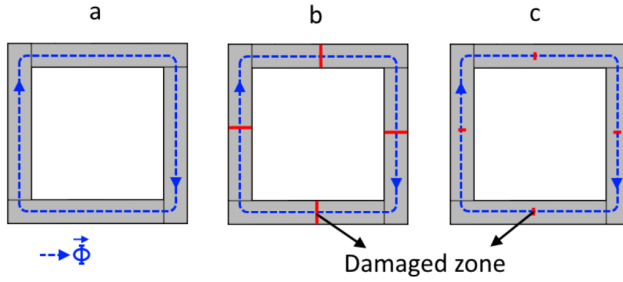


Figure 4.26: Overview of the used sets of Epstein strips. Undamaged Epstein strips (set *a*), line defect interlock (set *b*) and point defect interlock (set *c*).

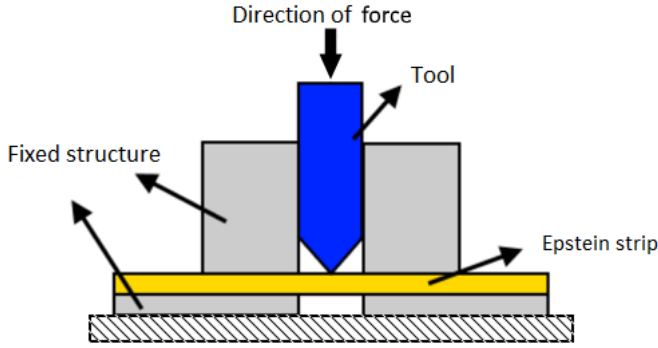


Figure 4.27: Schematic overview of the manufacturing process of the interlocking damage for the samples *b* and *c* in Fig. 4.26. After the punch, the V-shaped tool creates an interlocking damage causing the sample to be formed similar to the laminations in Fig. 4.28.

ing. To verify the repeatability of the applied interlocking technique, the BH -curve was measured three times, each time on a completely different set of four Epstein strips with point defect damage (Fig. 4.29). The curves show that the Epstein strips have very consistent magnetic material properties, and that the interlocking technique is sufficiently repeatable to apply the methodology. The average deviation ϵ_{avg} over all measured points in Fig. 4.29 is 6.3 % as calculated by

$$\epsilon_{avg} = \frac{1}{N} \sum_i^N \frac{|H_{max,i} - H_{min,i}|}{\frac{1}{3}(H_{b1,i} + H_{b2,i} + H_{b3,i})} \quad (4.6)$$

where N represents the 15 points measured on each of the three sets of strips. $H_{b1,i}$, $H_{b2,i}$ and $H_{b3,i}$ are the measured values on each of the three

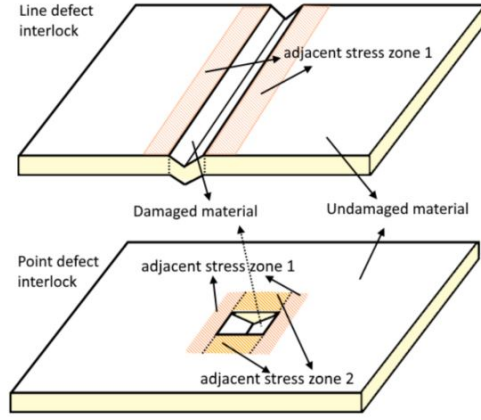


Figure 4.28: Illustration of adjacent stress zones affected by the interlocking damage for line defect interlock (set *b*) and point defect interlock (set *c*).

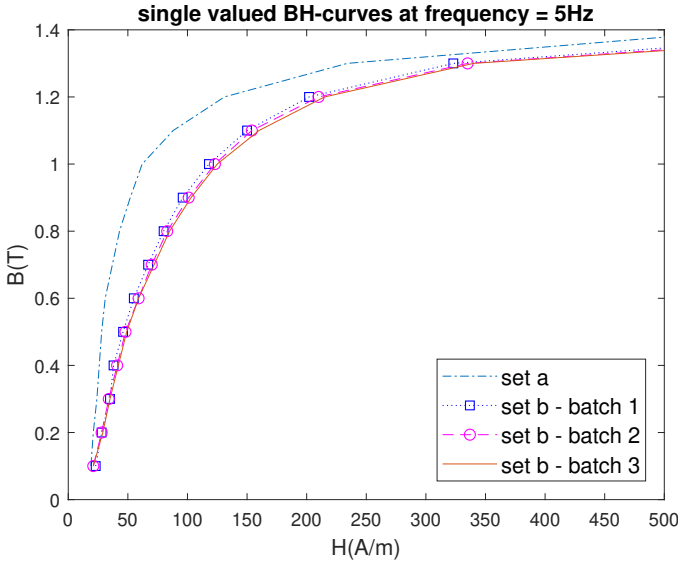


Figure 4.29: *BH*-curves of 3 sets of point defect interlocking NO27 Epstein strips, confirming the consistency and repeatability of the measurement setup, magnetic properties of the Epstein strips and of the applied interlocking technique.

sets of strips for a given B_i and $H_{max,i} = \max(H_{b1,i}, H_{b2,i}, H_{b3,i})$ and $H_{min,i} = \min(H_{b1,i}, H_{b2,i}, H_{b3,i})$.

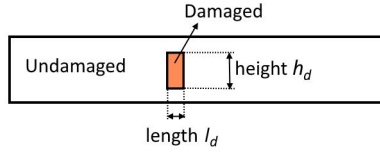


Figure 4.30: Illustration of the simple 2D model of interlocking damage, which can be implemented in any 2D finite element software.

4.4.3 Core Loss Model

The core loss measured in electrical steel is modelled according to the SLT with parameter α set equal to 2, as in (4.5). In the interlocking model, both the undamaged and damaged material zones are characterized by their proper BH -curve and loss coefficients. Hence, the material parameters are fitted for both the undamaged and damaged material, similar to the approach used in the welding model in 4.3.

4.4.4 Methodology for Modelling Interlocking Effects

The result of the proposed methodology is a simple degradation model of the material affected by interlocking stress, which can be directly implemented in any 2D FEM code. This model represents the interlock as a rectangular degraded zone within non-degraded, undamaged material (Fig. 4.30). The degraded zone is parametrized by its height h_d , length l_d and proper magnetic permeability μ_d and loss coefficients, which can be modelled by correctly executing the methodology. Fig. 4.31 shows an overview of the methodology, which is explained in more detail in the following paragraphs.

In step 1, the BH -curves of sets a , b and c are measured. The properties of set a act as the reference for the undamaged material in the rest of the methodology. The measured curves of b and c will be used to parametrize the damaged material.

In step 2, core losses are measured on set a and b over a range of peak flux densities and frequencies. Later, in step 7, these core loss measurements will be used to define loss coefficients of the damaged area.

In steps 3 to 6, a 2D FE-model of the point defect interlocking damage in set c should be constructed and used in an inverse problem formulation. In this model, the height h_d and length l_d are fitting parameters. The material properties of the undamaged material are those measured on set a in step 1. The material properties of the damaged area are derived from the measurements on set b and are linked to fitting parameter l_d . Although set b is not a typical interlock geometry, it is used to relate the length l_d to the modelled perme-

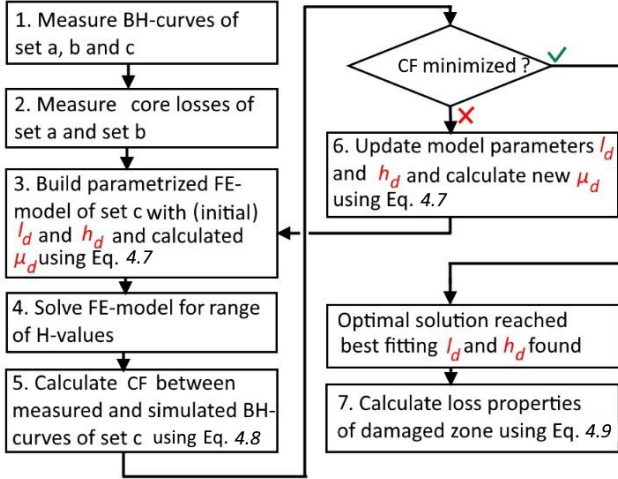


Figure 4.31: Overview of the methodology

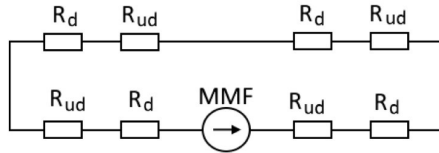


Figure 4.32: Magnetic Equivalent Circuit for set b .

ability of the damaged area by comparing measurements on set b and set a . The configuration of set b (with 4 line-defect interlocks as shown in Fig. 4.26) can be considered as a magnetic equivalent circuit with 1 MMF-source and 8 magnetic reluctances in series: 4 for the damaged zone (R_d) and 4 for the undamaged zone (R_{ud}) (Fig. 4.32). In this circuit, the magnetic flux propagates through R_d and R_{ud} alternately. The total magnetic reluctance of set b is $R_b = 4 R_d + 4 R_{ud}$. In general, the magnetic reluctance can be expressed as $R(B) = l/(\mu_0 \mu_r(B) A)$, where l is the magnetic path length, μ_r is the specific relative permeability and A is the magnetic cross section of the reluctance.

The BH curve measured on set a can be used to calculate $\mu_a(B)$ and is equal to the permeability of the undamaged part of set b , namely $\mu_{ud}(B)$. Since the BH curve measured from set b is valid for the entire set, and since the BH characteristics for the healthy material were measured on set a , the magnetic

permeability of the damaged zone μ_d can be calculated as a function of B using the following equation

$$\mu_d(B, l_d) = \frac{4\mu_b(B)\mu_a(B)l_d}{l_{tot}\mu_a(B) - 4l_{ud}\mu_b(B)} \quad (4.7)$$

where l_{tot} is the total average magnetic path length equal to 940 mm, l_d is the path length of the flux through the damaged line interlock zone which will be a fitting parameter in the inverse problem formulation. Consequently, the path length through undamaged material is defined as $l_{ud} = l_{tot}/4 - l_d$. μ_a and μ_b are the measured magnetic permeabilities for the undamaged set a and line defect set b , respectively. These permeabilities are a function of B following the well-known constitutive relation $\mu_r(B) = B/(H\mu_0)$. There is an important remark to make about the deviation between the realistic and the modelled length of l_d . In reality the damaged zone is larger because the residual stress gradually propagates through the material, as illustrated in Fig. 4.33, and the theoretical value for μ_d is lower than the actual value. This means that μ_d cannot be interpreted as a physical permeability, but by underestimating μ_d , the model accounts for the adjacent stress zone 1 in Fig. 4.28. This assumption is illustrated in Fig. 4.33. The interlocking degradation is assumed to be confined to a well defined region. In this region, the degradation is uniform but the magnetic permeability is also a function of B as defined in (4.7). This equation results in a theoretic relative permeability of the degraded zone which is determined in such a way that the realistic measurements correspond to the model.

Using MATLAB's *fmincon*-algorithm, l_d and h_d can be treated as fitting parameters, with μ_d dependent on l_d as mentioned in (4.7). By iteratively changing h_d , adjacent stress zone 2 (Fig. 4.28) will be compensated and transferred into the damaged zone. The optimization problem applies the following cost function (CF) where the deviation between the measured data and simulated data is minimized:

$$CF(h_d, l_d) = \sum_i \left\| \frac{B_{sim}(H_i) - B_{meas}(H_i)}{B_{meas}(H_i)} \right\|^2 \quad (4.8)$$

The simulated B -values are obtained by averaging the solution for B along the dotted line in Fig. 4.34. The simulated H -values are calculated using the current setpoint and applying Ampère's law. Fig. 4.34 shows an example of this FE-simulation.

In step 7, the loss coefficients of the material in the damaged area can be calculated based on the measurements from step 2. The optimized l_d enables the determination of loss coefficients of the damaged material by analysing the difference in measured losses of set a and b . Differences in measured core

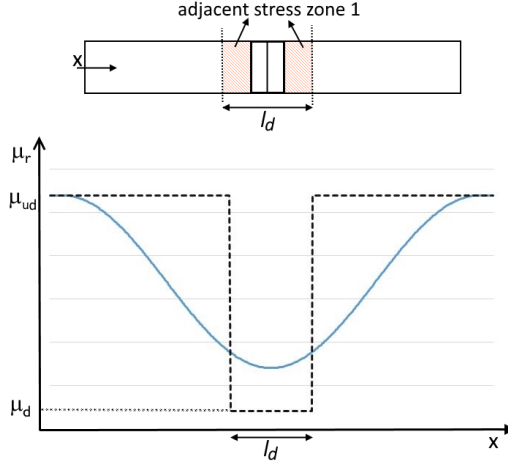


Figure 4.33: Distribution of the realistic gradually degrading magnetic permeability in set b (full line) as a result of the line defect interlock and the theoretical magnetic permeability considered in the methodology (dotted line). This graph illustrates the assumption that the degradation remains confined to a well defined region with an equal magnetic permeability $\mu_d(B)$. This assumption transfers the effect of interlocking damage in the adjacent stress zones to the damaged zone by underestimating $\mu_d(B)$.

losses between set a and b can be attributed to the damaged part of set b . The total specific losses in set b consist of the specific losses in the damaged and undamaged material, weighted according to their specific length in the total set length:

$$P_b(B, f) = \frac{4l_{ud}}{l_{tot}} P_{ud}(B, f) + \frac{4l_d}{l_{tot}} P_d(B, f) \quad (4.9)$$

with P_{ud} and P_d respectively the specific losses of the undamaged and damaged material (both in (W/kg)). Because P_{ud} was measured on set a and P_b was measured on set b , the specific losses of the damaged material $P_d(B, f)$ can be calculated and fitted to (4.9).

4.4.5 Interlocking Tool Characterization on NO27

In this section, the methodology is demonstrated on NO27 grade of electrical steel. The dimensions of the interlocking toolhead are 1 and 4 mm, respectively. Fig. 4.35 shows the interlocking damage in each set for this experiment. The goal of this section is to characterize the effect of the used tool on the magnetic degradation by identifying the parameters (l_d , h_d , μ_d and P_d) of the model using the proposed methodology. According to step 1, BH curves are measured and displayed in Fig. 4.36. In this figure, the effect of interlocking

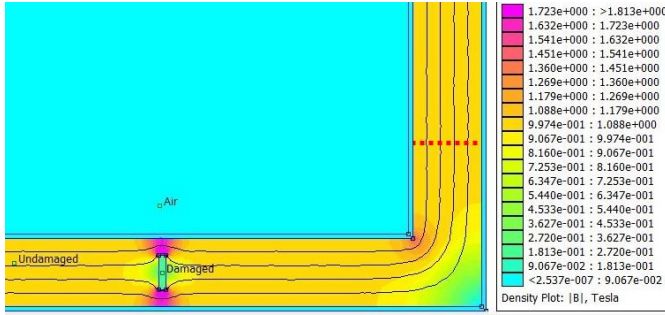


Figure 4.34: Simulated magnetic flux lines and magnetic flux density distribution obtained from FE-simulation of the point defect interlocking damage in set c.

damage on the magnetic properties becomes apparent. The interlocking stress causes the average magnetic permeability of the material to decrease. The degradation is more severe for the line defect interlock (set *b*) than for the point defect interlock (set *c*). Hence the BH curve of set *c* lies between the curves of set *a* and set *b*. In step 2, core loss data is obtained at controlled frequencies from 10 to 200 Hz and sinusoidal flux density peak values from 0.1 to 1.5 T. A sample of these data is displayed in Fig. 4.37. In steps 3 to 6, the FE-model is built and optimization carried out. In this case, the optimal h_d and l_d were 20 mm and 8 mm, respectively. Fig. 4.38 shows the correspondence between the simulated BH curve obtained from the FE-model with modelled interlocking damage and the measured BH curve from set *c*, after the optimization is finished. The optimized model parameters which enabled the construction of the simulated BH curve can be used for further application and validation of the model. With l_d known, the optimal μ_d is also identified using (4.7). The BH curve of the damaged zone is displayed in Fig. 4.39. This curve can be used directly to characterize the damaged region, modelled in any 2D FEM package. The difference between the modelled curve of the damaged material and the originally undamaged curve is substantial. However, the severely damaged material properties - in combination with the identified geometrical parameters l_d and h_d - are calculated so that the model corresponds accurately to the measurements.

According to step 7, the losses of the damaged material can now be calculated. The core loss coefficients in W/kg of the undamaged material as measured in step 2 are $C_{hyst} = 0.0087$, $C_{cl} = 1.4e-10$ and $C_{exc} = 0.001$. The core loss coefficients in W/kg as calculated using (4.9) with optimized $l_d = 8$ mm are $C_{hyst} = 0.0129$, $C_{cl} = 1.34e-5$ and $C_{exc} = 8.5e-4$. It should be noted that the large difference in fitted classical loss coefficients is a result of the fitting procedures and might not correspond to the actual physical nature of the classical loss component.

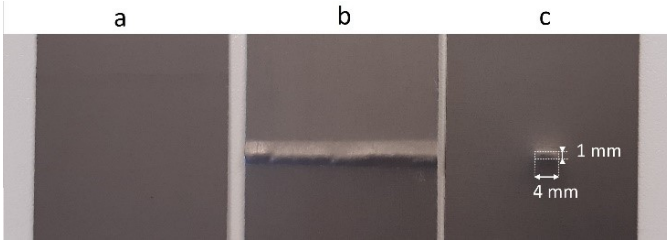


Figure 4.35: Picture of the interlocking defects applied to Epstein strips necessary for constructing sets *a*, *b* and *c*. The dimensions of the interlocking tool are indicated on the picture of set *c*.

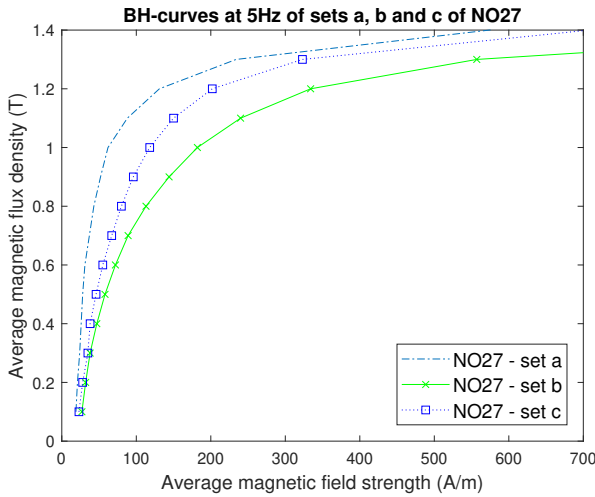


Figure 4.36: Measured *BH*-curves of NO27 electrical steel grade in configurations *a*, *b* and *c* as displayed in Fig. 4.26. The degrading effect of interlocking is most noticeable between 0.7T and 1.2T.

It is now possible to insert the rectangular damaged area with optimized l_d , h_d and core loss coefficients into a FE-model of set *c*. This model can simulate average core losses of set *c*, for different levels of peak magnetic flux density. When comparing the simulated losses to the measured losses, an accurate correspondence is found. This proves that P_d , which was found using core loss measurements on set *b* and (4.9), can be used for predicting the losses in set *c*. An example of this validation is shown in Fig. 4.37.

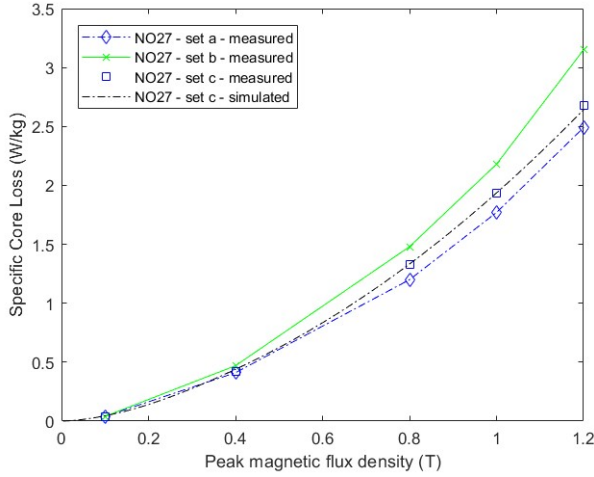


Figure 4.37: Measured core losses at 100 Hz sinusoidal flux density waveform for NO27 grade for sets *a*, *b* and *c*. The simulated core losses of set *c* are added to demonstrate the correspondence with the measurements.

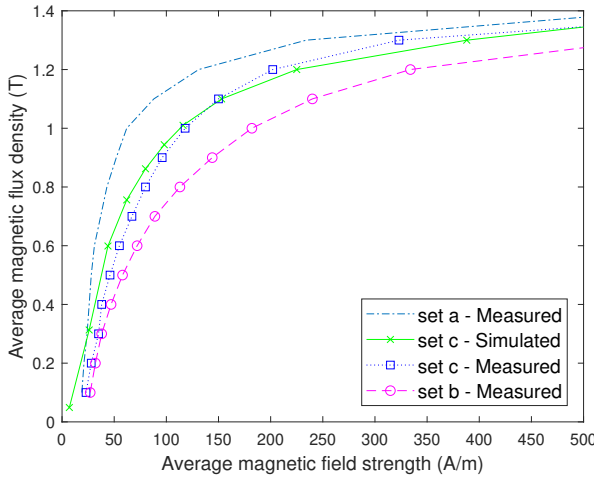


Figure 4.38: Comparison of BH -curves obtained from FEM-simulation and measurements for point defect interlock set *c*. The FEM-simulated BH -curve was obtained from a FE-model with optimized damaged zone parameters $h_d = 20\text{mm}$ and $l_d = 8\text{mm}$.

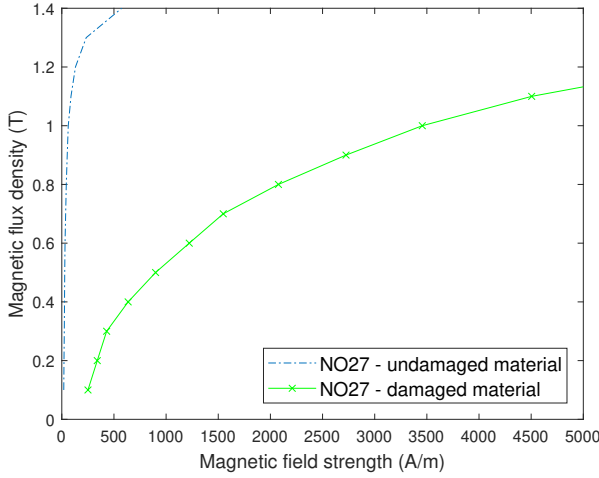


Figure 4.39: *BH*-curves of the damaged material in the NO27 electrical steel due to interlocking, as obtained from the proposed methodology. This curve can be used directly to the damaged region of Fig. 4.30, modelled in any 2D FEM package. The original *BH*-curve of the undamaged material is added as a reference.

4.4.6 Effect of anisotropy

In the previous section, the results shown are based on measurements of Epstein strip sets with 2 strips cut in the rolling direction (RD) and 2 strips in transverse direction (TD). This way, the effect of magnetic anisotropy on interlocking was averaged out. In this section, measurements are presented that demonstrate the effect of interlocking on the magnetic anisotropy of electrical steel. Two sets of strips were manufactured by shearing. The first set consists only of strips that were cut parallel to the rolling direction. The second set was cut perpendicularly to the rolling direction. The *BH*-curves of both sets were measured before and after applying point defect interlocking (similar to the damage in set *b* in Fig. 4.26). Fig. 4.40 shows the measured curves. There is a clear difference in the required magnetic field strength *H* for obtaining the same magnetic flux density *B*. The degrading effect of interlocking can be calculated quantitatively:

$$\delta = \frac{1}{N} \sum_i^N \frac{|H_{d,i}(B) - H_{ud,i}(B)|}{H_{ud,i}(B)} \quad (4.10)$$

where *N* is the amount of measurement points in each *BH*-curve, and where the required magnetic field to obtain a controlled *B* is *H_{ud}* for the undamaged set (before interlocking) and *H_d* for the damaged set (after interlocking). Each

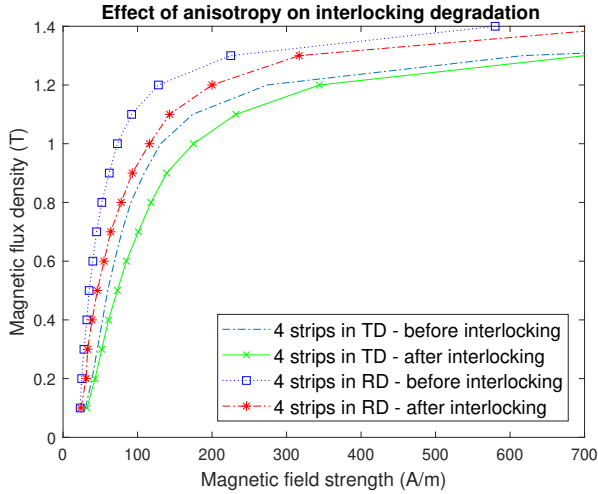


Figure 4.40: Measured BH -curves of two sets of NO27 Epstein strips cut in RD and TD, before and after interlocking.

BH -curve was measured at 5Hz and consists of 15 datapoints. δ was calculated for the set of strips in RD (δ_{RD}) and TD (δ_{TD}), both before and after interlocking. δ_{RD} was 37 % and δ_{TD} was 22 %. The difference between δ_{RD} and δ_{TD} is more significant than the repeatability of the interlocking technique, which was investigated in section 4.4.2. These results show that interlocking causes a greater degrading effect in the rolling direction than in the transverse direction. Additionally, the proposed methodology was applied to the set of 4 RD-strips and the set of 4 TD-strips with the goal of demonstrating how the resulting model parameters deviate. When executing the methodology on the set of strips that were exclusively cut in TD, the resulting model parameters l_d and h_d were 6 mm and 26 mm, respectively. Based on the measurements on strips that were cut exclusively in RD, the resulting model parameters l_d and h_d were 8 mm and 16 mm, respectively. The area of the damaged zone is larger for the RD strips than for the TD strips. In Fig. 4.41, the accurate correspondence is depicted between the measured BH curve and the simulated BH curve of set c after optimization of the model parameters.

4.4.7 Model Validation

In this section, it is proven that the proposed methodology based on Epstein frame measurements, is capable of accurately predicting interlocking effects for a realistic motor lamination. The results of the methodology application on NO27 are applied to a 2D FE-simulated stator core of the same NO27 material

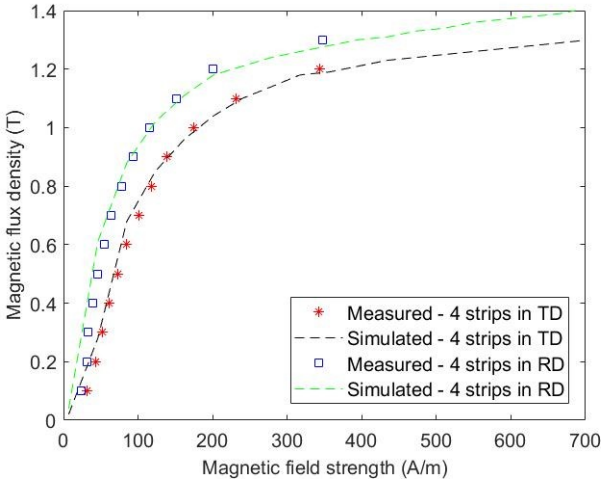


Figure 4.41: Measured and simulated BH curves of the point defect sets (set c) of Epstein strips cut in TD and RD, proving that the proposed methodology is accurate for both BH curves measured in RD and TD.

for the purpose of model validation. The properties of the damaged part μ_d , l_d , h_d and P_d were obtained using the proposed methodology. On this stator core lamination (Fig. 4.42), the measured and simulated BH curves before and after interlocking were compared to validate the model. The dimensions h_d and l_d of the damaged rectangle as modelled by the proposed methodology may differ from the visible interlock size on the photo, but nevertheless the magnetic behaviour of the interlock is accurately modelled. The stator core was manufactured using nibble punching and 4 interlocking points were applied using the same tool as used in previous sections to create set c. This interlocking tool has a rectangular shape of 1 mm by 4 mm. In the NO27 Epstein strips with point defect interlock, the longest edge of the interlocking tool was oriented perpendicular to the direction of the magnetic flux. In the NO27 stator geometry (Fig. 4.42), the longest edge of the interlocking tool was oriented parallel to the direction of the magnetic flux lines. This means that the orientation of the interlocking points in Fig. 4.42 is rotated by 90° with respect to the sets of Epstein strips used for the methodology. Therefore, the rectangular damaged area in the FE-model of Fig. 4.42 was also rotated by 90° . This was done to demonstrate the generality of the methodology. Also, because the cutting technique for creating the stator core differs from the cutting technique for the Epstein strips, the material properties of the undamaged part in the FE-model are obtained from the measured properties of the undamaged stator lamination. Figure 4.43 shows the measured and simulated BH curves of the

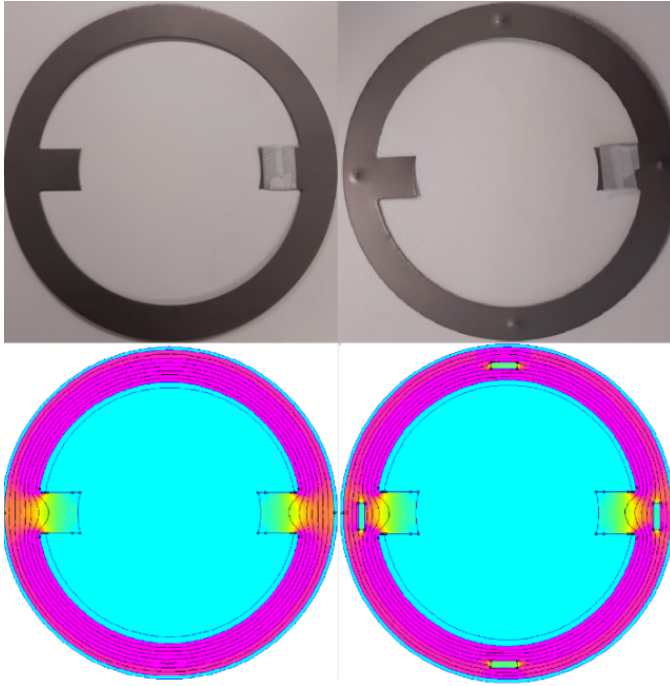


Figure 4.42: Pictures and FE-simulations of the stator core lamination before (left) and after (right) applying interlocking damage. 4 interlocking defects were added around the yoke.

stator core before and after interlocking. The measured curve was obtained using the ring core measurement principle by winding a double concentric coil around the stator yoke. The setup-specific properties such as S , n_1 , n_2 and l_a were also adapted to measure the BH curves correctly according to the ring core measurement principle. The simulated BH curve of the stator core with 4 interlocks is obtained solely by the proposed methodology, which is based on Epstein measurements. This simulated curve matches the measured BH curve on the realistic stator geometry (blue) closely. Using (4.10), the magnetically degrading impact of interlocking can be quantified for the simulated BH curves (δ_{sim}) and for the measured BH curves (δ_{meas}). This equation results in $\delta_{meas} = 31\%$ and $\delta_{sim} = 28\%$, proving that the simulated degrading impact approximates the measured degrading impact. This confirms that the proposed Epstein-based methodology, which parametrizes a simple interlocking degradation model, is able to incorporate interlocking effects on the magnetic properties in 2D simulations of realistic motor laminations accurately.

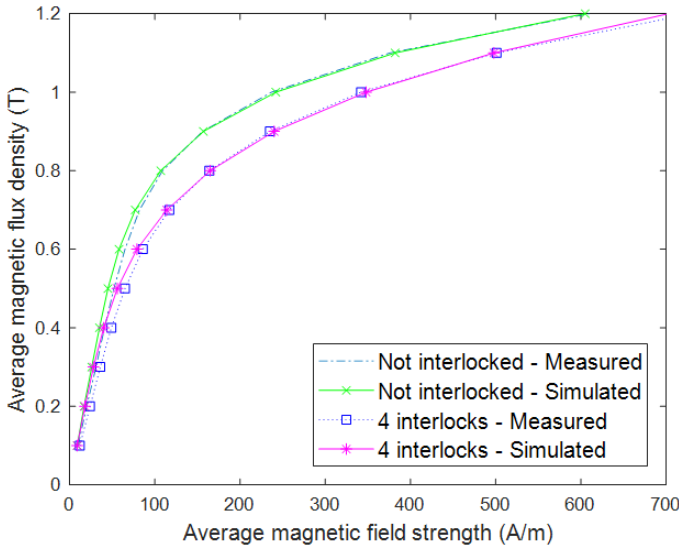


Figure 4.43: Measured and simulated BH curves of NO27 stator core before and after interlocking.

4.5. Conclusion

The goal of this chapter was to present a series of modelling techniques that can be utilized for building a degraded material model for electrical steels.

First, a cutting effect model using several sets of Epstein strips with varying strip width and cutting techniques was elaborated and applied for M100-23P GO steel. In this model, the relative magnetic permeability is defined as a function of the distance to the closest cutting edge. Since the classical loss component is unaffected by cutting stress, only the hysteresis and excess loss component were redefined as functions of the distance to the closest cutting edge. The cutting effect model was applied to a MEC model of a YASA machine. It was found that model parameters fitted on measurements of the laser cut strips produced a decrease in EMF of up to 1.25 % and a decrease in motor torque of up to 1.2. %. Simultaneously, the simulated core losses in the machine model were up to 180 % higher for the laser cut steel than for the water-jet steel. From this experiment, it can be concluded that the cutting technique primarily impacts the machine core losses.

Secondly, the impact of welding was incorporated into a full machine model using permeability and core loss measurements on M400-50A welded stator cores. In this approach, the stator yoke material was assumed uniform and any local magnetic degradation effect due to welding was neglected. A sim-

plified loss model was fitted for the M400-50A material both before and after welding. Hence, the impact of welding was captured in the loss components of the loss model. These loss coefficients were then used in a FE model of an induction machine where the yoke material was also considered uniform and different from the stator tooth material. The FEM simulations indicated that - at full load condition - the machine produced 10 % more core losses with the welded loss properties than with the unwelded loss coefficients. Afterwards, the machine simulations were compared to measurements on a 37 kW induction machine with blocked rotor. It was found that the stator core losses calculated in the FEM simulation deviated from the full machine measurements by approximately 8 % at rated voltage supply.

Finally, the impact of interlocking was modelled using methodology based on measurements of 3 distinct sets of Epstein strips. The methodology considers local degradation effects of interlocking by assuming a rectangular degraded area on the location of the interlocking point. This size and magnetic properties of this area can be identified by using the methodology. This approach was demonstrated on an Epstein strips of NO27 grade and it was found in the validation that the methodology succeeds accurately in predicting the global average BH curve of an interlocked NO 27 ring core.

5

Influence of Stress on Magnetic Properties

The stresses occurring in the laminations of electrical machines originate from several different sources. These stresses can be categorized as 'external' or 'internal', depending on the source of the load. In this classification, external stress is, to a certain extent, essential for machine operation. The centrifugal forces in the rotor sheets can cause large tensile stresses while rotating. Simultaneously, the stator sheets experience tangential forces acting on the motor housing. On the other hand, internal stress is related to the construction of the machine and is present even when the motor is not being used. Shrink fitting the stator yoke in the housing leads to compressive stress in the radial direction. Cutting the individual laminations for the mother coil leads to deformation and plastic stress near the edges. Joining the laminations to form a fixed stack is usually done by compressing the stack and welding or interlocking the sheets, which leads to complex internal stress distributions that are inherent to the manufacturing process of the machine.

Because external stress is fundamental to the normal motor operation, the negative effects on the material properties are difficult to avoid. Contrarily, the internal stress introduced during the manufacturing of the machine can be studied so that the negative effects on the machine performance are min-

imized. As a first step towards this goal, the complex relation between stress and magnetic behaviour should be investigated. Then, the specific manufacturing stress should be measured in order to have a local and accurate mapping of the stress distribution. Finally, models can be built which predict the global magnetic properties of electrical steel stacks based on the known stress distribution and its relation to the local magnetic properties.

5.1. Relation between mechanical stress and magnetic properties in literature

Appropriately, most studies coupling magnetism and mechanical stress in materials involve obtaining measurement data. Experimental setups have been built for simultaneous measurement of global magnetic properties and externally applied stress. This enables an effective quantization of the effects of stress on magnetization. However, the angle between the magnetic field direction and stress direction has a significant impact on the measured magnetic properties [81], [6]. In this section, a distinction is made between setups on the basis of the orientations of stress and magnetic field.

Considering the relation between the material microstructure and its behaviour during magnetization, it seems obvious that any stress acting on this microstructure also affects its magnetic properties. Domain theory as a framework links the domain structure of electrical steel to its magnetic properties. Consequently, researchers have studied the magnetomechanical relation from the viewpoint of domain theory as a means to explain the observed effects.

5.1.1 Parallel stress and magnetic field

In [53], [31], [57], [42], [28], [39] and [66] the relation between an externally applied static load and the magnetic properties of a single sheet of electrical steel was investigated using modified SST setups. A standard SST was fitted onto a support frame and the sample sheet is clamped on both sides in the direction of the magnetic field. Using a load mechanism, the sample is placed under stress while a load cell measures the applied force. In Table 5.1, an overview of the experiments and measured properties is given.

From these experiments, preliminary conclusions can be drawn. Difficulties arise when measuring high compressive stresses due to the buckling of samples. Thin sheets of electrical steel are not suitable for sustaining high compression. In every case, the measured losses increase dramatically when the sample was placed under compressive stress. Under small tensile stress (below the material's yield strength), the core losses are generally lower when compared to the unloaded state. With a tensile stress greater than the yield

strength, the material is plastically deformed and the core losses increase with respect to the unloaded state. In some reports, a core loss analysis was done to separate the effect of stress on the different loss components. In general, it is found that the classical losses are unrelated to the applied stress. The main contribution of the change in core losses originates from the hysteresis component. In some cases, e.g. [66] and [53], the relation between stress and the excess loss component was reportedly similar to the hysteresis loss component. Because of the strong dependence of the hysteresis loss on the applied stress, it is assumed that the domain wall configuration within elementary domains changes the domain wall motion under magnetization. When a relatively small tensile stress is imposed parallel to the applied magnetic field, the added magnetoelastic energy alters the domain configuration and the magnetization process is more energy efficient. This new configuration favours growth of domains which are parallel to the applied field at the expense of the perpendicular domains. The initial decrease and subsequent increase of the hysteresis losses with increasing tensile stress implies that there must be an optimal domain configuration for which the core losses are minimized. This minimum is typically found when the electrical steel is stressed uni-axially in the tensile elastic region between 20 and 40 MPa [66], [53]. In [57], an intuitive approach using domain theory suggests that for a fixed variation of the magnetization, the 90° domain walls need to move 1.41 times further than the 180° domain walls. 90° domain wall movement is therefore less efficient and more subject to pinning. Tensile stress decreases the area of the 90° domains and consequently increases the magnetic permeability and lowers the hysteresis losses. Increasing the tensile stress even further results in a further decrease of the area of the 90° domain walls, but this can be unfavourable to the magnetostatic energy which strives towards minimization by maintaining a minimal distance between neighbouring 180° domain walls. This might explain the appearance of an optimal domain configuration under small tensile stress.

The dramatic degradation of the magnetic properties when subject to plastic deformation is commonly attributed to the increase in dislocation density when the material is strained beyond the yield strength. An increase in dislocation density leads to the formation of pinning sites which are known to impede domain wall motion. In [43], measurement data was obtained where the samples were plastically deformed and afterwards released. In this state, it is assumed that the samples contain a certain amount of (presumably compressive) residual stress. Several samples with increasing amounts of strain deformation were manufactured. In this unloaded state, the BH loop and magnetostriction were measured and the permeability, coercivity and remanent magnetization were plotted. The coercivity linearly correlated with increasing strain deformation while remanent magnetism and permeability exhib-

Table 5.1: Details of magnetomechanical experiments found in literature. A negative stress implies compression and a positive stress implies tension.

<i>Reference</i>	<i>Material</i>	<i>Range (MPa)</i>	<i>Measured properties</i>
[53]	50H290	-60 to +440	Core loss
[31]	M250-35A	0 to +142	Core loss
[57]	M330-50A	-30 to +80	Magnetostriction
[42]	n.a.	-50 to +80	Core loss
[28]	n.a.	0 to +650	Permeability Barkhausen Noise Coercivity
[39]	M270-50A	0 to +530	Hysteresis loops
[66]	M400-50A	-40 to +100	Core loss

ited non-linearly decreasing behaviour. The magnetostriction loop displayed highly irregular behaviour with increasing levels of strain. It is concluded in this paper that the changes in magnetic properties can be related to the generation of new pinning sites during the deformation process which cause a linear increase in the coercive field.

On the other hand, previously unloaded samples subjected to static compressive stress experience a sharp increase in hysteresis losses. In this case, the opposite from the small tensile stress occurs. According to [42], the domains with an easy axis closer aligned to the transverse direction benefit from a compressive stress, thus making the global magnetization more energy intense. As a consequence to this reorientation, the permeability decreases and total core loss increases.

5.1.2 Stress parallel to stacking direction

The uni-axial stress state described in the previous section gives an interesting insight in the magnetomechanical relation. Unfortunately, this specific uniform stress rarely occurs over a large area in real machine applications. However, in some cases the stack is compressed in the axial direction before the laminations are joined. This is done to ensure a close contact between the laminations and to avoid any interlaminar air gaps. When the stack is compressed and subsequently joined, it can be assumed that a residual axial compressive stress maintains within the stack. This residual stress might also have a significant impact on the magnetic performance of the stack, which is why the effect of this axial stress should be accounted for when analysing the manufacturing process of electrical machines. The rationale seems straightforward, yet comparatively few research papers report on this specific stress state. In [32], a ring core stack made from 50A290 steel was placed in a compression cell and

the stress was increased up to 10 MPa. It was found that the core losses, measured at 50 Hz, initially increased with increasing compression stress up to 4 MPa, after which the core losses decreased with respect to the unloaded state. [4] manufactured a similar setup and was able to increase the compressive stress on a stack of 35WW300 ring shaped laminations up to 30 MPa. The same trend appeared when plotting the measured core losses against the increasing compressive stress, but the core losses decreased only after 15 MPa. The core losses peaked at approximately 16 % above the stress free core loss value at 10 MPa. A separation of losses was done which indicated that only the hysteresis loss component was affected by this stress. In [74], another ring core compression setup was presented and core losses were measured at frequencies up to 2 kHz and 10 MPa. A dramatic increase in core losses was attributed to the additional eddy currents flowing through the edge burr. Presumably the compressive stress improves conductivity in the short circuit connection on the cutting edge of the laminations. All of the previously mentioned papers used ring cores to measure the effect of compressive stress. A different approach was used in [46], where an SST was fitted with a load mechanism and local compressive stress in the thickness direction was imposed up to 10 MPa. Similar to the other reported results, the permeability decreased and core losses increased significantly up to a certain level of stress, after which the degradation stabilized and in some cases the properties even improved.

5.1.3 Multi-axial stress and magnetic field

As suspected from the results from the uni-axial measurements, the relation between stress and magnetic properties is strongly dependent on the directions of stress and magnetic field in the material. Traditional magnetomechanical setups have therefore been elaborated in order to study the case when field and stress are perpendicular [81], [54] or multi-axial [6], [30]. In [6], the core losses of M400-50A electrical steel were measured at 1 T peak flux density while the sample was placed under uniaxial, equibiaxial and pure shear stress. However, the level of applied stress was rather limited and ranged between -30 MPa and 30 MPa. Core losses were measured under various stress states. The results under equibiaxial stress were consistent with the results from uni-axial experiments: When the sample is magnetized in the x direction, the core losses decreased gradually when tensile stress was applied in the x direction and compressive stress was applied in the y direction. Core loss analysis of measurements in all stress states (including shear stress) showed that the evolution of the hysteresis loss component and excess loss component tend to behave very similar.

5.2. Magneto-elastic coupling models

The complex relation between the anisotropy of electrical steels and multi-axial mechanical and magnetic excitation has led to the development of magnetomechanical coupling models. The goal of these models is to predict the effects of multidirectional stress on the magnetic properties, with consideration of the resulting anisotropy. Attempts were done to parametrize these models solely on the basis of uni-axial measurements, which are significantly easier to perform than the multi-axial measurements. This would allow machine designers to model the effect of stress in any direction based on the knowledge of the uni-axial stress relation. One approach commonly found in literature is the equivalent stress technique. This technique is based on the assumption that any multi-axial stress can be substituted by an equivalent uni-axial stress. This equivalent stress can be used to calculate the changes to the magnetic properties occurring the original multi-axial stress. In [18], a short literary overview is given of the equivalent stress models which are valid under bi-axial loading. More interestingly however, an equivalent stress model is proposed and applied which can calculate the equivalent stress under a fully multi-axial mechanical loading. This model is based on an equilibrium in magneto-elastic energy and is defined as

$$\sigma_{eq} = \frac{3}{2} \mathbf{h}^T \mathbf{s} \mathbf{h} \quad (5.1)$$

$$\mathbf{s} = \boldsymbol{\sigma} - \frac{1}{3} \text{tr}(\boldsymbol{\sigma}) \mathbf{I} \quad (5.2)$$

with \mathbf{h} the direction of the applied magnetic field and \mathbf{s} the deviatoric part of the stress tensor $\boldsymbol{\sigma}$, and \mathbf{I} the identity tensor. As shown in [18], it is possible to define a complex multi-axial stress state and subsequently calculate its equivalent stress σ_{eq} . Then, it can be assumed that this calculated stress is parallel to the local magnetic field, and that this stress will modify the magnetic permeability in the same way as the actual multi-axial stress. The validity and accuracy of this model was investigated in further detail in [59].

For the problem of modelling manufacturing effects, such equivalent stresses may simplify the stress state in the laminations where different manufacturing effects cause residual stresses.

5.3. Uni-axial measurements and analysis on M270-35A in plastic tensile region

The lamination material near cutting edges and joining sites is in a plastically deformed state without any external load. Consequently, it can be argued that

the local domain structure is significantly different from the undamaged material and that there are residual stresses present in the material. However, most experimental magnetomechanical measurements reported in literature are done within the lower side of the elastic region. With the purpose of modelling manufacturing effects, insight should be gained into the magnetic properties of steel after plastic deformation. In this section, the uni-axial magnetomechanical properties of deformed steel are measured, both before and after load release. BH curves and core losses are obtained at several frequencies, peak flux density values and increasing levels of tensile strain. Additionally, core loss analysis is done which provides an understanding of the microstructural changes in the domain wall configuration.

5.3.1 Experimental setup and methodology

A modified double-yoke SST where the samples are clamped in a stress bench equipped with a load cell and rotary handle is used for performing the core loss measurements under uni-axial stress (Fig. 5.1). The stress exerted on the sample is controlled with the rotary handle. A calibrated load cell measures the force and allows for an accurate determination of the static stress in the sample. Each turn of the rotary handle causes a fixed amount of strain on the sample. The elongation after each turn is equal to the lead of the threaded axis. All measured samples originated from the same mother coil of NO M270-35A electrical steel. Three sets of samples were manufactured using shearing. The cutting direction differed between the sets. One set was cut with the long edge parallel to the rolling direction (RD), another was cut parallel to the transverse direction (TD), and the last set was cut diagonally at an angle of 45° with respect to the rolling direction (DD). Each sample was placed in the SST setup, clamped and strained to a certain level before the magnetic measurements under load were performed. Afterwards, the load was released, the clamps removed and the measurements were repeated.

Sample elongation or strain was used as the control variable in this experiment. However, such experiment results are typically reported under controlled stress. Therefore, it is necessary to measure the stress strain curve of this material. This way, any strain value under loaded condition can be associated with the uni-axial stress in the sample. Stress strain curves for M270-35A were measured in rolling direction using a tensile tester (Fig. 5.2) which was developed by a company called MTS. The samples used for this measurement were of the same thickness as the steel laminations, but had a width and length of 55 mm and 200 mm, respectively. It should be noted that these samples do not correspond to the standard sample geometry that is normally used for obtaining stress strain curves. The standardized samples have a wider cross section at both ends of the sample, allowing it to be fixed securely in the clamps.

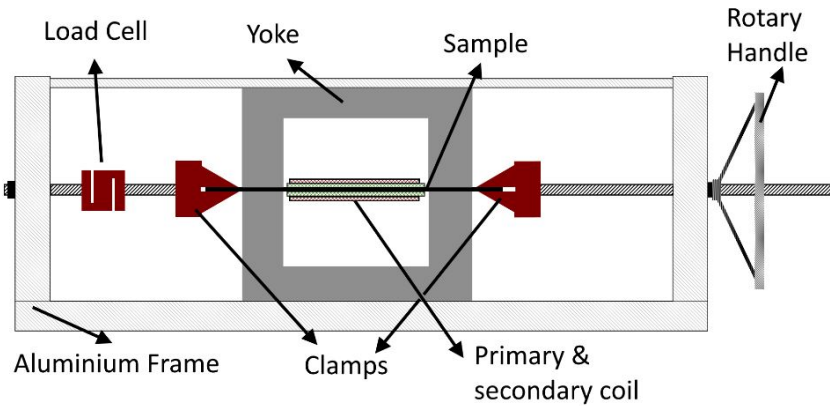


Figure 5.1: Side view of the modified SST setup with stress bench and load cell.

Also, the standard sample cross section is smaller in the middle than on the ends, thus causing a maximal applied stress in the middle section of the sample. This will ensure that the eventual fracture of the sample occurs in the middle. This way, the extensometer will measure the strain up until the point of fracture. By using a sample with different geometry (such as an Epstein strip), the fracture might occur in the region near the clamps. However, after several attempts and careful placement of the sample, it was possible to obtain a measurement over the full range, which ended in a fracture in the middle of the sample. In this instance, the resulting stress strain curve revealed material properties corresponding to the material's data sheet. The traditional dog bone shaped sample used for conventional tensile testing is geometrically different from the Epstein strip samples used in the magnetomechanical SST setup. The dog bone shape ensures a uni-axial stress state over the gauge length of the sample. However, the uniform cross section of the Epstein strip is essential for accurate magnetic measurements. If a dog bone shape is used for magnetic measurements, the measured average magnetic flux density can no longer be assumed to be uniform across the cross section of the sample. Building an accurate setup for measuring magnetic properties under uni-axial stress therefore poses a problem because either the stress distribution or the magnetic flux density distribution is not uniform. This problem could be an interesting topic for further research.

5.3.2 Measurement data

The stress strain curve measured in M270-35A on rectangular strips cut in RD is shown up to 15% strain in Fig. 5.3. A yield strength (0.2% proof) of 428



Figure 5.2: Complete setup available at UGent (Soete Laboratory) for obtaining stress strain curves (left). Close up picture of extensometer device for obtaining accurate measurements of sample elongation.

MPa and ultimate tensile strength of 554 MPa was measured. At the point of fracture, the sample was elongated by 50%.

The effect of plastic strain on the measured BH curves is shown in Fig. 5.4. Even a small amount of plastic deformation has a large impact on the BH curve. When the sample is strained to 1.3 %, the magnetic field strength required to generate a peak flux density of 1.2 T rises from 270 A/m to 1577 A/m. With increasing levels of strain, the magnetic field required to reach a certain flux density increases. When comparing the sets with different cutting direction in Fig. 5.5, it becomes clear that the strain affects the three sets in a similar way. For each set, a load which plastically deforms the sample increases the magnetic field strength required to obtain a certain flux density, and releasing the strain load further degrades the magnetic properties of the sample. In Fig. 5.6, the evolution of the relative magnetic permeability under increasing levels of plastic strain is shown for different levels of B_p . A consistent pattern is found over the displayed range of peak flux densities. An initial dramatic decrease of permeability is followed by a slow further decrease when the strain is increased. On average over the displayed data, the relative permeability initially drops to approximately 20% of the unstrained sample. When the sample is strained further, the relative permeability decreases by 80 per strain percentage increase.

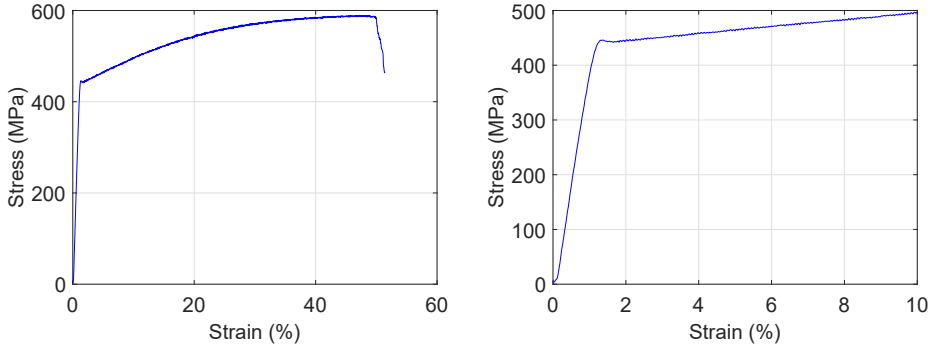


Figure 5.3: Measured stress strain curve on M270-35A steel rectangular samples cut in RD. The full curve is shown on the left, a more detailed version at low values of strain is shown on the right.

In Fig. 5.7, core losses measured are shown on M270-35A steel grade for several levels of plastic strain, both before and after the load was released. From these data, it is clear that the total core loss before release generally increases with increasing levels of strain. When the sample is strained up to 10,4% and before the load is released, the core losses on average increase 105 % over the whole range of plotted data. After the load release, the core losses are increased 198 % with respect to the unloaded samples. The increase is smaller for increasing frequency and increasing peak flux density. The data shows how the core losses after load release are drastically higher than before the release at equal levels of pre-release strain. On average over the whole plotted range, releasing the load after strain increases the core losses by 39%. This increase becomes smaller when frequency and peak flux density increase, indicating that increasing mechanical strain primarily raises the hysteresis loss component. In Fig. 5.8, this effect is compared in samples with different cutting orientations. In the unloaded state, the core losses are highest for the sample cut in TD and lowest for the RD sample. With increasing strain, the losses are consistently higher for the DD and TD samples than for the RD sample. There was no significant difference in added losses due to load release between the three samples.

5.3.3 Core loss analysis using loss separation

As mentioned previously, the measured total core losses P_{tot} can be segregated in hysteresis losses, classical (eddy current) losses and excess losses. Mechanical stress has a distinct impact on each of these components. Consequently, it is valuable to investigate the relation between stress and each loss component.

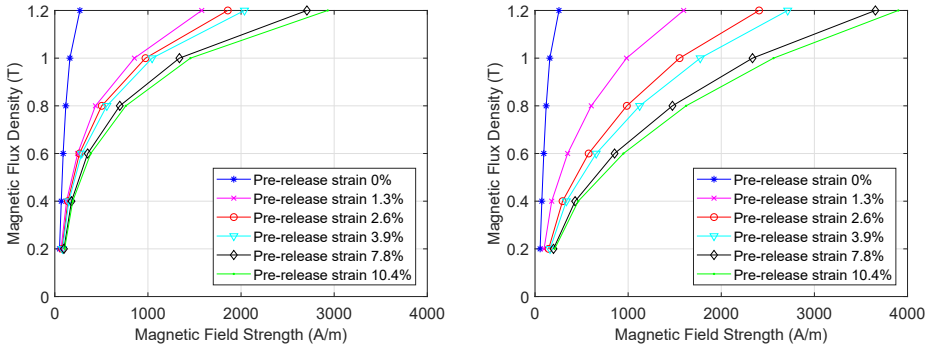


Figure 5.4: Measured BH curves for increasing levels of pre-release strain before (left) and after (right) the load was released.

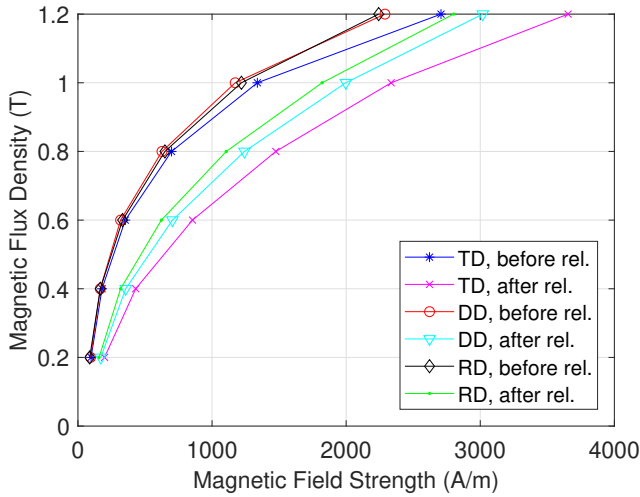


Figure 5.5: Measured BH curves of three differently cut samples at 7.8% strain before and after the load was released.

Analysis using separation of losses is therefore justified. Instead of fitting the core loss components C_{hyst} , C_{cl} and C_{exc} using an inverse problem formulation, the loss separation analysis presented here is done analytically. Considering the separation of power losses (typically expressed in (W/kg)) in terms of energy losses requires a transformation by dividing each term by the frequency f and multiplying with the material mass density ρ to obtain energy density terms in (J/m³)

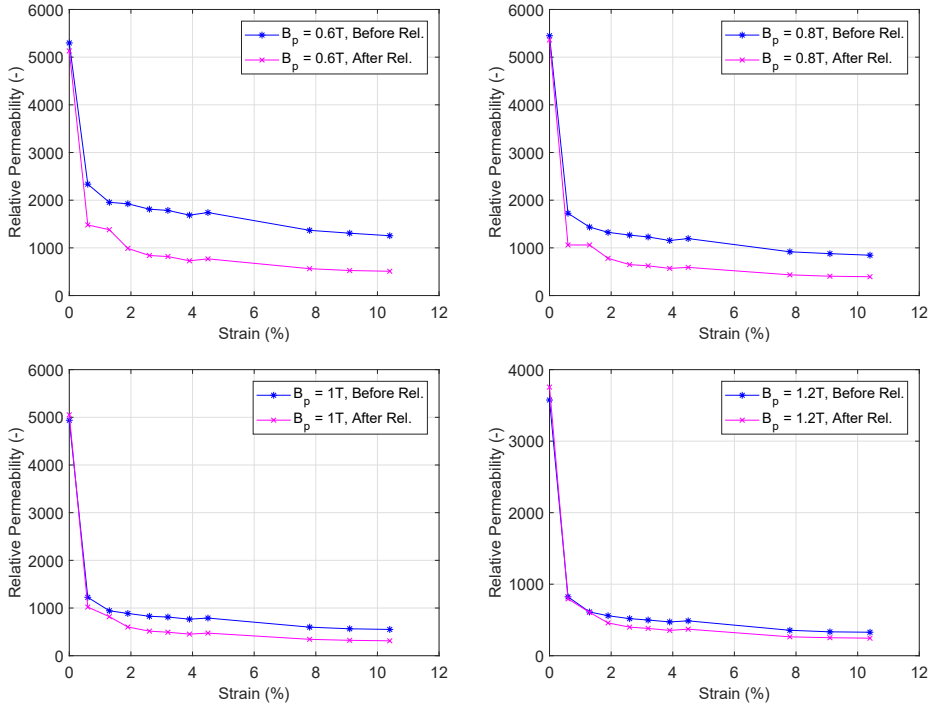


Figure 5.6: Effect of increasing strain in the plastic region on the relative permeability at different levels of peak flux density.

$$W_{tot} = W_{hyst} + W_{cl} + W_{exc} \quad (5.3)$$

In this expression, the classical losses can be calculated analytically

$$W_{cl} = P_{cl}\rho/f = \frac{B_p^2 f d^2 \pi^2 \kappa}{6\rho} \quad (5.4)$$

It can be assumed that the conductivity κ does not change when the material is strained. This was verified in the next section with electrical resistance measurements using the 4-wire method and an RLC meter. Similarly, the excess energy loss can be formulated as

$$W_{exc} = P_{exc}\rho/f = 8\sqrt{\kappa GSV_0}B_p^{1.5}f^{0.5} \quad (5.5)$$

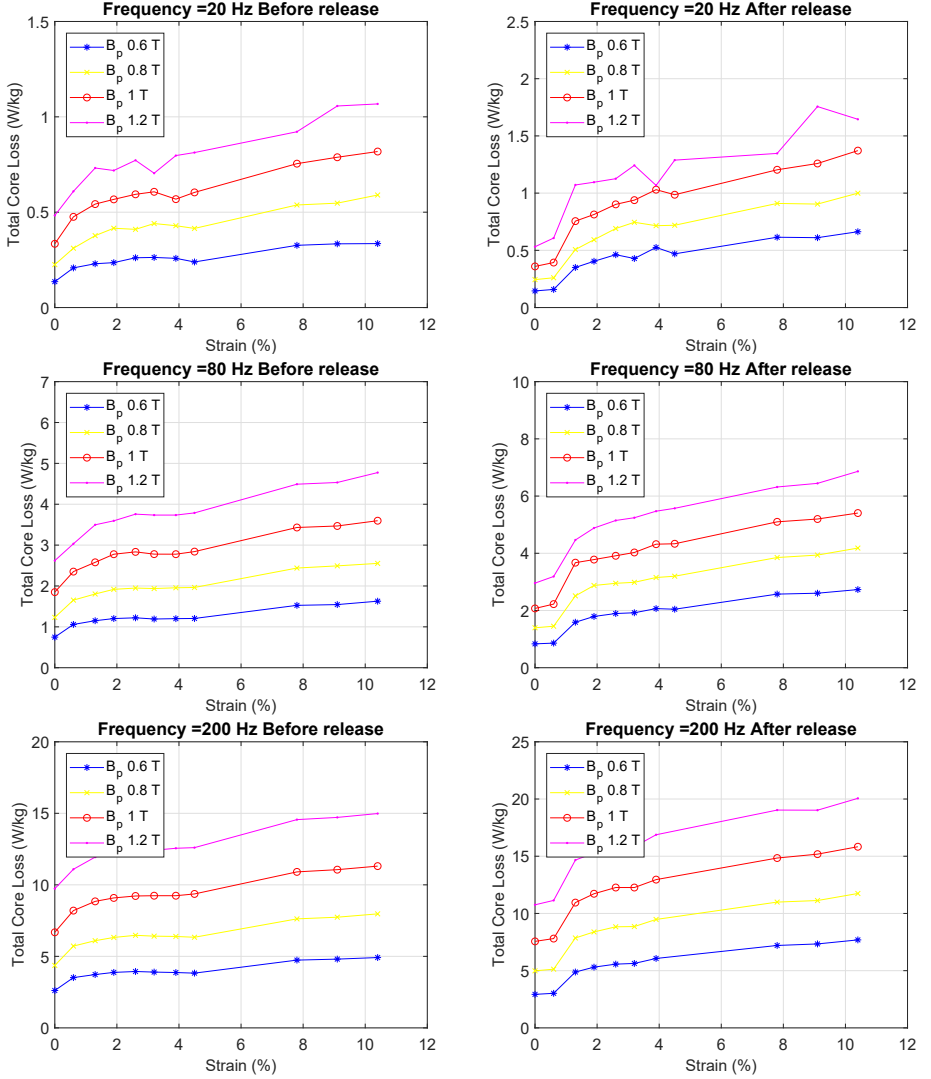


Figure 5.7: Measured core losses in RD on M270-35A before and after load release at different levels of pre-release strain, peak flux density and frequency. It is important to note that the strain values after release represent the strain which was present before the sample was released.

With the classical energy loss known, it can be subtracted from the total loss to find

$$W_{tot} - W_{cl} = W_{hyst} + 8\sqrt{\kappa GSV_0}B^{1.5}f^{0.5} \quad (5.6)$$

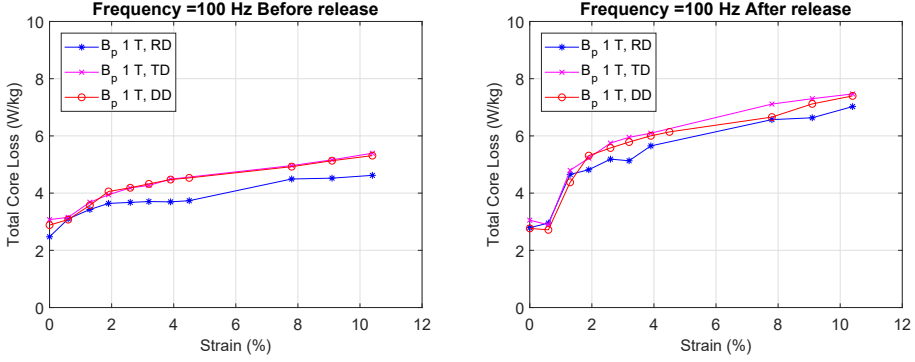


Figure 5.8: Measured core losses in RD, TD and DD on M270-35A before and after release at 100 Hz and peak flux density 1 T.

Extrapolating the difference between the total and classical losses to obtain the loss at $f = 0$ Hz results in an approximation of the hysteresis loss component

$$W_{hyst}(B_p) = \lim_{f \rightarrow 0} \frac{P_{tot} \rho}{f} \quad (5.7)$$

Obtaining an accurate value for the hysteresis energy loss by means of extrapolation implies measuring total losses at several low frequencies and peak flux densities. Then, calculated classical losses can be subtracted from the measured values, and an extrapolation to $f = 0$ Hz will result in the hysteresis energy loss. Consequently, the excess energy component is determined as well as the material related parameter V_0 . It can be assumed that the parameter V_0 together with hysteresis energy loss W_h could describe the effect of the applied external mechanical stress on the microstructure and on the magnetic properties of NO electrical steels, where V_0 describes the influence on losses of various microstructural features such as (among others) grain size, crystallographic texture and residual stresses [53]. Thus, analysis using separation of losses can be used for gaining insight in the microstructure of the steel at different deformation levels.

The applied loss separation methodology has some limitations, namely:

1. The core losses were measured up to 10.4 % strain. Attempts to measure core losses at a higher strain level by further increasing the stress caused local cracks in the sample near the clamps of the setup, which resulted in an erroneous measurement.
2. A more accurate way of expressing the excess loss per cycle is proposed in [10]

$$P_{exc} = 2B_p f \rho^{-1} (\sqrt{(n_0 V_0)^2 + 16\kappa G S V_0 B_p f} - n_0 V_0) \quad (5.8)$$

The stress dependence of the excess loss term can be analysed using the V_0 and the n_0 parameters, as they are both related to the material microstructure. In order to accurately measure the effect of n_0 , low frequency measurements are necessary. However, because low frequency measurements are inherently more noise-sensitive, the n_0 parameter is neglected and the more simplified definition (5.5) of the excess loss was applied.

3. Calculation of the classical loss using (5.4) disregards the skin effect as described in Chapter 2. At high frequencies, the skin depth can become too small which would invalidate the loss separation method. Therefore, the maximum frequency was set to 400 Hz.

The separation of loss technique is applied to the strained samples. For this experiment, core loss measurements were obtained at frequencies 20, 40, 60, 80, 100, 200, 250, 300, 350 and 400 Hz and peak flux densities between 0.2 T to 1.4 T in steps of 0.2 T. For each datapoint, the classical losses are subtracted from the measured losses and the results are plotted as a function of $f^{0.5}$. For the RD sample at 0% and at 10.4% strain, this is shown in Fig. 5.9. Linear regression of each series of data allows the estimation of the hysteresis losses for each level of strain and peak flux density. The hysteresis energy loss can be plotted for increasing level of strain. In Fig. 5.10, this is done for three sets of samples, both before and after release. There appears to be a strong correlation between the effect of strain on the total losses and on the hysteresis losses. The average rise in hysteresis loss before release was 175% for the RD samples, 153% for the TD samples, and 196% for the DD samples. After releasing the load which caused a 10.4% strain, the increase in hysteresis losses with respect to the unloaded state was significantly higher at 407% for the RD samples, 366% for the DD samples, and 363% for the TD samples. With the classical and hysteresis loss determined, the excess loss energy can similarly be plotted (Fig. 5.11). The data is noisy, however some interesting elements can be observed. In these plots, it is clear that the excess loss behaves very differently than the hysteresis loss in samples under strain. In general, it can be concluded that an initial increase in excess losses under small strain is followed by a slow decrease at higher pre-release strains. Although the impact is not as large as for the hysteresis loss, releasing the load marginally decreases the excess core losses. On average over all the plotted results, the excess losses decreased by approximately 13% when the load was released. There was no significant difference in excess loss behaviour under plastic stress between the RD, DD or TD samples. The ratio between the hysteresis loss component and the excess loss component increases with applied pre-release strain, as shown in 5.12.

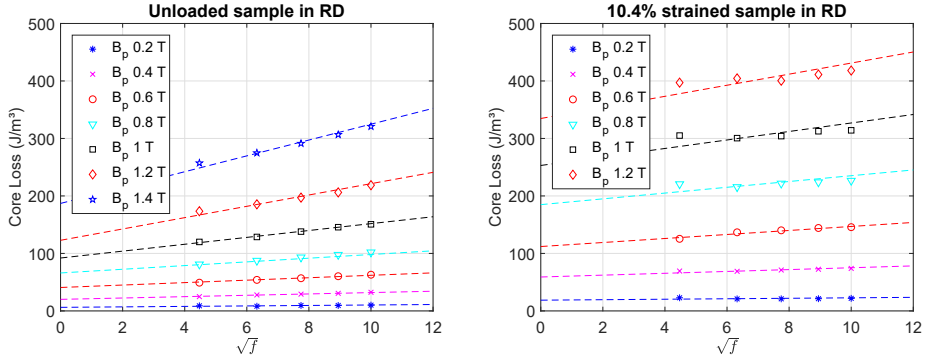


Figure 5.9: Core losses, without classical loss component, plotted in unloaded stress state and 10% strained sample

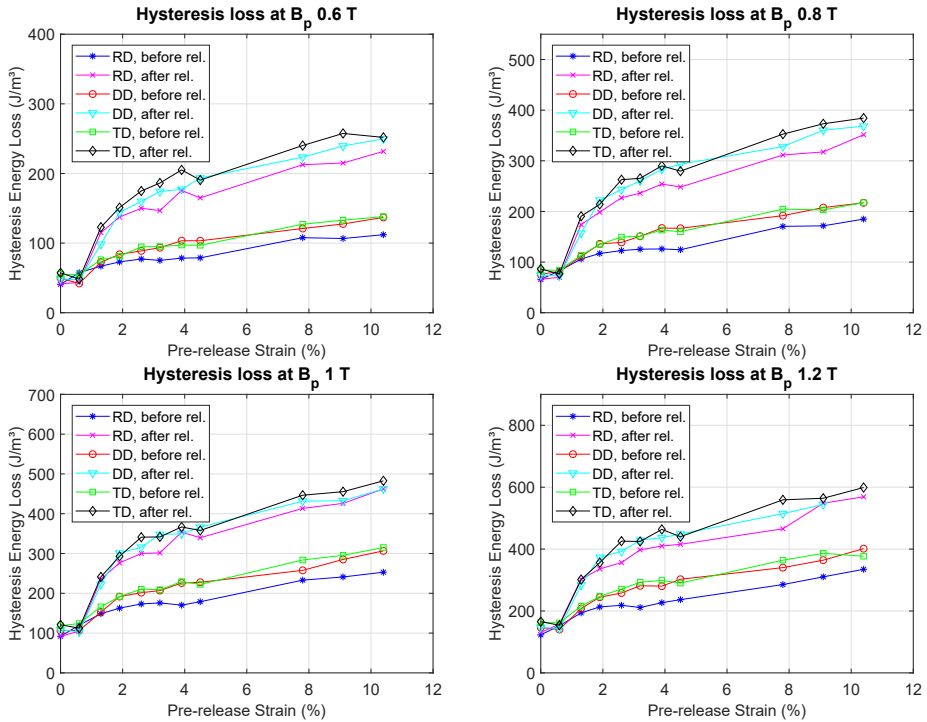


Figure 5.10: Hysteresis energy losses as a function of pre-release strain for different levels of peak flux density.

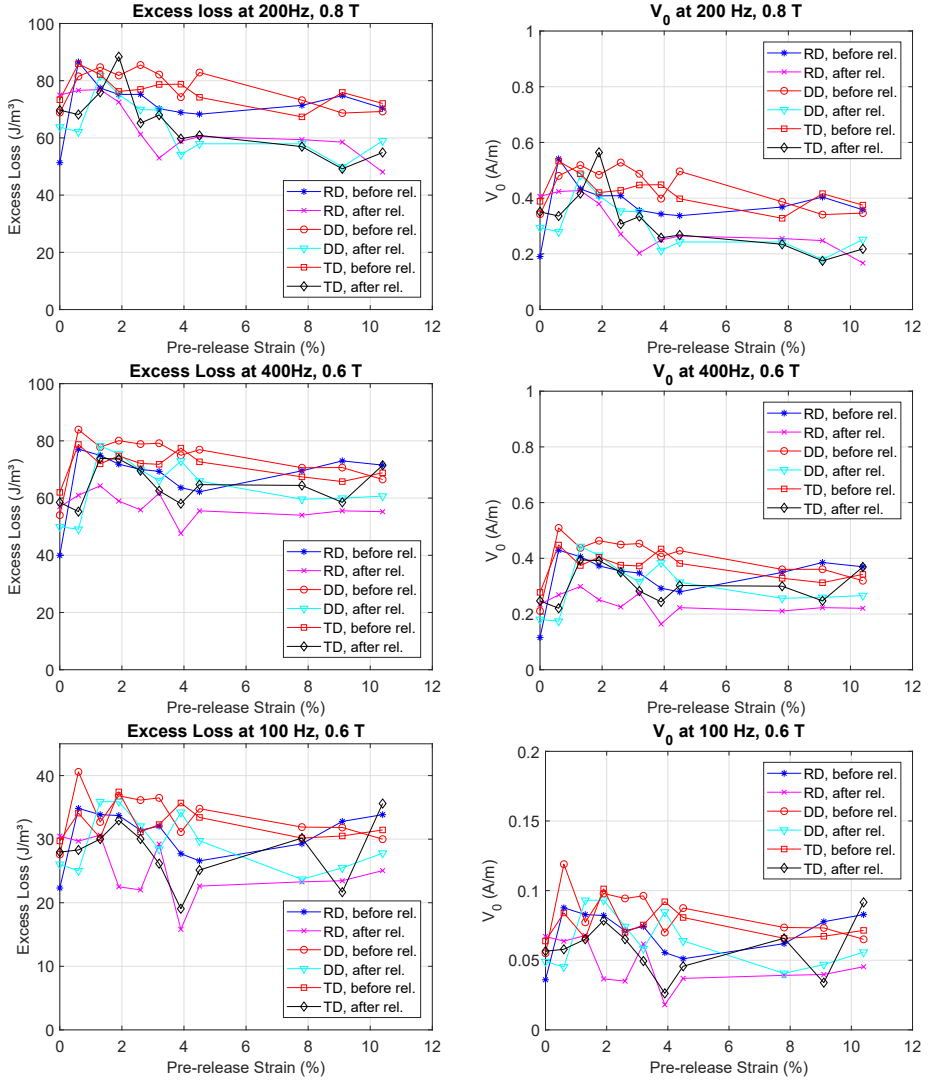


Figure 5.11: Excess energy losses at several excitation levels, both before and after the release. On the right, the correspondingly calculated V_0 parameter is shown.

5.3.4 Effect of increasing strain on electrical resistivity

The increase in total core losses due to the straining of electrical steel was found to be largely caused by the increase in hysteresis losses. In the core loss analysis that has lead to this conclusion, it was assumed that the electrical resistivity of the sample did not change when the sample was strained.

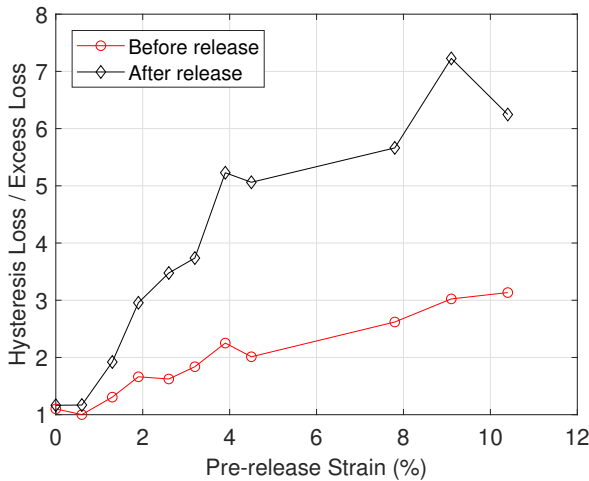


Figure 5.12: Ratio between the hysteresis loss component and excess loss component in M270-35A at several levels of pre-release strain both before and after release of the load. Data valid for magnetic excitation at 200 Hz and peak flux density 0.8 T.

Therefore, it could be assumed that the classical loss component remained unaffected by the strain. This assumption is now verified by measuring the electrical resistance of the strained samples after release. If the total core losses increase due to a decrease in resistivity, it should be possible to confirm this change on unloaded samples by accurately measuring the resistance. In Fig. 5.13, the setup is shown which was used for this experiment. The electrical resistance of 6 samples with increasing levels of elongation up to 6.2% was measured by means of placing the probes on the sample with a constant distance between them. Each measurement was repeated 6 times in order to verify the repeatability. The average values and corresponding error bars are plotted in 5.14. It is clear that the measured resistance did not noticeably change after the steel was strained. Based on these experimental data, it can be concluded that the assumption is valid.

5.3.5 Microstructural changes in strained electrical steel

It was established in the previous section that the degradation of magnetic properties after straining of electrical steel can, at least for the largest part, be attributed to the increase in hysteresis losses. In this section, the microstructure of M270-35A steel is investigated using Transmission Electron Microscopy (TEM) after increasing levels of strain in the plastic region. This was done in collaboration with the UGhent Metallurgic Lab. Using TEM, the



Figure 5.13: Setup and equipment for resistivity measurements using an RLC-meter and 4-wire method.

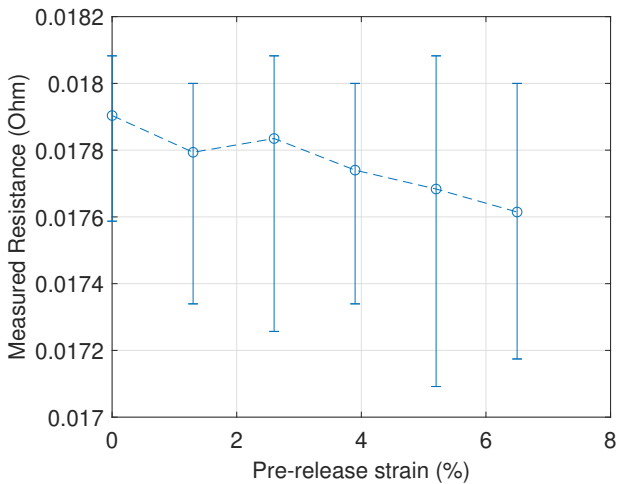


Figure 5.14: Measured electrical resistance of electrical steel samples after being subjected to increasing levels plastic strain.

dislocation density in the microstructure of the samples (after load release) can be measured. In Figure 5.15, micrographs obtained using the TEM are shown for three samples. From these micrographs, the dislocation density was calculated and plotted in Figure 5.16. For each sample, several images were captured. The calculation was repeated several times for each sample. The average calculated dislocation density is used for the plot line and the error bars were constructed correspondingly. At 10.4% strain, the variability of the calculations was higher due to the presence of entangled dislocations. From these

data, it was confirmed that the dislocation density rises sharply due to plastic deformation. In the unstressed sample, the average dislocation density is $3.2 \times 10^{13}/\text{m}^2$. The samples that were plastically strained to 5.1% and 10.4% had an average dislocation density of $5.2 \times 10^{13}/\text{m}^2$ and $1.31 \times 10^{14}/\text{m}^2$, respectively. The observed increase in dislocation density influences the magnetic properties because the dislocations become entangled, forming stronger pinning sites which impede domain wall motion [19]. This impeded motion causes a degradation of the magnetic properties. Also in [19], the Jiles-Atherton hysteresis model is used to highlight the relation between several microstructural parameters and the magnetic hysteresis properties. In this model, parameter k_j is proportional to the coercive field and the hysteresis loss component and parameter a_j is inversely proportional to the relative permeability. Both of these parameters are proportional to the square root of dislocation density, which is in correspondence with the measurements reported in this thesis.

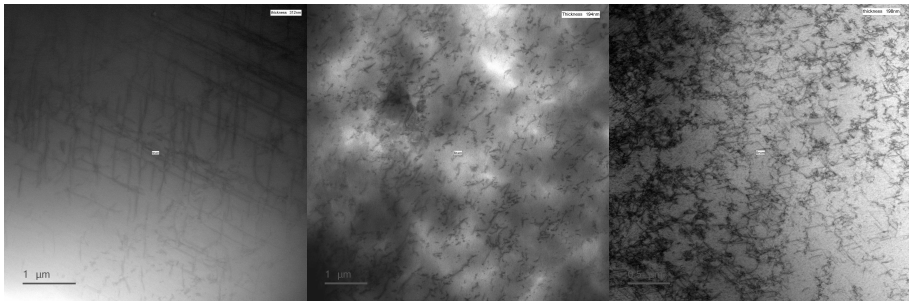


Figure 5.15: Micrographs obtained using TEM for three samples of M270-35A silicon steel. (Left) unstrained sample. (Middle) Sample strained to 4.5% and afterwards released. (Right) Sample strained to 10.4% and afterwards released.

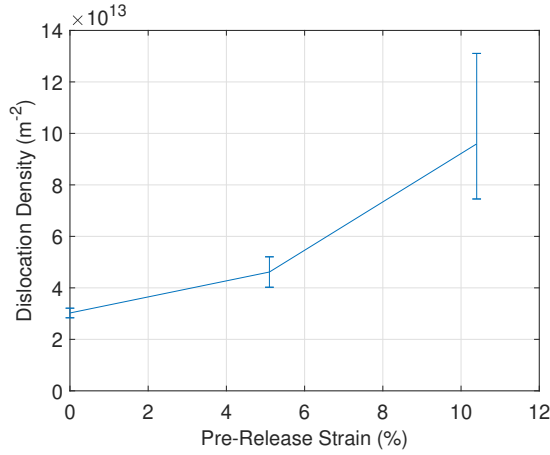


Figure 5.16: Dislocation density as a function of pre-release strain.

5.3.6 Discussion

The material state near cutting edges and other local plastic deformed areas of ferromagnetic cores is investigated using a magnetomechanical setup. When the material is plastically strained, the BH curve is affected and the magnetic permeability is significantly degraded. At 10.4% strain, the permeability has decreased by 88% with respect to the unloaded state for the RD sample. An even further degradation was observed when the plastically deforming mechanical load was released. After load release the permeability has decreased by 94% with respect to the stress-free state. This ‘released’ load state corresponds more closely to the material state near cutting edges of electrical steel sheets. The total core losses were measured and it was found that the plastic deformation significantly increases the core losses, similar to the magnetic degradation observed in the BH curves. Core loss analysis has shown that the large increase in core energy losses is mainly caused by a sharp increase of the hysteresis loss component. At 10.4% strain, the hysteresis loss component has increased by 55% with respect to the unloaded state for the RD sample. After mechanical load release, the hysteresis loss component has increased further by 98% with respect to the stress-free state. Both the classical and excess loss component showed no clear changes under increasing deformation. Within the measured range, the electrical resistivity remains unaffected by the sample deformation. The effect of plastic deformation on the magnetic properties is similar for samples cut in different directions. As expected, TEM measurements on unloaded deformed samples have shown a sharp increase in dislocation density due to deformation. At 10.4% strain, the dislocation density has increased approximately 330% with respect to the

unloaded state. The effect of plastic strain on the hysteresis loss component and the dislocation density shows a positive correlation. The results show that the magnetic properties of electrical steels are significantly degraded when plastically strained and afterwards released. This highlights the importance of using material models which incorporate the effects of residual stress when developing accurate electrical machine models.

5.4. Uni-axial measurements and analysis on M270-35A in elastic tensile region

In the previous section, it was shown how the hysteresis losses increase with increasing plastic strain, and that these losses increase even further when the load is released. On the contrary, the excess losses initially increase, but show a slight decrease with increasing strain. After release, the excess losses behave oppositely to the hysteresis losses. In this section, the magnetic behaviour of M270-35A steel is investigated while under stress in the elastic region. The goal is to demonstrate that this specific steel grade has magnetic properties which are affected by elastic stress in a similar way as other grades reported in literature. Therefore, these results could indicate that any type of NO steel also behaves differently under plastic strain.

5.4.1 Experimental setup and methodology

The same modified SST setup described in the previous section was used for this experiment. One set of M270-35A strips, cut in RD, was manufactured. The core losses were measured at several frequencies (16, 64, 144, 256, 400 Hz) and B_p levels (0.2, 0.4, 0.6, 0.8, 1, 1.2, 1.4 T).

5.4.2 Measurement Data and analysis

In Fig. 5.17, BH curves are shown when the sample was placed under various levels of uni-axial elastic stress. It appears that for low values of stress, the magnetic field strength for obtaining a certain flux density decreases. For high values of elastic stress, this effect is reversed. At 1 T B_p , the magnetic field strength is 181 A/m. When this sample is subjected under 20 MPa of stress, this value decreased to 124 A/m. At 100 MPa, 318 A/m is required. An increase of stress towards the material's yield strength further increases the required magnetic field, thus degrades the magnetic properties. In Fig. 5.18, the relative permeability is plotted against the applied static stress for various levels of B_p . A consistent trend appears for each plotted curve, a trend

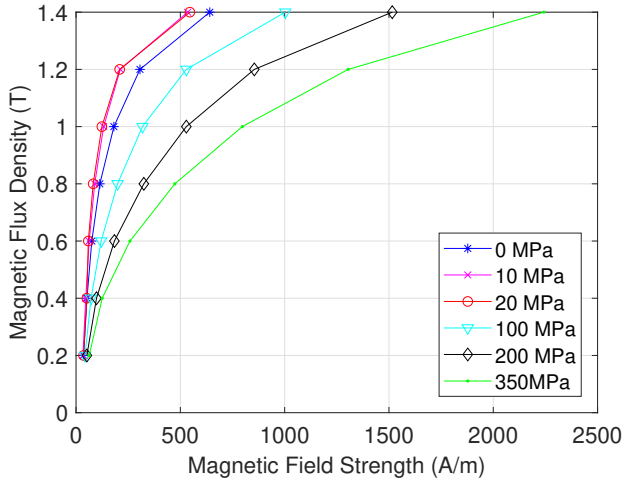


Figure 5.17: Measured BH curves of M270-35A under various levels of static elastic stress.

which is confirmed in the normalized plots on the right hand side of this figure. The relative permeability peaks between 10 and 20 MPa of stress. Further increasing stress decreases the permeability.

The influence of elastic tensile stress on the loss components was investigated using a separation of losses analysis. In Fig. 5.19, the hysteresis losses are plotted under increasing levels of uni-axial tensile stress at several peak flux density levels. An initial sharp decrease of losses is followed by a slow increase for increasing stress. A minimum is reached on average at 55 MPa. The hysteresis loss evolution show a similar trend for each B_p -level. Therefore, an additional plot with normalized data is shown in Fig. 5.20. From this plot it can be confirmed that the hysteresis loss component is minimized at approximately 50 MPa tensile stress. The yield strength of M270-35A steel as found in datasheets is 450 MPa, which implies that the minimum loss value is obtained at roughly 10% of the material yield strength. On average over the plotted data, the minimum hysteresis loss value is 59% of the initial unloaded value. After this minimum, a rising tensile stress increases the losses. This rate of increase appears to be inversely related to the peak flux density value. At 350 MPa, the hysteresis losses are approximately equal to the unloaded stress state for $B_p = 0.6$ T, while the hysteresis losses are still only 72% of the initial unloaded value for $B_p = 1.4$ T.

Similarly, the excess loss component is separated from the total measured losses in order to study the effect of elastic tensile stress. Several results are shown in Fig. 5.21 for a constant frequency of 144 Hz and a constant B_p of 1 T. A plot with normalized data is added in Fig. 5.22. It appears that the excess

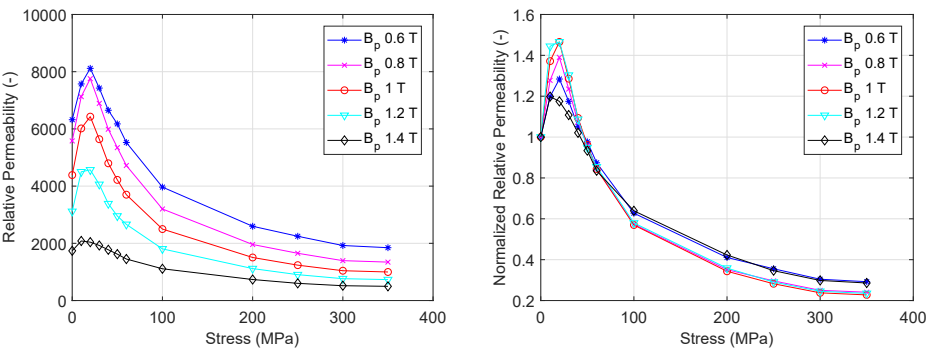


Figure 5.18: Evolution of the relative permeability (left) and normalized relative permeability (right) of M270-35A electrical steel under increasing static stress in the elastic region for different levels of peak flux density.

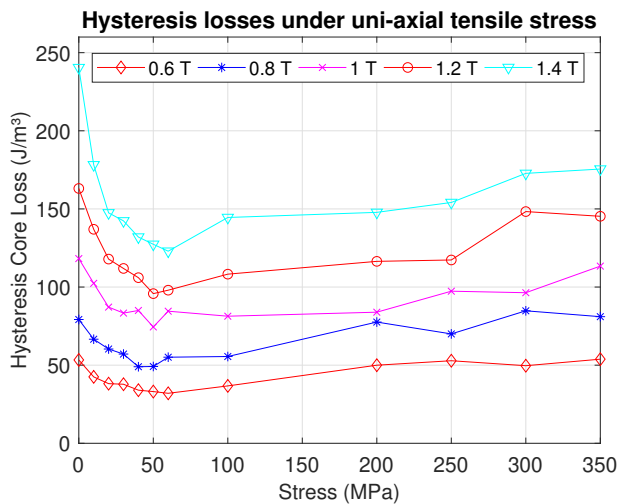


Figure 5.19: Hysteresis loss component of M270-35A electrical steel under increasing uni-axial tensile stress for different levels of peak flux density.

loss component shows a trend which is similar to the hysteresis loss component under increasing elastic tensile stress. However, the minimum in excess losses is obtained at a slightly lower stress level of approximately 30 MPa (or 7% of the material yield strength). The minimum value of excess losses (on average over the plotted results) is 77% of the initial unloaded value. A further rising tensile stress will increase the excess losses in a similar way as it did for the hysteresis loss component.

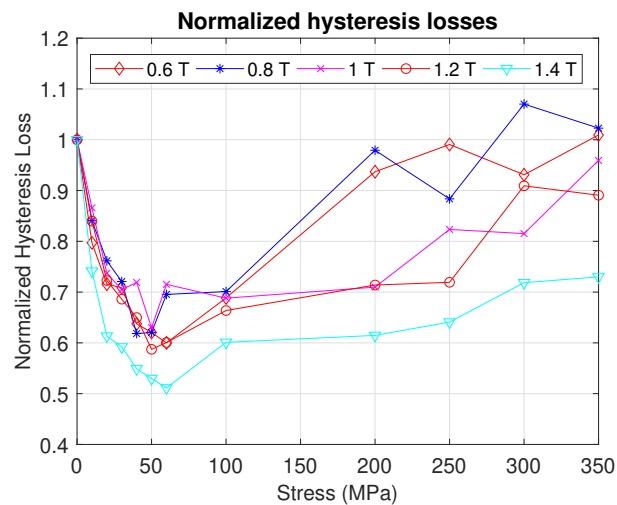


Figure 5.20: Normalized hysteresis loss component of M270-35A electrical steel under increasing uni-axial tensile stress for different levels of peak flux density. The losses are normalized with respect to the unloaded state.

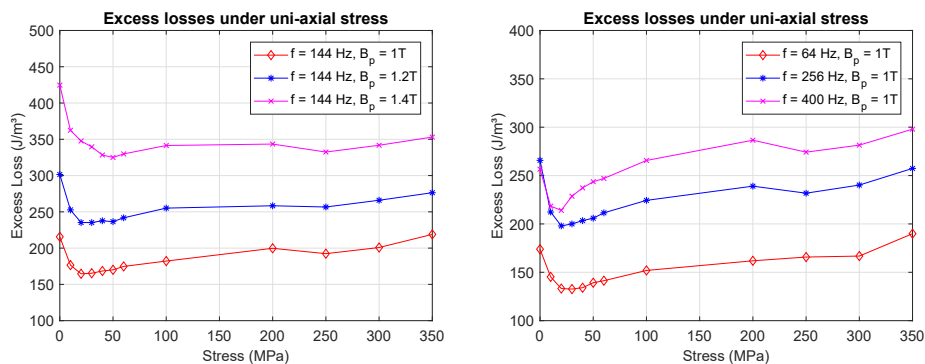


Figure 5.21: Excess loss component of M270-35A electrical steel under increasing uni-axial tensile stress for constant frequency (left) and constant peak flux density (right).

5.5. Uni-axial measurements and analysis on M270-35A in elastic compressive region

In realistic applications, the load which is applied to the ferromagnetic core is not always tensile. In some cases, the core of an electric motor is placed inside the housing by means of shrink fitting, which causes the housing to exert a compressive stress on the outer edge of the yoke. The impact of uni-axial

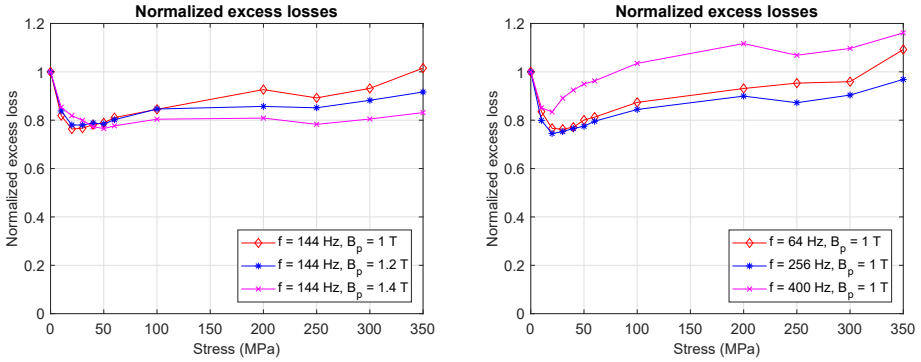


Figure 5.22: Normalized excess loss component of M270-35A electrical steel under increasing uni-axial tensile stress for constant frequency (left) and constant peak flux density (right).

compressive stress on magnetic properties of electrical steel has been reported frequently in literature. However, the results strongly depend on many microstructural features such as grain size, texture, impurities such as carbon and nitrogen, dislocation density or residual stresses [52]. In order to have a complete dataset of the effect of stress on M270-35A, it is important to measure the effects of compressive elastic stress on the magnetic properties of M270-35A. The same magnetomechanical setup as described earlier (Fig. 5.1) is used for applying the compressive load. However, due to the small thickness of the sample, even a small compressive force can result in the buckling or bending of the sample. In order to avoid this, a reinforcement piece was manufactured that encloses and supports the sample. This allowed the compressive stress to be increased up to 30 MPa without distorting the measurements. The core losses were measured at 4 different excitation frequencies (16, 64, 144, 256 Hz) and 6 levels of peak flux density from 0.2 T up to 1.2 T. Due to the significant degradation of the magnetic properties, it proved increasingly difficult to obtain a higher peak flux density. In Fig. 5.23, the measured single-valued BH curves are displayed under increasing compressive stress. The large impact of even a small compressive stress indicates that the magnetic material properties are highly sensitive to mechanical compression of the steel. These BH curves are then used for calculating the relative permeability for each value of B_p , and plotted in Fig. 5.24. From the normalized values of the relative permeability, it appears that the effect of compressive stress is not constant but varies with the value of B_p . The permeability decreases exponentially and is reduced to 50 % for all measured values after only 15 MPa of compressive stress. A similar drastic effect is observed when plotting the measured core losses. In Fig. 5.25, it is depicted how the compressive stress increases the total core

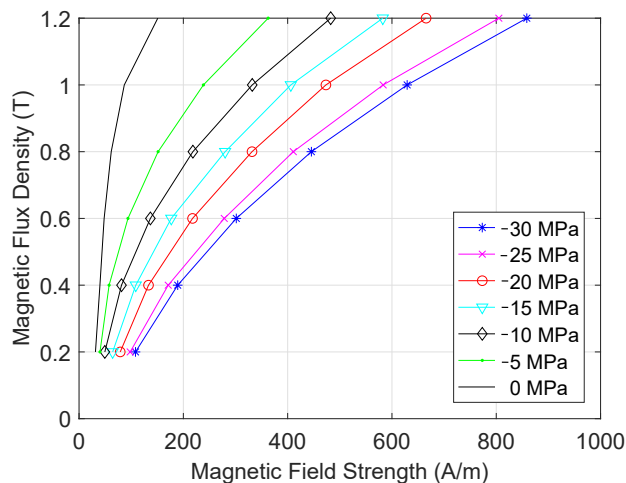


Figure 5.23: *BH* curves measured on M270-35A electrical steel at increasing levels of compressive uni-axial stress.

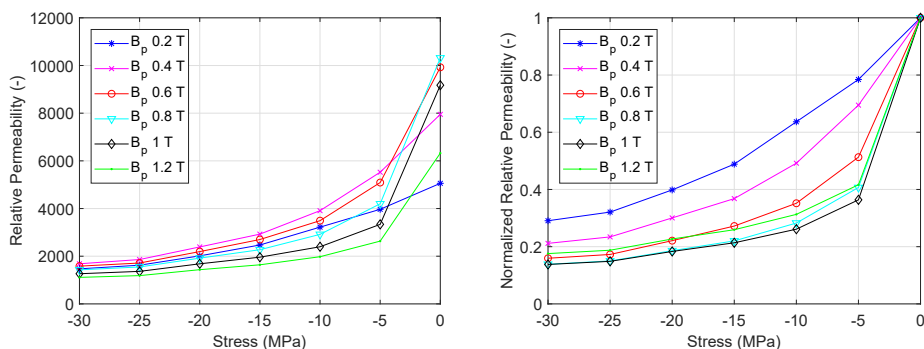


Figure 5.24: The impact of compressive stress on the relative permeability of M270-35A electrical steel in absolute values (left) and normalized valued (right). The normalized values are calculated in reference to the unloaded, stress-free case.

losses. The trend which can be observed is similar for various frequencies and peak flux densities. Further analysis of the core losses is needed to explain the causes of this phenomenon. In Fig. 5.26, the hysteresis losses are depicted as absolute and normalized values. The core losses dramatically increase for moderate levels of compressive stress, and the effect appears to depend on the level of peak flux density. When considering the excess losses, a similar trend is observed (Fig. 5.27). The high sensitivity to compression in the uni-

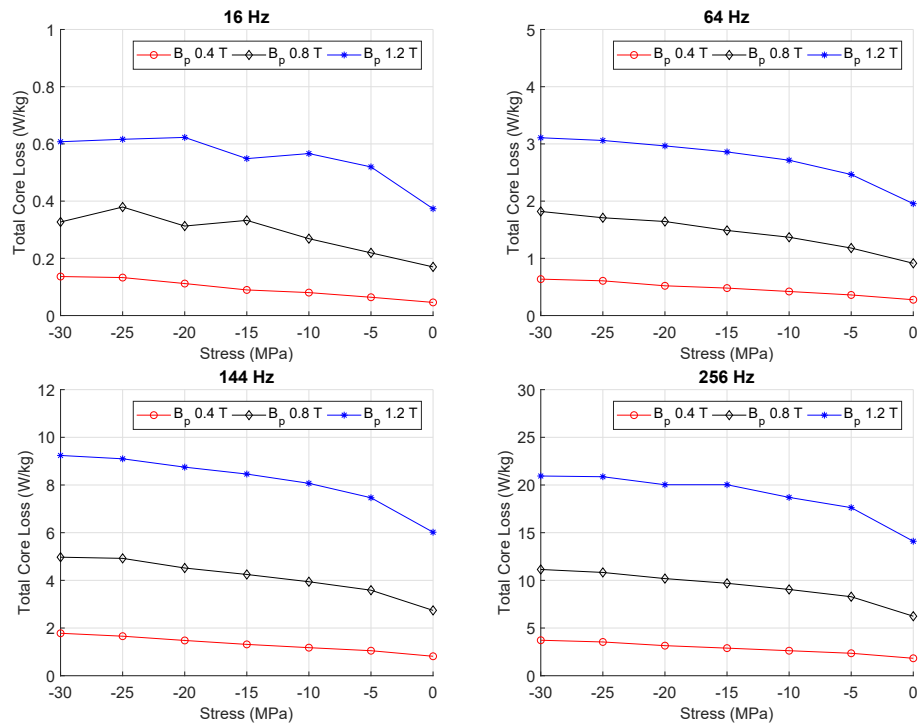


Figure 5.25: Total measured core losses obtained at various levels of elastic compressive stress on M270-35A electrical steel.

axial direction is similar for both the excess loss component and the hysteresis loss component of M270-35A electrical steel. This similarity was also observed in the elastic tensile region, as described in the previous section. Also, the measured relation between magnetic properties and compressive stress is in close agreement with results found in literature. With the magnetomechanical measurement data obtained in the compressive elastic region, the tensile elastic region and the tensile plastic region, it is possible to construct a uni-axial magnetomechanical model over a broad range of stresses. This model will be further described in the next chapter, where it will be used for incorporating the effects of stress on manufacturing effect models.

5.6. Effect of stacking stress on core losses of M100-23P

In this section, an experiment is described where the influence of stacking pressure on the magnetic properties is investigated using a simplified prototype setup. As described in literature, similar experiments have found that the

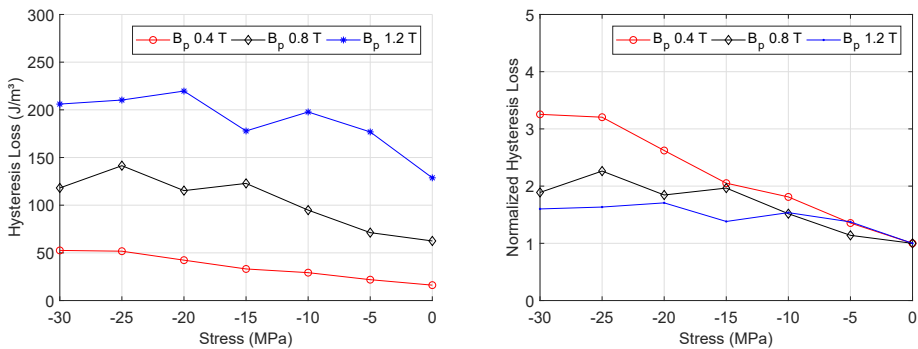


Figure 5.26: Effect of elastic compressive stress on the hysteresis losses of M270-35A electrical steel.

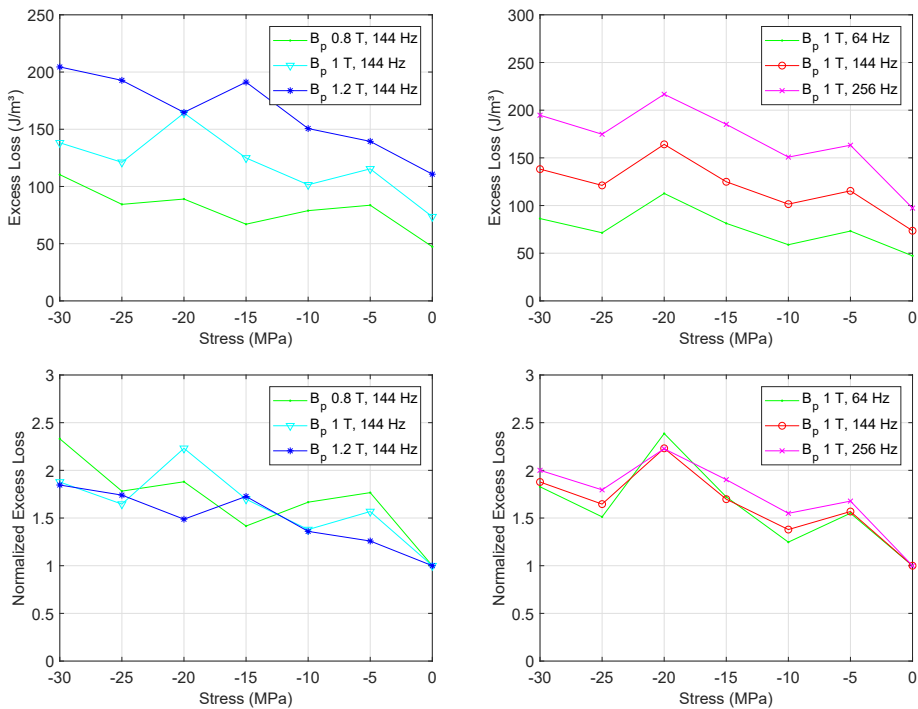


Figure 5.27: Effect of elastic compressive stress on the hysteresis losses of M270-35A electrical steel. The large local peak in excess loss at 1 T and -20 MPa might be a consequence of a systematic measurement error.

influence of increasing axial stress was detrimental to the magnetic properties of the stack. It was suggested that one reason for this degradation might be the additional eddy current circuits which are formed through the cutting edge of the laminations. In this experiment, the effect of cutting edge degradation and axial stress is investigated by means of three sets of samples. Each set was cut in RD from M100-23P electrical steel. The first set was cut using water jetting, the second was cut with a laser cutter, and the last set was cut using a punching tool. Due to the different nature of these cutting techniques, the hypothesis is that core losses of the stack might be influenced by the interaction between the chosen cutting technique and the subsequent application of axial compressive stress.

5.6.1 Experimental setup and methodology

Core loss measurements were obtained at 16, 64, 144, 256 and 400 Hz for induction levels of 0.2, 0.4, 0.6, 0.8, 1, 1.2 and 1.4 T. A novel setup is used for measuring the effect of compressive stacking stress in the axial direction of the machine. The design is based on the standard SST, which is modified to accommodate a compressive force on a stack of sheets. The applied force is generated by rotating screws mounted on a threaded axis and guided onto the stack through a mechanical yoke (Fig. 5.28). In this setup, the axial pressure is applied on a specific part of the stack. Consequently, only a small portion of the entire magnetic circuit is affected by the compressive stress. This small portion corresponds to the 'Stressed length' in Fig. 5.29. However, the measurements are valid for the entire magnetic circuit. In order to determine the magnetic properties of the stack under compressive stress, the magnetic path in the modified SST should be considered as an equivalent circuit with one reluctance representing the stressed material.

5.6.2 Measurement Data and analysis

In this setup, sheets of electrical steel are compressed in the direction of the lamination thickness. Consequently, the electrical contact near the cutting edge might be influenced by this compressive stress. An improved electrical contact can lead to additional eddy currents through the short circuits on the cutting edge. Therefore, in the core loss analysis, the classical loss component cannot be assumed constant for increasing levels of compressive stress. Hence, a different loss separation technique is necessary. In Fig. 5.30, measured core losses are shown for three sets of stacks.

The measured core losses are separated using the modified SLT core loss model, with each loss coefficient formulated as a function of the compressive mechanical stress in the axial direction.

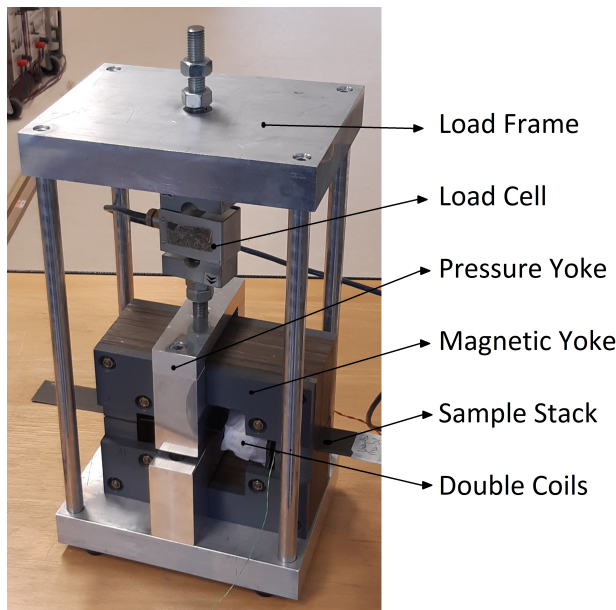


Figure 5.28: Modified SST setup for measuring the effect of axial compressive stress on the magnetic properties of stacked sheets of electrical steel.

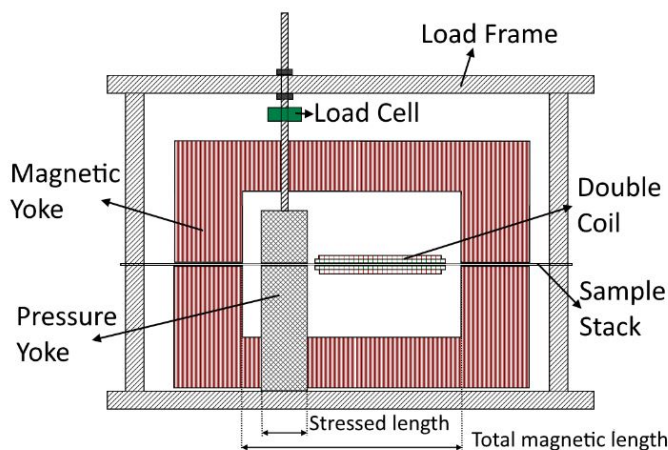


Figure 5.29: Side view of modified SST setup drawing with highlighted magnetic lengths.

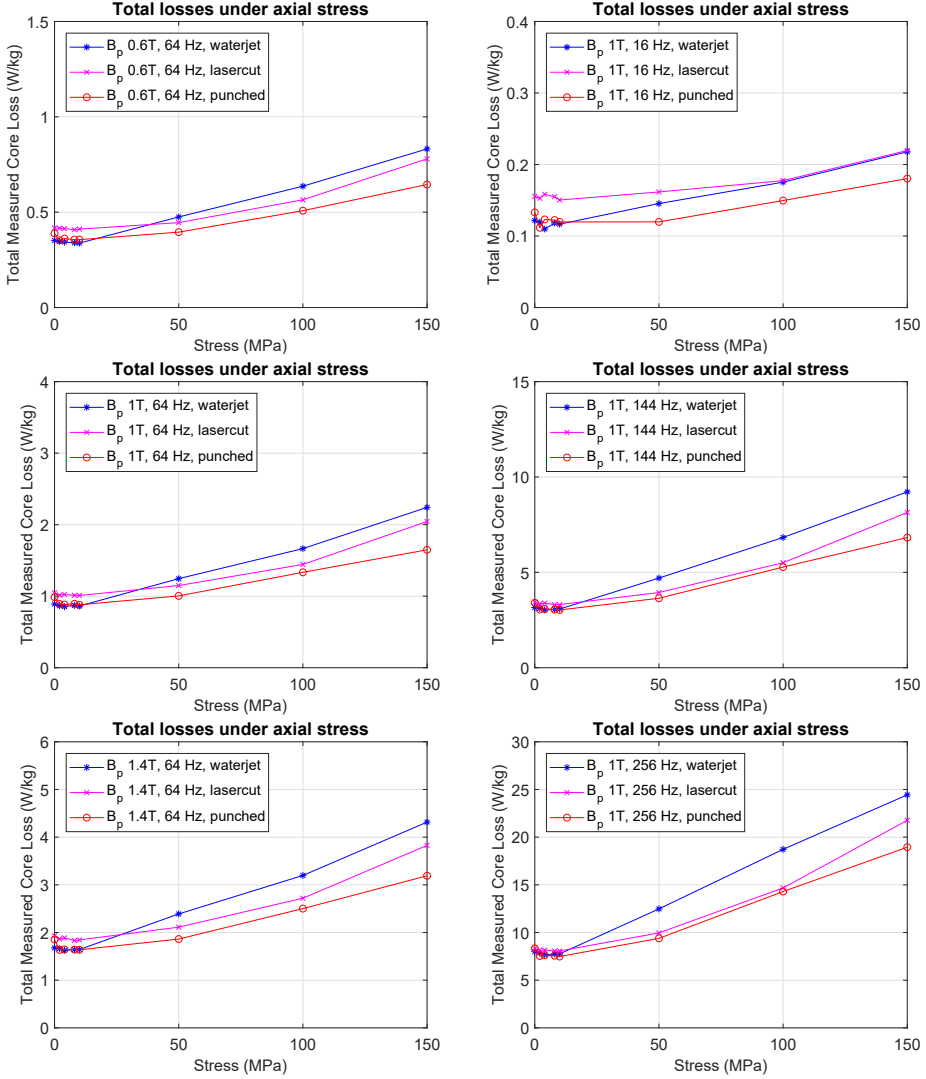


Figure 5.30: Measured losses on modified axial stress SST for three sets of sample. The effect of axial stress under constant excitation frequency (left) and peak flux density (right) is shown.

$$P_{tot} = C_h(\sigma_{ax})B_p^2 f + C_{cl}(\sigma_{ax})B_p^2 f^2 + C_{ex}(\sigma_{ax})B_p^{1.5} f^{1.5} \quad (5.9)$$

In order to identify the three loss coefficients, the previously used standard loss separation technique is inapplicable. Instead, an inverse optimization al-

gorithm can be utilized where the modelled and measured losses are iteratively compared and the coefficients are correspondingly updated until the model simulations fit accurately with the measurement data. This algorithm was produced using two MATLAB toolboxes. First, a genetic algorithm is used to find a global minimum and secondly the solution is refined with the *fmincon* constrained optimization algorithm. This sequence of algorithms was repeated several times to test the sensitivity of the solution to the measurement errors.

The results of this inverse problem formulation for loss analysis are shown in Fig. 5.31. From the analysis, it appears that the axial compressive stress drastically impacts the classical losses. At 150 MPa, the classical core losses have almost tripled for all three cutting techniques. Meanwhile, the impact of axial compression on the hysteresis or excess loss component is much less compelling. From this analysis, it can be concluded that the increase in core losses observed after applying a large compressive stress can mainly be attributed to the increase in classical losses. This might be enabled by the improved electrical contact and consequent interlaminar short circuits when the laminations are placed under large axial mechanical pressure. However, as a topic of further research, this experiment could be repeated with only one lamination where the possibility of interlaminar short circuits is removed.

5.7. Conclusion

The main focus of this chapter is on the impact of mechanical stress on the magnetic properties in electrical steels. The relation between uni-axial stress on M270-35A was studied in several stress states (tensile, compressive, elastic and plastic) using a modified SST setup. In several static stress states, the magnetic permeability and core losses were measured and afterwards analysed using core loss separation. It was shown that the magnetic permeability, hysteresis loss component and excess loss component are strongly influenced by the mechanical stress state. It was verified experimentally that the classical loss component remains unaffected by plastic strain.

Under compressive stress up to - 30 MPa, the relative permeability decreases while the hysteresis and excess losses increase up to 3 times depending on the peak magnetic flux density and excitation frequency.

Under elastic tensile stress, the permeability initially peaks at 1.4 time the unloaded permeability at approximately 30 MPa. At this relatively low tensile stress state, both the excess and hysteresis loss component reach a minimum value. With increasing tensile stress, the permeability gradually decreases and the core losses increase.

When the stress is increased above the yield strength up to plastic deformation, the magnetic properties degrade rapidly. It was found that the magnetic

properties vary significantly under a deforming mechanical stress before and after the load is released. When a mechanical load plastically deforms electrical steel, the magnetic properties are more favourable before the load release than after (i.e. the magnetic permeability is higher and the core losses are lower before the release than after). This effect might be particularly interesting for researchers studying manufacturing effects because the material state near the cutting edge of a lamination is in a plastically deformed and unloaded state. To investigate the observed magnetic properties after straining further, the samples were placed in a TEM to measure their dislocation density. It was found that the effect of plastic strain on the hysteresis loss component and the dislocation density shows a positive correlation.

Lastly, the impact of compressive stress in the thickness direction (or axial stress) was measured on M100-23P steel. This was done using a modified SST which allowed a controlled mechanical load to be exerted on a stack of strips. The impact of stacking stress was measured for 3 sets of strips. One set was cut using a water jet, the second set was cut using laser cutting and the third set was cut using traditional punching. Core loss measurements were performed at several levels of peak flux density and excitation field frequency. The obtained loss data was used for fitting a modified loss model in which each loss coefficient was dependent on the applied compressive stress. From this analysis, it was found that the classical loss component showed a strong relation with the applied axial compressive stress, increasing up to 300 % at 150 MPa for the waterjet cut samples. Meanwhile, the excess and hysteresis loss component did not show any significant change under increasing axial compressive stress.

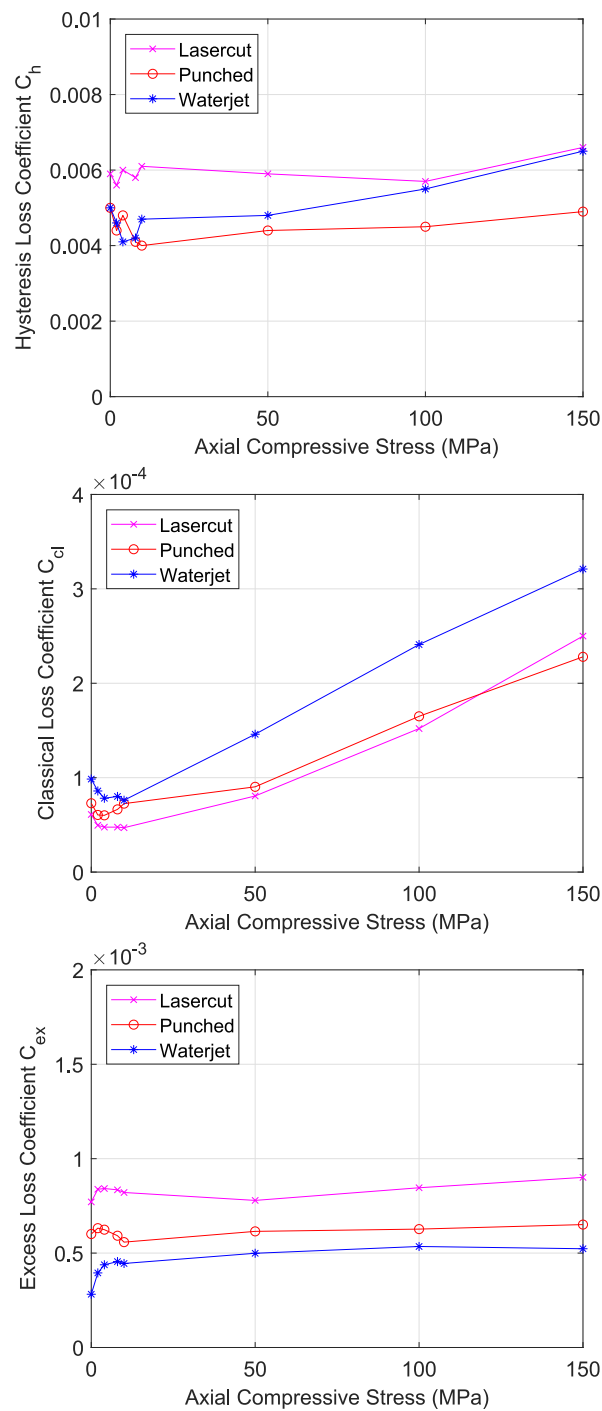


Figure 5.31: Result of core loss analysis displaying the effect of axial compressive stress on each core loss component.

6

Application of Stress in Manufacturing Effect Models

In this chapter, it is discussed how the known relation between magnetic properties and stress (i.e. the magnetomechanical properties of electrical steel) can be utilized to shape an improved machine model which incorporates manufacturing effects. As mentioned in the first chapter, machine designers usually don't consider the negative effects of the manufacturing process and instead implement a machine building factor to account for any discrepancy between the predicted and actual machine performance. It can be argued that this discrepancy is caused by a lack of information provided by the steel supplier on the one side, and by the core manufacturer on the other. In the previous chapter, it has been demonstrated that mechanical stress has a strong influence on the magnetic properties of steel. However, electrical steel suppliers typically only provide data which is obtained using standardized (often Epstein frame) measurements. On the other hand, companies processing the magnetic cores typically provide no details on the stress distributions which their several techniques introduce into the steel. However, it has been demonstrated by metallurgists in literature that the impact of cutting or joining can be measured using techniques such as, among others, nano-indentation or X-Ray diffraction. These techniques quantify the amount and distribution of residual me-

chanical stress which is introduced after each specific process. A closer collaboration between steel suppliers and lamination manufacturers might provide some insight into the black box that currently is the building factor. In this chapter, an approach is presented to link the magnetomechanical effect to the effects of manufacturing on the ferromagnetic core. This approach uses some geometrical simplifications and assumptions in order to make the model practicable.

It should be noted that some difficulties occur in linking the magnetomechanical model (which captures the effect of mechanical stress on the magnetic properties) to the manufacturing model (which divides the lamination geometry into distinct areas that are affected by the residual stress caused by production techniques). For example, due to the complexity of residual stresses, it isn't obvious what the directionality of the stress in the sample is. The results published in [33], for example, show the local value of residual stress near welding seams in structures of stacked steel plates. What is known from Chapter 5 is that the angle between the applied stress and the direction of the magnetic measurements is of great importance to the conclusion. Also, it is important to know if the plastically deformed region (e.g. near cutting edges) is in a loaded or unloaded state. Lastly, it should be noted that because the known stress characteristics are valid in one sample, the effect of interlaminar eddy currents is not accounted for in the basic magnetomechanical model. Therefore, additional modifications need to be made to the standard manufacturing effect models.

Nevertheless, a more accurate and intuitive model of a fully manufactured electrical machine can be built when stress characteristics are available. To demonstrate this, the effects of stress are included in the joining manufacturing models using stress-dependent MEC models and an inverse problem approach. This chapter can be considered as an initial attempt towards a more realistic model of stress based manufacturing models. In 6.1, the magnetomechanical model is described. In 6.2, a step by step guide is given to parametrize the model for any type of electrical steel grade. Finally, the magnetomechanical model is incorporated into a MEC manufacturing effect model for welding and interlocking, respectively in 6.3 and 6.4.

6.1. Magnetomechanical model

Based on the measurement results from the previous chapter, it is possible to parametrize a magnetomechanical model. These measurements have shown that the relative permeability, hysteresis and excess loss component are all strongly influenced by mechanical stress. In the magnetomechanical model, this effect can be accounted for using coarse-scale correction factors. The correction factors are modelled using a piecewise function approximation of the

normalized measurement data. From these data, it appeared that the correction factors depend on the peak magnetic flux density. In Fig. 6.1, the correction factor for the relative permeability is plotted over a wide range of mechanical stress. These data are valid for M270-35A grade steel. The correction factor for the relative permeability K_μ is described in (6.1) using a piece-wise interpolation function of the mechanical stress σ . K_μ is defined by a set of 10 B_p -dependent parameters, namely α_1 to α_{10} . In the plastic region (i.e. $\sigma > \sigma_e$), the correction factor depends on different α -parameters according to the mechanical stress state (stressed or released).

A similar approach can be used for defining correction factors for the excess loss component and hysteresis loss component. In (6.2), a general expression is given of these correction factors using 9 parameters, namely β_1 to β_9 . For K_{hyst} , the parameters depend only on B_p while K_{exc} depends both on B_p and the magnetic field excitation frequency f . The function limits σ_1 , σ_2 and σ_e are also material dependent. The correction factors for the hysteresis loss component and the excess loss component have been plotted for M270-35A steel in figures 6.2 and 6.3, respectively. The correction factor curves show discontinuities around the yield strength. Similar to the results reported in [39], determining accurate magnetic material properties when stressing the material to yield strength is difficult from a technical viewpoint. Magnetic measurements obtained in the elastic region between 350 MPa and 450 MPa were highly unrepeatable and were therefore not used for modelling the linear function approximation for this stress region. A lack of accurate magnetic measurements around the yield strength also leads to inaccuracies at this stress state. The observed discontinuity might be explained by the hard limit border between the elastic and plastic region in the magnetomechanical model, while in reality the transition between elastic and plastic stress might occur more gradually.

$$K_\mu(\sigma, B_p) = \begin{cases} 1 - \left(\frac{\sigma}{(\alpha_1 + \alpha_2 \sigma)} \right) & \sigma \leq 0 \\ \alpha_3 \sigma^2 + \alpha_4 \sigma + 1 & 0 < \sigma < \sigma_1 \\ \alpha_5 \sigma^{\alpha_6} & \sigma_1 < \sigma < \sigma_e \\ \alpha_7 \sigma + \alpha_8 & \sigma > \sigma_{e, stressed} \\ \alpha_9 \sigma + \alpha_{10} & \sigma > \sigma_{e, released} \end{cases} \quad (6.1)$$

$$K_{hyst, exc}(\sigma) = \begin{cases} \beta_1 \sigma + 1 & \sigma \leq 0 \\ \beta_2 \sigma^2 + \beta_3 \sigma + 1 & 0 < \sigma \leq \sigma_2 \\ \beta_4 \sigma + \beta_5 & \sigma_2 < \sigma \leq \sigma_e \\ \beta_6 \sigma + \beta_7 & \sigma > \sigma_{e, stressed} \\ \beta_8 \sigma + \beta_9 & \sigma > \sigma_{e, released} \end{cases} \quad (6.2)$$

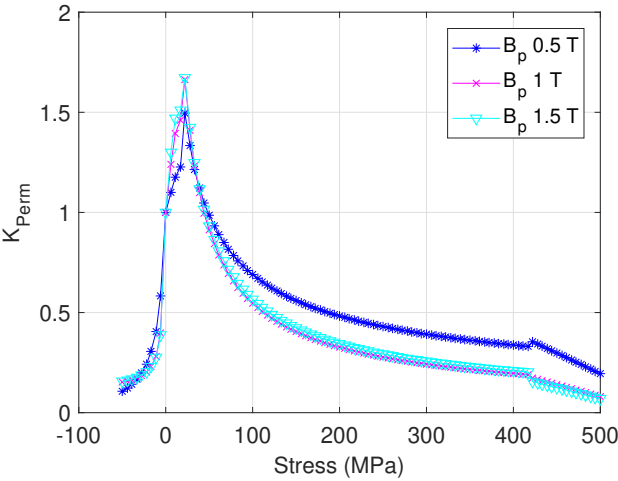


Figure 6.1: Correction factor curves for the relative magnetic permeability in M270-35A grade electrical steel at 50 Hz. Data in plastic region (Stress > 450 MPa) are valid under mechanical load before release.

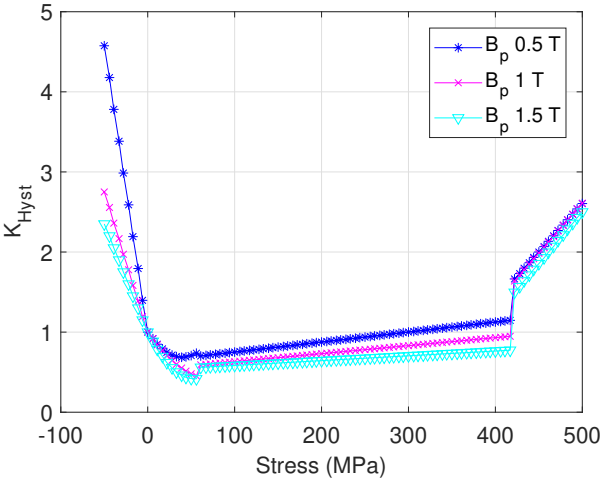


Figure 6.2: Correction factor curves for the hysteresis loss component at 50 Hz in M270-35A grade electrical steel. Data in plastic region (Stress > 450 MPa) are valid under mechanical load before release.

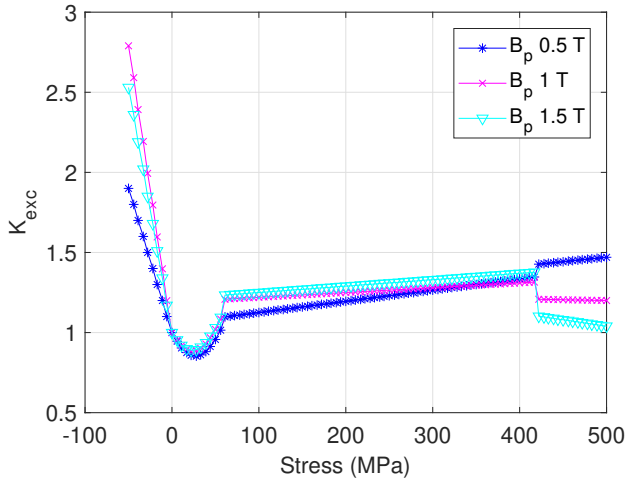


Figure 6.3: Correction factor curves for the excess loss component in M270-35A grade electrical steel at 50 Hz. Data in plastic region (Stress > 450 MPa) are valid under mechanical load before release.

6.2. Guidelines for Building the Magnetomechanical Model

In this section, a step-by-step guide is presented on how to fit a new material to the magnetomechanical model. With the necessary measurement equipment available, developing a full characterization of the magnetic material properties under uni-axial mechanical stress is possible for any grade of electrical steel. A corresponding flowchart is shown in Fig. 6.4.

1. Manufacture Epstein strips of the material under investigation
2. Place the strips in the setup for magnetomechanical measurements
3. Measure the magnetic permeability and core losses under sinusoidal B -waveform for all permutations of the following magnetomechanical states:
 - a sufficient number of frequencies between 10 and 400 Hz
 - Peak flux density levels 0.2, 0.4, 0.6, 0.8, 1, 1.2, 1.4, 1.6 T
 - Elastic uni-axial static mechanical stress from -50 MPa (compressive) to the material elastic limit (tensile) with intervals of 10 MPa.
 - Plastic uni-axial static mechanical stress before and after release from 2 % strain up to material fracture with intervals of 2 % strain
4. Perform loss separation on core loss measurements [11]
5. Normalize the measured permeability, hysteresis losses and excess losses with respect to the unaffected stress state (0 MPa)
6. Fit the normalized data to the piecewise interpolation model described in (6.1) and (6.2). For the correction factors for magnetic permeability and hys-

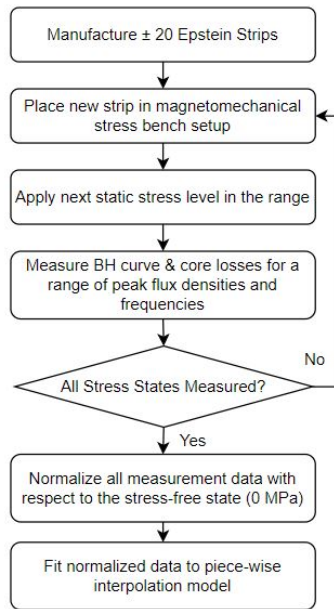


Figure 6.4: Flowchart describing the necessary steps to parametrize the magnetomechanical model for any grade of electrical steel.

teresis losses, the α and β - coefficients are a function of peak flux density. For the correction factor of the excess loss, α and β - coefficients are both a function of peak flux density and frequency.

The process of core loss separation is essential due to the different relation between mechanical stress and the hysteresis and excess loss component. Additionally, the classical loss component is insensitive to mechanical stress, but is able to impact the global core losses when interlaminar contacts are created in welded or interlocked stacks. Therefore, it is important to consider each loss component separately.

6.3. Application of magnetomechanical model to welding effect models

The internal stresses introduced by production techniques can be modelled using MEC-models where the magnetic reluctances represent the different stress areas in the material. The magnetic permeability and core loss components of these reluctances are defined according to the magnetomechanical model. Simultaneously, the MEC model can be used for modelling the inter-

laminar electrical connections that occur as a result of the disintegration of the insulating coating due to stack welding or interlocking. With the MEC model properly defined, an optimization of the stress reluctances can be carried out to find the optimal combination of stress and reluctance size.

First, the construction of the MEC-model is disclosed and the material specific stress dependency of the material model will be described in more detail. Then, a case study is elaborated in which the model parameters are identified using an inverse problem formulation using ring core measurements of a prototype welded stator stack. Finally, the model is validated by comparing MEC simulations and ring core measurements on a differently welded stator stack.

6.3.1 MEC model of welded ring core

In the model, the stator yoke of the machine is simplified as a ring core with rectangular welded region and magnetically degraded region (Fig. 6.5). Each welded section of the stator can be represented by a MEC as shown in Fig. 6.6. The weld seam geometry in this model was simplified using rectangular areas. The weld seam is located on the outer edge of the lamination. In the welding seam, the laminations are electrically connected. In the region near the welding seam (region 2 in Fig. 6.5), the heat from the welding process causes residual stress in the material but the electrical insulating coating remains intact. For regions 2 and 3, a uniform stress state is assumed in the model. This stress state influences the magnetic permeability necessary for calculating the magnetic flux in each reluctance. To accomodate the effect of stress, the magnetomechanical model is used. However, the magnetomechanical model is only valid when the direction of magnetization is parallel to the direction of stress while it is known that the stress dependency of electrical steel is anisotropic. The influence of this stress anisotropy can be modelled using the equivalent stress approach. This approach was used by several researchers [6, 18] and enables the calculation of magnetic properties under multi-axial stress when only uni-axial measurements are available. The equivalent stress was adopted from [18] and is described in the previous chapter. In regions 2 and 3 (Fig. 6.6), the stress is assumed to be directed radially away from the weld seam. This assumption corresponds to the results found in [82] and [76]. The stress in these areas is directed either 0° , 45° or 90° with respect to the magnetic flux direction (double-ended arrows in Fig. 6.6). For the reluctances where the residual stress is not parallel to the magnetization direction, the corresponding σ_{eq} is calculated according to [18] and used to determine the correction factors for each reluctance. In the proposed model, each reluctance in the network is defined by

$$\mathcal{R}(\sigma_{eq}, B) = \frac{l}{\mu_0 K_\mu(\sigma_{eq}) \mu_r(B) A} \quad (6.3)$$

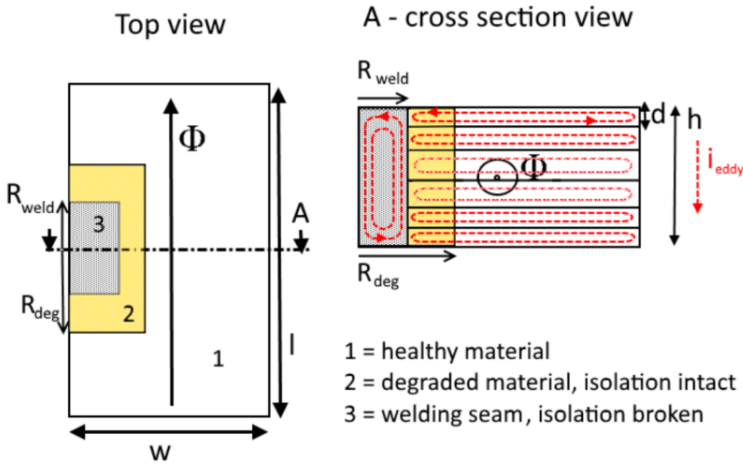


Figure 6.5: Top view and cross section view of a welded stack of laminations. Welded and degraded region are simplified to a rectangular area.

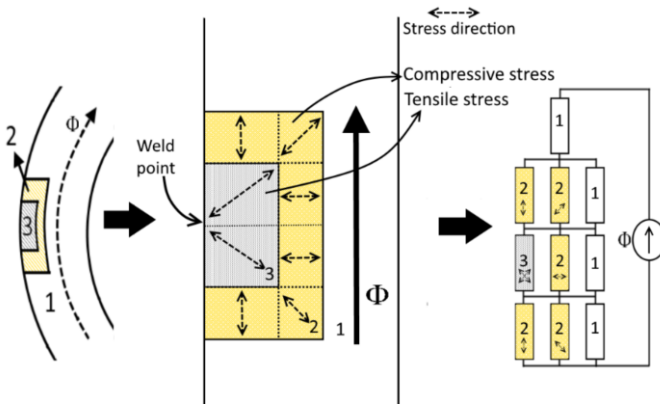


Figure 6.6: MEC model for a ring core with one weld seam where the flux perpendicular to the cross section travels through parallel branches of healthy, degraded and welded material. The indices of the reluctances indicate different stress-dependent material properties corresponding to the regions described in Fig. 6.5.

where l and A are the length and magnetic cross section of the reluctances. The relative magnetic permeability μ_r is the permeability when unaffected by stress. In Fig. 6.6, region 1 is the zone unaffected by stress where $K_\mu=1$. Regions 2 and 3 are affected by stress and K_μ is determined by first calculating σ_{eq} and afterwards applying the magnetomechanical model (6.1).

A summarizing list of the model assumptions is given here:

1. The weld seam area and its surrounding heat affected area are simplified as a rectangular area with dimensions specified in Fig. 6.5.
2. The curvature on the outer edge of the ring core is simplified to a straight line
3. A uniform isotropic stress state is assumed in each reluctance of the considered MEC, but stress anisotropy with respect to magnetization direction is considered.
4. The skin effect is neglected which is a valid assumption when considering sufficiently low frequencies.
5. The applied welding technique does not change the metallurgic composition of the weld seam. The electrical steel melts and bonds with adjacent laminations without any additional binding material during the welding process.

6.3.2 Coarse-scale stress dependent loss coefficients

In the previous subsections, it is described how the MEC accounts for the residual stresses in and near the welding seam by assigning a stress dependent magnetic permeability to each reluctance. Now, the MEC model can be solved for the flux density in each reluctance. Consequently, the magnetomechanical model can be applied again for calculating the stress-dependent core loss contribution of each reluctance using (6.2). The core loss components are then correctly determined by

$$P_{hyst}(\sigma_{eq}) = K_{hyst}(\sigma_{eq}) C_{hyst} B_p^2 f \quad (6.4)$$

$$P_{exc}(\sigma_{eq}) = \sqrt{K_{exc}(\sigma_{eq})} C_{exc} (B_p f)^{1.5} \quad (6.5)$$

6.3.3 Local classical loss in weld seam

In the previous section, it was mentioned that the classical losses remain unaffected by the stress state. However, as the welding seam forms a connecting bar of electrical steel at the outer edge of the stack, the local eddy currents in this bar can be calculated using the classical loss equation but with thickness d equal to the weld seam radius R_{weld} (as illustrated in Fig. 6.5). This way, the influence of the weld seam radius on the classical losses in the weld seam (region 3 in Fig. 6.5) is included in the model:

$$P_{cl,weld} = \frac{B_p^2 f^2 \kappa R_{weld}^2 \pi^2}{6\rho} \quad (6.6)$$

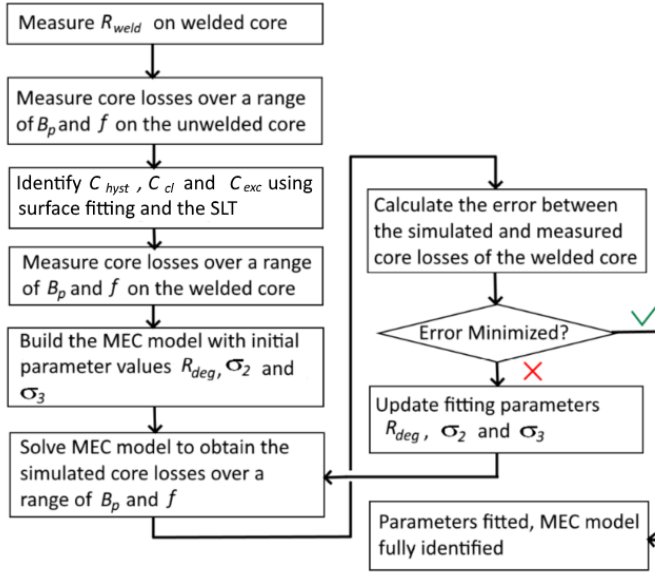


Figure 6.7: Flowchart describing optimization algorithm for stress-dependent welding model

6.3.4 Methodology

The proposed stress-based MEC model can simulate the core losses occurring in welded stator cores. In order to obtain accurate simulation results, a case-specific characterization should be done, which can be accomplished by following the procedure described here. First, the grade dependent coefficients (not to be confused with the correction factors due to stress) C_{hyst} , C_{cl} and C_{exc} need to be identified using loss measurements for different frequencies and peak flux densities on an unwelded stack. Then, measurements on a welded stack can be used to fit the unknown parameters in the proposed MEC model which are the stress states (σ_{eq2} and σ_{eq3} in regions 2 and 3 respectively) and size of the region near the weld seam (R_{deg}). An inverse problem formulation can be used as a fitting procedure. The calculated iron losses originate from solving the proposed MEC model, with σ_{eq2} , σ_{eq3} and R_{deg} fitted. (6.3), (6.4), and (6.5) were applied for calculating the losses in regions 1 and 2. The classical loss component was calculated using (2.9). In the welded region (3 in Fig. 6.6), the same equations apply except for the calculation of the classical losses, where (6.6) was used. The magnetomechanical model provides the correction factors, which are valid for one specific grade. This methodology is illustrated with a flowchart in Fig. 6.7.

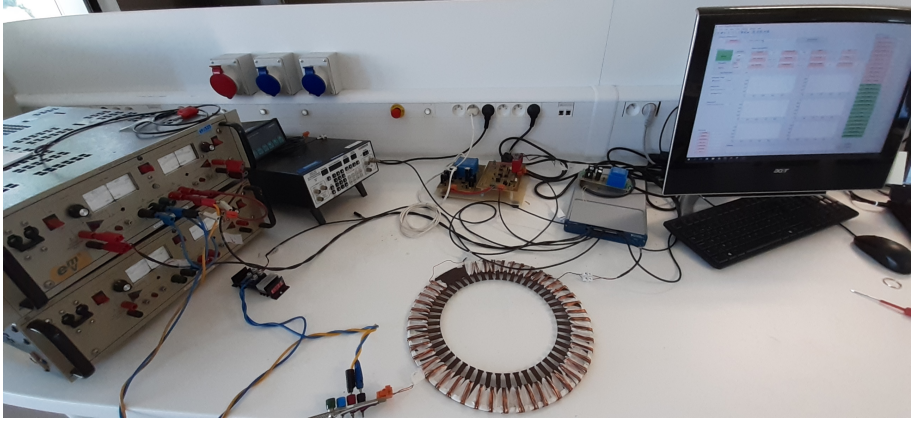


Figure 6.8: Setup used for obtaining loss measurements: amplifier (left), welded stator core (center) and data acquisition system (right).

6.3.5 Case study on M270-35A welded stator core

As a proof of concept, core losses were measured at different peak flux densities and excitation frequencies on a stack of M270-35A stator laminations before and after welding. The laminations were lasercut and afterwards stress relief annealed. This way, the cutting effect is reduced and a more accurate modelling of the welding effects is made possible. A stack of 15 laminations was welded on 4 equidistant locations around the edge of the yoke using TIG welding (compatible with assumption 5 in section 6.3.1) with welding current 90A at a welding speed of 4mm/s. The weld seam radius R_{weld} is not an unknown parameters and was measured to be 1.5mm. Global measurements of magnetic field strength H_s and magnetic flux density B_a were performed for a range of frequencies (10Hz - 200Hz) and peak flux densities (0.1 - 1.3T) using the setup displayed in Fig. 6.8. The data acquisition system consists of a National Instruments DAQ-card connected to a CPU running MATLAB software for Magnetic Measurements which was developed at Ghent University. The Kepco 50V/8A Bipolar Operational Amplifier was used for generating the controlled excitation field in the stator core. The measured losses in the unwelded stack were used to fit the parameters of the undamaged material, namely C_{hyst} (=0.0126), C_{cl} (=1.195e-5) and C_{exc} (=0.0011). Afterwards, the unknown model parameters (R_{deg} , σ_{eq2} and σ_{eq3}) are fitted using a combination of the MATLAB *genetic algorithm* and *fmincon* toolboxes. In the next paragraph, the measurements are compared to the losses calculated by the fitted model. Also, a validation of the model is elaborated.

6.3.6 Results

After fitting the parameters based on loss measurements on the unwelded and welded (with 4 seams) core over a range of frequencies (10, 50 and 200Hz) and peak flux densities (0.1 T to 1.3 T), it was found that for a compressive stress state of $\sigma_{eq2} = 220$ MPa in region 2 and $R_{deg} = 13$ mm the simulations correspond accurately with the measurements. The fitted stress state in the weld seam σ_{eq3} was found to be 330 MPa tensile stress, however it must be noted that this factor appeared to play a minor role in the loss calculation due to the comparatively small size of R_{weld} in the total width of 23 mm (w_{tot} in Fig. 6.5). Based on the local measurement results found in literature [33], [76], it was assumed that the residual stress in the welded region σ_{eq3} was tensile and the residual stress in the surrounding damaged region σ_{eq2} was compressive. This assumption was incorporated in the inverse problem by setting the corresponding constraints to the solutions. Fig. 6.9 displays the measured and simulated specific iron losses for different frequencies and peak flux densities for the welded and unwelded case. This graph shows a good correspondence between the fitted model and the measurements. The deviation between the measured and simulated values for each case can partially be explained by the noise-sensitive nature of the measurement setup. Similar to the approach described in [53], the relation between the V_0 and B_p was neglected in the model in order to simplify the stress dependency of V_0 . This could lead to inaccuracies when the material is saturated. Therefore, measurements and fitting were done for B_p -values up to 1.3 T. In Fig. 6.10, the model (which was fitted with loss measurements at 10, 50 and 200 Hz on a 4 weld seam stack) was validated in case the number of weld seams doubled to 8 at frequency 100 Hz. Here, measurements on a welded stack with 8 weld seams are compared to model calculations when 8 weld sections are simulated. This shows that the model succeeds accurately in predicting the effect of core losses for varying frequencies and varying amounts of weld seams.

6.3.7 Effect of Increasing Weld Radius

The results obtained from the simulations show that the local classical losses in the welded zone are significantly higher than the other loss components. In this section, the effect of the weld radius R_{weld} on the total core losses is simulated and compared to the results presented in [77]. In this work, Wang and Zhang performed FE-simulations and analytical calculations on welded laminations where the total width was 5 mm and the sheet thickness was 0.27 mm. These results show that the eddy current losses increase exponentially when the weld radius increases from 0.8 mm to 1.3 mm at 50 Hz excitation frequency. With the identified fitting parameters from the previous section kept constant, the effect of increasing weld radius (from 3.7 mm to 6 mm, in order to keep the

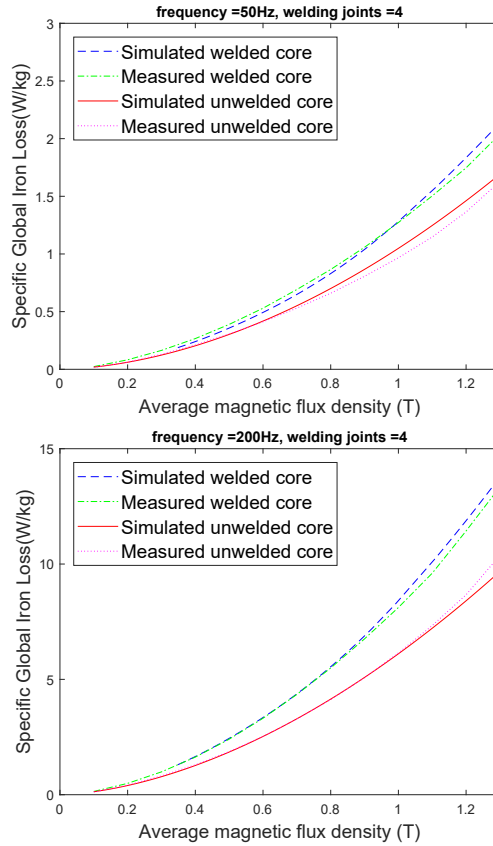


Figure 6.9: Comparison of the simulated specific losses and measured specific losses as a function of peak flux density for 50 Hz and 200 Hz excitation frequencies. The peak flux density values are averaged over the magnetic cross section as they are known to vary locally near the welded region.

ratio of the weld radius over the total section width equal for both cases) on the total core losses is simulated and shown in Figure 6.11. This figure shows that the proposed stress-dependent MEC model incorporates adequately the effect of increasing eddy current core losses due to increasing weld radius, similar to the results in [77].

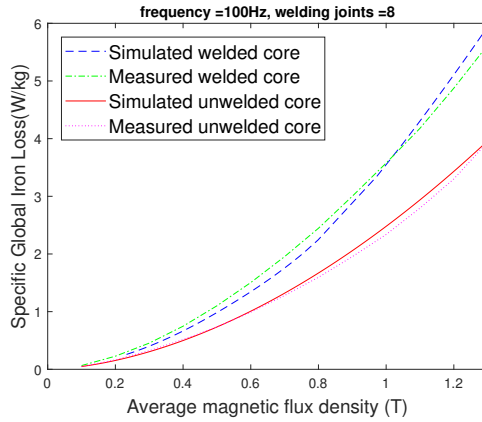


Figure 6.10: Comparison of the simulated specific losses and measured specific losses as a function of peak flux density for 100 Hz and 8 welding seams. The model was fitted using loss measurements at different frequencies of the stack with 4 weld seams.

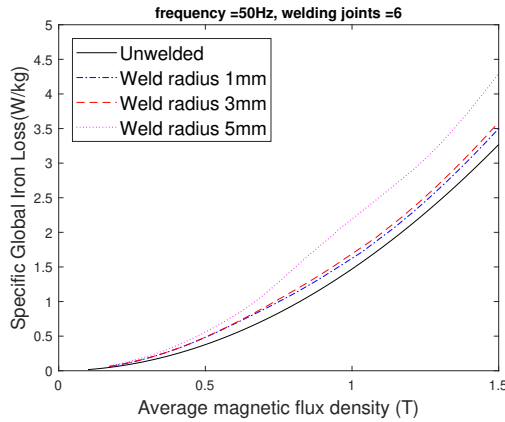


Figure 6.11: Simulated core losses as a function of peak flux density, demonstrating the effect of increasing weld radius on the total core losses when all other model parameters remain equal.

6.4. Application of magnetomechanical relation to interlocking effect models

The same methodology can be applied to the problem of simulating interlocking effects. However, the MEC-configuration is different from a welded stator core, due to the location of the degraded zones. An adapted MEC model

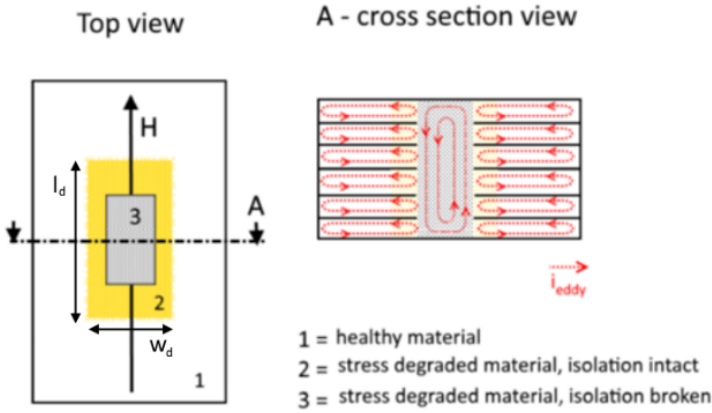


Figure 6.12: Top view and cross section view of an interlocked stack of laminations.

can be built which is more adequate for simulating interlocking degradation. Assuming that the location of the interlocking dowel is central between the two edges in the stator yoke, the configuration of the reluctances is mirrored across the interlocking point. In Fig. 6.12, the cross section view of a stack of interlocked laminations is illustrated. The short circuit enabling the formation of interlaminar eddy currents and the surrounding stress-degraded area are drawn correspondingly. This simplified interpretation of interlocking damage can be translated into a MEC-model as shown in Fig. 6.13. The practicability of the proposed methodology is again demonstrated in the form of a case study on interlocked stator cores of NO27 steel grade.

6.4.1 Case study on NO27 interlocked stator core

The stator core prototype in this case study has an inner and outer yoke diameter of 340 and 400 mm, respectively. The interlocking points were positioned central on the yoke, with the longest edge of the interlocking tool parallel to the yoke edge. The central grey area in Fig. 6.13 is defined by the specific interlocking toolhead used for this prototype. The interlocking points were manufactured using a flat and rectangular toolhead of 3 mm by 8 mm. The surrounding degraded area symbolizes the material stressed during the interlocking punch. As an assumption, this area is also considered rectangular. The modifications to the MEC-model that were necessary for accommodating interlocking damage also have an impact on the methodology. The flowchart describing the identification methodology for welding damage (Fig. 6.7) uses one geometrical parameter (R_{deg}) and two material parameters (σ_{eq2} , σ_{eq3}). In

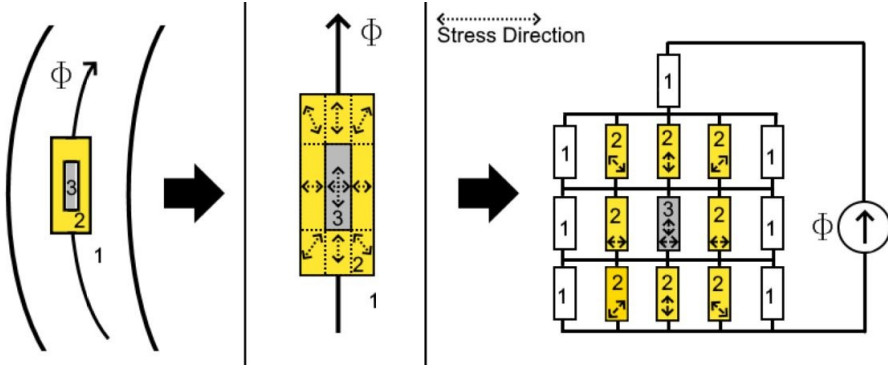


Figure 6.13: MEC model for a ring core with one interlocking point centrally placed between the ring core edges where the flux perpendicular to the cross section travels through parallel branches of healthy, degraded and welded material. The indices of the reluctances indicate different stress-dependent material properties corresponding to the regions described in Fig. 6.12.

the interlocking configuration, the material parameters remain similar, but an additional geometrical parameters is necessary for describing the stress degraded area. The two geometrical parameters are l_d and w_d . After running the inverse problem, the simulated core loss corresponded accurately to the measured core losses (Fig. 6.14). The fitted material parameters were $\sigma_{eq2} = 500$ MPa and $\sigma_{eq3} = -60$ MPa. The fitted geometrical parameters were $l_d = 13$ mm and $w_d = 7$ mm. Both the material parameters and the geometrical parameters are fitted so that the model corresponds to the global magnetic measurement results. It is important to remark that these parameters might not correspond to the realistic physical material state in and around the area damaged by interlocking.

6.4.2 Effect of number of interlocking points

For the model validation, the global core losses were simulated for various amounts of interlocking points and then compared to experimental results found in literature. In the experiments reported in [27], the core losses were measured on M400-50A ring core samples with 0, 2, 4 and 8 interlocking points. A linear increase in core losses was reported with increasing amounts of interlocking points. The simulation results obtained from the proposed stress-based MEC model shown in Fig. 6.15 show a similar trend.

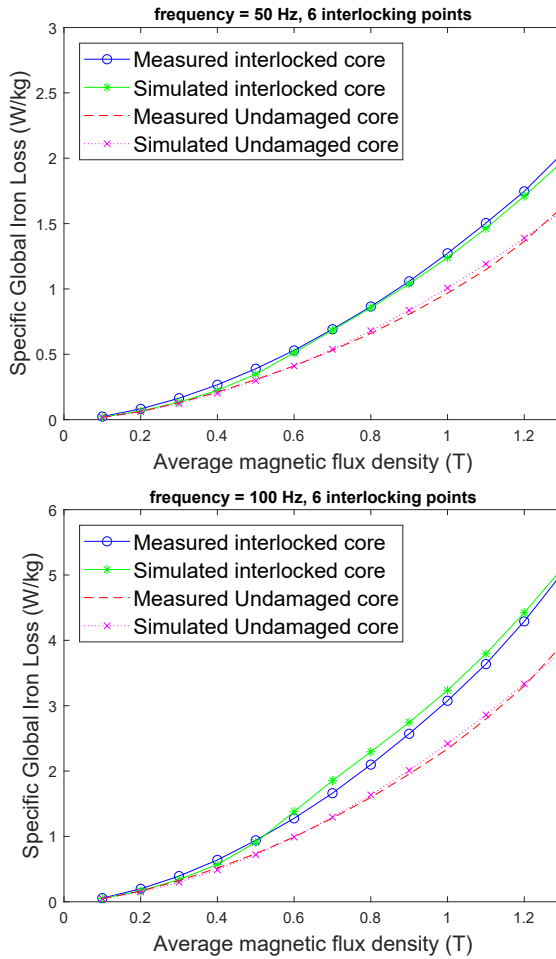


Figure 6.14: Comparison of the simulated specific losses and measured specific losses as a function of peak flux density at 50 Hz and 100 Hz for a NO27 stator ring core with 6 interlocking points.

6.5. Conclusion

This chapter presented a stress-based MEC model that may be included in a complete MEC model of an electrical machine. The model accounts for local residual stress near the interlocked or welded regions and for local eddy currents occurring near these regions. The model succeeds accurately in predicting the complex iron losses in electrical steel stator core stacks for varying amounts of excitation regimes. When the parameters are fitted, an optimal stress state is found near the welding or interlocking point and in the

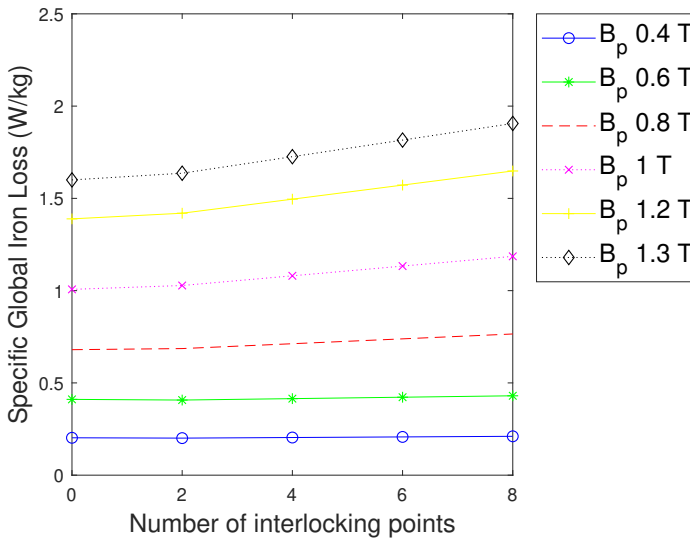


Figure 6.15: Simulated specific global core loss at 50 Hz as a function of the number of interlocking points on the stator core geometry.

surrounding degraded region. Although the model simplifies the complex degradation geometry and magnetic sensitivity to stress and assumes uniform residual stress states in different sub regions, it provides an interesting tool for studying the prominent effects of welding or interlocking and allows for a qualitative study of the effect of different process parameters on the additional iron losses. When the model parameters are fitted correctly based on experimental observations on stator cores, it is possible to calculate additional core losses due to welding or interlocking for varying amounts of welding or interlocking points and excitation regimes. The application of the model on prototype stator cores of NO27 and M270-35A grade steel has shown that with a limited number of magnetic measurements, the models can be fully parametrized. As shown in the case studies, the model was successfully validated for both the interlocked and welded stator core.

7

General Conclusions and Perspectives

7.1. Conclusions

The PhD thesis focuses on changes in magnetic material properties in ferromagnetic cores due to construction techniques. The first chapter positions this topic in the research area of electrical machine design. Chapter 2 describes the domain theory and how it manifests itself on a macroscopic level in BH loops. A brief explanation of the magnetic measurement techniques and modelling techniques used in this thesis is added for clarification. In Chapter 3, a series of experiments have demonstrated the quantitative differences between the magnetic properties measured in differently cut samples of electrical steel. When comparing two identical geometries of grade NO27, the measured core losses at 50 Hz in the laser cut samples were approximately 30 % and 25 % higher than the nibble punched samples at peak flux density 1 T and 1.5 T, respectively. This implies that laser cutting introduces the largest magnetic material degradation. A similar experiment was done using GO M100-23P grade steel, where samples of laser cut, waterjet cut and guillotine cut were compared. Measurements of core losses and magnetic permeability indicated that the water jet cutting technique introduces the least

amount of magnetic degradation to the material. Laser cutting proved again to introduce the largest additional core losses, up to 37 % higher than guillotine cutting at 1.5 T and 50 Hz. Another experiment was designed to study the influence of stress relief annealing. Two M270-35A stator cores were manufactured, one using laser cutting and one using a traditional punch and die. The magnetic properties of both cores were measured before and after stress relief annealing. The measurements showed that stress relief annealing has the highest restorative capacity for the laser cut core, which had experienced the worst material degradation during cutting. Annealing restored the magnetic properties significantly, reducing the core losses almost by 20 % at 1 T and 50 Hz excitation. The annealing process had only a modest effect on the punched sample. Finally, the effects of welding and joining were measured on stator cores of NO27 and M400-50A grade steel, respectively. In both experiments, the joining technique caused a significantly higher core loss (up to 11 % higher for interlocking and 60 % for welding, depending on the excitation regime) and decreased average magnetic permeability. When comparing those experiments to results from literature, it was concluded that the degree of degradation for each technique was very case specific. Joining techniques such as interlocking and welding have multiple process variables, all of them possibly having an impact on the resulting magnetic degradation.

Chapter 4 focuses on the modelling aspect of these construction techniques. A series of methodologies is elaborated that can be used for incorporating the effects of construction into the design of electrical machines. Using M100-23P grade steel, it was demonstrated how a material model can be built that introduces the distance to the cutting edge as a variable. Then, the model was fitted for three different cutting techniques, and afterwards applied in a MEC model of a YASA machine. As expected, the machine performed worst with the laser cut material model and best with the water jetted material model. The model parameters that were fitted on measurements of the laser cut strips produced a decrease in EMF of up to 1.25 % and a decrease in motor torque of up to 1.2 %. The simulated core losses in the machine model were up to 180 % higher for the laser cut steel than for the waterjet steel. For obvious reasons, the distance to the cutting edge can not be used as a variable when attempting to model welding effects. Modelling the effect of welding in stator cores of M400-50A, a different approach was taken. Now, the yoke of the stator core was assumed to have uniform magnetic properties. Any local effects of welding were disregarded and the material model was fitted using core loss measurements on the same stator core both before and after welding. The welded yoke material model had significantly worse magnetic properties than the yoke material model without welding. The material models were applied in a FE model, where it was found that the simulated stator core losses were approximately 10 % higher after welding than before. The FE model was af-

terwards validated by comparing measured core losses in a 37 kW blocked rotor induction machine with a laser welded stator to the FE model. Although the FE model simulations and full machine measurements showed a similar trend during validation, there was a significant deviation of approximately 12 % in core losses between the model and the measurements. Chapter 4 was concluded with another measurement based methodology for incorporating interlocking damage, using specific sets of Epstein strips to fit a local degradation material model. The methodology was demonstrated on NO27 grade steel and successfully validated by comparing the simulations to measurements on a realistic stator geometry.

In Chapter 5, the main focus was placed on the underlying reasons for the observed magnetic material degradation. The impact of uni-axial stress on M270-35A steel was measured in the compressive and tensile elastic regions. The obtained results corresponded accurately to the literature in this field. In one experiment, strips of M270-35A grade steel were stressed beyond the yield strength and measured both before and after the mechanical load was released. In this stress state, it was observed that releasing the load actually increased the core losses and therefore degraded the sample even further. When the sample was strained up to 10.4 %, releasing the load increased the hysteresis losses by 55 % with respect to the strained sample. The magnetic permeability decreases by a factor of 5 at 1 % strain and by a factor of 10 at 10 % strain. Using TEM, the microstructure of the strained samples was analyzed and it was found that the dislocation density had increased by 330 % with respect to the unloaded state. The increase in dislocation density showed a positive correlation to the observed change in hysteresis losses. At the end of Chapter 5, an experimental setup was presented which allowed the measurement of the effect of compressive stacking stress. Differently cut strips of M100-23P steel were placed under compressive stress in the thickness direction and the resulting magnetic properties were measured. Contrary to the stress free state - where water jetted samples exhibited the least core losses when compared to laser cut or guillotine cut samples - it was found that the water jetted samples now caused the largest amount of core loss. Further analysis using core loss separation resulted in the isolation of the classical loss component as the main contributor to the observed effect. A possible explanation for this effect could be found in the removal of the insulating coating during cutting. If water jet cutting removes more coating surface than laser cutting or guillotine cutting, the interlaminar electrical resistance could be significantly smaller when the stack of samples is compressed in the thickness direction. This would facilitate more interlaminar eddy currents, increasing the classical loss component. Alternatively, the water jetting technique might cause a larger burr on the cutting edge. This extra edge burr could also cause

a better interlaminar contact when the samples are stacked, resulting in increased classical losses.

In Chapter 6, an alternative approach to modelling manufacturing effects is proposed where the main underlying cause - residual stress - is incorporated into the material degradation model. The experimental results from Chapter 5 were captured into a magnetomechanical model using a piece-wise interpolation function with parameters that depend on both the excitation frequency and peak flux density. The resulting model is a combination of the traditional MEC model and this magnetomechanical model. This approach was applied for both interlocking and welding, and proved to be highly accurate after careful validation.

7.2. Future Work

The investigations carried out in this project offered interesting insights for further research. Besides interlocking and welding, glue bonding offers an interesting alternative for joining laminations. The impact of glue bonding on the magnetic properties of stacks has received far less attention in literature when compared to welding or interlocking. However, this technique potentially causes less damage to the magnetic material properties because it does not require large local plastic deformation or local heating of the material.

Due to the recent advances in the field of 3D metal printing, an interesting topic of further research could be to investigate the capabilities of additive manufacturing applied to ferromagnetic core design. Although several technical challenges still need to be overcome, this technology potentially has the capacity to revolutionize the current production process of ferromagnetic cores. A deeper investigation of the local phenomena in laminations can be done using local magnetic measurements. The EELAB at Ghent University has a lot of in-house expertise in this area. The local magnetic degradation near cutting edges and welding seams or interlocking joints can be measured using the needle probe method as described in [2]. However, in order to achieve an accurate measurement of the local magnetic properties, the available sensors should be improved to achieve a higher spatial resolution.

In this PhD, dislocation density measurements of plastically strained electrical steel were discussed and related to the magnetic properties. Due to technical restrictions however, the measurements were limited to the strained samples after the mechanical load was released. As a topic of further investigation, the dislocation density of the material can be analysed both before and after the mechanical load is released. Additionally, other microstructural properties could be measured and related to the magnetic properties.

In the last chapter of this PhD, a new approach to modelling manufacturing effect on magnetic properties of electrical steel was discussed. However, sev-

eral assumptions on the geometry and local material properties of the modelled regions were necessary to achieve a model that fitted the measurements accurately. Further research could focus on the analysis of these assumptions with the goal of refining the model.

Bibliography

- [1] A.a.-E. Abdallh. *An Inverse Problem Based Methodology with Uncertainty Analysis for the Identification of Magnetic Material Characteristics of Electromagnetic Devices*. PhD thesis, 2012.
- [2] A.a.-E. Abdallh and L. Dupré. Local magnetic measurements in magnetic circuits with highly non-uniform electromagnetic fields. *Measurement Science and Technology*, 21(4), 2010.
- [3] AK Steel. Selection of Electrical Steels for Magnetic Cores, 2007.
- [4] N. Alatawneh, T. Rahman, D. A. Lowther, and R. Chromik. Design and analysis of a toroidal tester for the measurement of core losses under axial compressive stress. *Journal of Magnetism and Magnetic Materials*, 432:519–526, 2017.
- [5] W.M. Arshad, T. Ryckebusch, F. Magnussen, H. Lendenmann, B. Eriksson, J. Soulard, and B. Malmros. Incorporating Lamination Processing and Component Manufacturing in Electrical Machine Design Tools. In *2007 IEEE Industry Applications Annual Meeting*, pages 94–102, 2007.
- [6] U. Aydin, P. Rasilo, F. Martin, A. Belahcen, L. Daniel, A. Haavisto, and A. Arkkio. Effect of multi-axial stress on iron losses of electrical steel sheets. *Journal of Magnetism and Magnetic Materials*, 469(July 2018):19–27, 2019.
- [7] M. Bali, H. De Gersem, and A. Muetze. Finite-element modeling of magnetic material degradation due to punching. *IEEE Transactions on Magnetics*, 50(2):1–4, 2014.
- [8] M. Bali, H. De Gersem, and A. Muetze. Determination of Original Nondegraded and Fully Degraded Magnetic Properties of Material Subjected to Mechanical Cutting. *IEEE Transactions on Industry Applications*, 52(3):2297–2305, 2016.
- [9] G. Bertotti. General Properties of Power Losses in Soft Ferromagnetic Materials., 1988.
- [10] G. Bertotti. General properties of power losses in soft ferromagnetic materials. *IEEE Transactions on Magnetics*, 24(1):621–630, 1988.
- [11] G. Bertotti, F. Fiorillo, and G. Soardo. The Prediction of Power Losses in Soft Magnetic Materials. *Journal De Physique Colloques*, 49:1915–1919, 1988.

- [12] K. Bourchas, A. Stening, J. Soulard, A. Broddefalk, M. Lindenmo, M. Dahlen, and F. Gyllensten. Influence of Cutting and Welding on Magnetic Properties of Electrical Steels. *IEEE Transactions on Industry Applications*, 53(5):4269–4278, 2017.
- [13] K. Bourchas, A. Stening, J. Soulard, A. Broddefalk, M. Lindenmo, M. Dahlen, and F. Gyllensten. Quantifying Effects of Cutting and Welding on Magnetic Properties of Electrical Steels. *IEEE Transactions on Industry Applications*, 53(99):4269–4278, 2017.
- [14] H. Cao, L. Hao, J. Yi, X. Zhang, Z. Luo, S. Chen, and R. Li. The influence of punching process on residual stress and magnetic domain structure of non-oriented silicon steel. *Journal of Magnetism and Magnetic Materials*, 406:42–47, 2016.
- [15] H. Cao, L. Hao, J. Yi, X. Zhang, Z. Luo, S. Chen, and R. Li. The influence of punching process on residual stress and magnetic domain structure of non-oriented silicon steel. *Journal of Magnetism and Magnetic Materials*, 406:42–47, 2016.
- [16] C. C. Chiang, A. M. Knight, M. F. Hsieh, M. G. Tsai, B. H. Liu, I. G. Chen, Z. L. Gaing, and M. C. Tsai. Effects of annealing on magnetic properties of electrical steel and performances of SRM after punching. *IEEE Transactions on Magnetism*, 50(11), 2014.
- [17] A. J. Clerc and A. Muetze. Measurement of stator core magnetic degradation during the manufacturing process. *IEEE Transactions on Industry Applications*, 48(4):1344–1352, 2012.
- [18] L. Daniel and O. Hubert. Equivalent stress criteria for the effect of stress on magnetic behavior. *IEEE Transactions on Magnetism*, 46(8):3089–3092, 2010.
- [19] L. Dupre, M.J. Sablik, R. Van Keer, and J. Melkebeek. Modelling of microstructural effects on magnetic hysteresis properties. *Journal of physics D: applied physics*, 2086(35):2086–2090, 2002.
- [20] S. Elfgen, S. Steentjes, S. Böhmer, D. Franck, and K. Hameyer. Influences of material degradation due to laser cutting on the operating behaviour of PMSM using a continuous local material model. *IEEE Transactions on Industry Applications*, 53(3):1837–1842, 2016.
- [21] R. G. Hancock. The effects of stress relief annealing on the magnetic properties of cut laminations and assembled cores produced from nonoriented electrical steel. *Journal of Magnetism and Magnetic Materials*, 19:65–68, 1980.
- [22] H. M. S. Harstick, M. Ritter, and W. Riehemann. Influence of Punching and Tool Wear on the Magnetic Properties of Nonoriented Electrical Steel. *IEEE Transactions on Magnetism*, 50(4):3–6, 2014.
- [23] A. Hemeida, A. Lehtikainen, P. Rasilo, H. Vansompel, A. Belahcen, A. Arkkio, and P. Sergeant. A Simple and Efficient Quasi-3D Mag-

- netic Equivalent Circuit for Surface Axial Flux Permanent Magnet Synchronous Machines. *IEEE Transactions on Industrial Electronics*, 66(11):8318–8333, 2019.
- [24] K. H. Ho and S. T. Newman. State of the art electrical discharge machining (EDM). *International Journal of Machine Tools and Manufacture*, 43(13):1287–1300, 2003.
- [25] M. Hofmann, H. Naumoski, U. Herr, and H. Herzog. Magnetic Properties of Electrical Steel Sheets in Respect of Cutting : Micromagnetic Analysis and Macromagnetic Modeling. *IEEE Transactions on Magnetics*, 52(2), 2016.
- [26] T. P. Holopainen, P. Rasilo, and A. Arkkio. Identification of Magnetic Properties for Cutting Edge of Electrical Steel Sheets. *IEEE Transactions on Industry Applications*, 53(2):1785–1789, 2016.
- [27] S. Imamori, S. Steentjes, and K. Hameyer. Influence of Interlocking on Core Magnetic Properties. *IEEE Transactions on Magnetics*, 53(11):496–502, 2017.
- [28] V. E. Iordache, F. Ossart, and E. Hug. Magnetic characterisation of elastically and plastically tensile strained non-oriented Fe-3.2%Si steel. *Journal of Magnetism and Magnetic Materials*, 254-255:57–59, 2003.
- [29] T. Kai, S. Aihara, T. Todaka, and M. Enokizono. Investigation of measured distributions of local vector magnetic properties in a three-phase induction motor model core. *Journal of Electrical Engineering*, 61(7 SUPPL):115–118, 2013.
- [30] Y. Kai, Y. Tsuchida, T. Todaka, and M. Enokizono. Influence of stress on vector magnetic property under rotating magnetic flux conditions. *IEEE Transactions on Magnetics*, 48(4):1421–1424, 2012.
- [31] J. Karthaus, S. Steentjes, N. Leuning, and K. Hameyer. Effect of mechanical stress on different iron loss components up to high frequencies and magnetic flux densities. In *COMPEL - The International Journal for Computation and Mathematics in Electrical and Electronic Engineering*, volume 36, pages 580–592, 2017.
- [32] M. Kawabe, T. Nomiyama, A. Shiozaki, M. Mimura, N. Takahashi, and M. Nakano. Magnetic properties of particular shape specimen of nonoriented electrical steel sheet under compressive stress in thickness direction. *IEEE Transactions on Magnetics*, 48(11):3462–3465, 2012.
- [33] K. Kesavan, K. Ravisankar, S. Parivallal, and P. Sreeshylam. Non Destructive Evaluation of Residual Stresses in Welded Plates Using the Barkhausen Noise Technique. *Experimental Techniques*, 29(5):17–21, 2005.
- [34] D. Kowal, P. Sergeant, L. Dupré, and L. Vandenbossche. Comparison of Iron Loss Models for Electrical Machines With Different Frequency Domain and Time Domain Methods for Excess Loss Prediction. *IEEE Transactions on Magnetics*, 51(1), 2015.

- [35] A. Kraemer, M. Veigel, P. Pontner, M. Doppelbauer, and G. Lanza. Influences of separation and joining processes on single tooth laminated stacks. In *2016 6th International Electric Drives Production Conference, EDPC 2016 - Proceedings*, pages 178–185, 2016.
- [36] A. Krings, S. Nategh, O. Wallmark, and J. Soulard. Influence of the welding process on the performance of slotless pm motors with sife and nife stator laminations. *IEEE Transactions on Industry Applications*, 50(1):296–306, 2014.
- [37] Y. Kurosaki, H. Mogi, H. Fujii, T. Kubota, and M. Shiozaki. Importance of punching and workability in non-oriented electrical steel sheets. *Journal of Magnetism and Magnetic Materials*, 320(20):2474–2480, 2008.
- [38] E. Lamprecht, M. Homme, and T. Albrecht. Investigations of eddy current losses in laminated cores due to the impact of various stacking processes. In *2012 2nd International Electric Drives Production Conference, EDPC 2012 - Proceedings*, pages 1–8, 2012.
- [39] N. Leuning, S. Steentjes, M. Schulte, W. Bleck, and K. Hameyer. Effect of elastic and plastic tensile mechanical loading on the magnetic properties of NGO electrical steel. *Journal of Magnetism and Magnetic Materials*, 417:42–48, 2016.
- [40] M. Lindenmo, A. Coombs, and D. Snell. Advantages, properties and types of coatings on non-oriented electrical steels. *Journal of Magnetism and Magnetic Materials*, 215:79–82, 2000.
- [41] Y. Liu, S. K. Kashif, and A. M. Sohail. Engineering considerations on additional iron losses due to rotational fields and sheet cutting. In *Proceedings of the 2008 International Conference on Electrical Machines, ICEM’08*, pages 1–4, 2008.
- [42] M. LoBue, C. Sasso, V. Basso, F. Fiorillo, and G. Bertotti. Power losses and magnetization process in Fe-Si non-oriented steels under tensile and compressive stress. *Journal of Magnetism and Magnetic Materials*, 215:124–126, 2000.
- [43] J. M. Makar and B. K. Tanner. Effect of plastic deformation and residual stress on the permeability and magnetostriction of steels. *Journal of Magnetism and Magnetic Materials*, 222(3):291–304, 2000.
- [44] M. C. Marion-Pera, A. Kedous-Lebouc, T. Waeckerle, and B. Cornut. Characterization of SiFe Sheet Insulation. *IEEE Transactions on Magnetics*, 31(4):2408–2415, 1995.
- [45] B. Mehdi, R. Badji, V. Ji, B. Allili, D. Bradai, F. Deschaux-Beaume, and F. Soulié. Microstructure and residual stresses in Ti-6Al-4V alloy pulsed and unpulsed TIG welds. *Journal of Materials Processing Technology*, 231:441–448, 2016.

- [46] D. Miyagi, Y. Aoki, M. Nakano, and N. Takahashi. Effect of compressive stress in thickness direction on iron losses of nonoriented electrical steel sheet. *IEEE Transactions on Magnetics*, 46(6):2040–2043, 2010.
- [47] T. Nakayama and H. Kojima. Interlocking performances on non-oriented electrical steels. *Journal of Materials Engineering and Performance*, 16(1):7–11, 2007.
- [48] H. Naumoski, A. Maucher, and U. Herr. Investigation of the influence of global stresses and strains on the magnetic properties of electrical steels with varying alloying content and grain size. In *2015 5th International Conference on Electric Drives Production, EDPC 2015 - Proceedings*, pages 1–8, 2015.
- [49] H. Naumoski, B. Riedmüller, A. Minkow, and U. Herr. Investigation of the influence of different cutting procedures on the global and local magnetic properties of non-oriented electrical steel. *Journal of Magnetism and Magnetic Materials*, 392:126–133, 2015.
- [50] G. Paltanea, V. Manescu, I. V. Nemoianu, H. Gavrilă, and P. C. Andrei. Influence of cutting technologies on the magnetic anisotropy of grain oriented electrical steel. In *2017 Electric Vehicles International Conference, EV 2017*, volume 2017-Janua, pages 1–4, 2017.
- [51] S. C. Paolinelli and M. A. da Cunha. Effect of stress relief annealing temperature and atmosphere on the magnetic properties of silicon steel. *Journal of Magnetism and Magnetic Materials*, 304(2):599–601, 2006.
- [52] V. Permiakov. *1D and 2D Magnetization in Electrical Steels under Uniaxial Stress*. PhD thesis, Ghent University, 2005.
- [53] V. Permiakov, L. Dupré, A. Pulnikov, and J. Melkebeek. Loss separation and parameters for hysteresis modelling under compressive and tensile stresses. *Journal of Magnetism and Magnetic Materials*, 272-276(SUPPL. 1):2003–2004, 2004.
- [54] V. Permiakov, L. Dupré, A. Pulnikov, and J. Melkebeek. 2D magnetization of grain-oriented 3%-Si steel under uniaxial stress. *Journal of Magnetism and Magnetic Materials*, 290-291 PA:1495–1498, 2005.
- [55] D. Philips. *Optimizing design of the switched reluctance motor*. PhD thesis, Ghent University, 1994.
- [56] A. Pulnikov. *Modification of Magnetic Properties of Non Oriented Electrical Steels by the Production of Electromagnetic Devices*. PhD thesis, Ghent University, 2004.
- [57] A. Pulnikov, R. Decocker, V. Permiakov, L. Dupré, L. Vandeveldel, R. Petrov, J. Melkebeek, Y. Houbaert, J. Gyselinck, and H. Wisselink. The relation between the magnetostriction and the hysteresis losses in the non-oriented electrical steels. *Journal of Magnetism and Magnetic Materials*, 290-291 PA:1454–1456, 2005.

- [58] J. Pyrhönen, T. Jokinen, V. Hrabovcová, and H. Niemelä. *Design of Rotating Electrical Machines*. 2008.
- [59] M. Rekik, O. Hubert, and L. Daniel. Validation of a multiscale magneto-mechanical hysteresis model using multiaxial experiments To cite this version : HAL Id : hal-01552444 Validation of a multiscale magneto-mechanical hysteresis model using multiaxial experiments. In *CEFC*, page 132, 2014.
- [60] A. Saleem, N. Alatawneh, R. R. Chromik, and D. A. Lowther. Effect of Shear Cutting on Microstructure and Magnetic Properties of Non-Oriented Electrical Steel. *IEEE Transactions on Magnetics*, 256(5):20–31, 2003.
- [61] T. Schade, R. M. Ramsayer, and J P Bergmann. Laser Welding of Electrical Steel Stacks. In *2014 4th International Electric Drives Production Conference (EDPC)*, number 02, pages 1–6, 2014.
- [62] A. Schoppa, H. Louis, F. Pude, and Ch. Von Rad. Influence of abrasive waterjet cutting on the magnetic properties of non-oriented electrical steels. *Journal of Magnetism and Magnetic Materials*, 254-255:370–372, 2003.
- [63] A. Schoppa, J. Schneider, C. D. Wuppermann, and T. Bakon. Influence of welding and sticking of laminations on the magnetic properties of non-oriented electrical steels. *Journal of Magnetism and Magnetic Materials*, 254(255):367–369, 2003.
- [64] J. X. Shen, G. Y. Zhou, S. L. Jin, and H. Hao. Analysis of iron loss in interlocked lamination core. In *2015 International Conference on Sustainable Mobility Applications, Renewables and Technology, SMART 2015*, pages 2–5, 2015.
- [65] W. Shi, J. Liu, and C. Li. Effect of cutting techniques on the structure and magnetic properties of a high-grade non-oriented electrical steel. *Journal of Wuhan University of Technology-Mater. Sci. Ed.*, 29(6):1246–1251, 2014.
- [66] D. Singh, P. Rasilo, F. Martin, A. Belahcen, and A. Arkkio. Effect of Mechanical Stress on Excess Loss of Electrical Steel Sheets. *IEEE Transactions on Magnetics*, 51(11):1–4, 2015.
- [67] Deepak Singh. *Effect of Stress on Magnetic Properties of Electrical Steel Sheet and Core Losses in Electrical Machines*. PhD thesis, Aalto University, 2016.
- [68] S. Steentjes, G. Von Pfingsten, and K. Hameyer. An application-oriented approach for consideration of material degradation effects due to cutting on iron losses and magnetizability. *IEEE Transactions on Magnetics*, 50(11):2–5, 2014.
- [69] R. Sundaria, A. Daem, O. Osemwinyen, A. Lehtikainen, P. Sergeant, A. Arkkio, and A. Belahcen. Effects of stator core welding on an induction machine – Measurements and modeling. *Journal of Magnetism and Magnetic Materials*, 499(November 2019):166280, 2020.

- [70] R. Sundaria, A. Hemeida, A. Arkkio, A. Daem, P. Sergeant, and A. Belahcen. Effect of Different Cutting Techniques on Magnetic Properties of Grain Oriented Steel Sheets and Axial Flux Machines. In *Industrial Electronics Conference*, pages 1022–1027. IEEE, 2019.
- [71] L. Vandenbossche, S. Jacobs, X. Jannot, M. McClelland, J. Saint-Michel, and E. Attrazic. Iron loss modelling which includes the impact of punching, applied to high-efficiency induction machines. In *2013 3rd International Electric Drives Production Conference, EDPC 2013 - Proceedings*, pages 1–10. IEEE, 2013.
- [72] H. Vansompel, P. Sergeant, L. Dupré, and A. Van Den Bossche. Axial-flux PM machines with variable air gap. *IEEE Transactions on Industrial Electronics*, 61(2):730–737, 2014.
- [73] M. Veigel, A. Krämer, G. Lanza, and M. Doppelbauer. Investigation of the Impact of Production Processes on Iron Losses of Laminated Stator Cores for Electric Machines. In *2016 IEEE Energy Conversion Congress and Exposition (ECCE)*, pages 1–5, 2016.
- [74] G. Von Pfingsten, K. Hameyer, and D. Paul. Influence of axial mechanical stress on the magnetic properties of non-oriented electrical steel. In *2016 6th International Electric Drives Production Conference, EDPC 2016 - Proceedings*, pages 193–200. IEEE, 2016.
- [75] G. Von Pfingsten, S. Steentjes, A. Thul, T. Herold, and K. Hameyer. Soft magnetic material degradation due to manufacturing process: A comparison of measurements and numerical simulations. In *2014 17th International Conference on Electrical Machines and Systems, ICEMS 2014*, pages 2018–2024, 2014.
- [76] P. Vourna, A. Ktena, P. E. Tsakiridis, and E. Hristoforou. A novel approach of accurately evaluating residual stress and microstructure of welded electrical steels. *NDT and E International*, 71:33–42, 2015.
- [77] H. Wang and Y. Zhang. Modeling of Eddy-Current Losses of Welded Laminated Electrical Steels. *IEEE Transactions on Industrial Electronics*, 64(4):2992–3000, 2017.
- [78] H. Wang, Y. Zhang, and S. Li. Laser welding of laminated electrical steels. *Journal of Materials Processing Technology*, 230:99–108, 2016.
- [79] P. Weiss. L' hypothèse du champ moléculaire et la propriété ferromagnétique. *J. Phys. Theor. Appl.*, 6(1):661–690, 1907.
- [80] X. Xiong, S. Hu, K. Hu, and S. Zeng. Texture and magnetic property evolution of non-oriented Fe-Si steel due to mechanical cutting. *Journal of Magnetism and Magnetic Materials*, 401:982–990, 2016.
- [81] K. Yamazaki, H. Mukaiyama, and L. Daniel. Effects of multi-axial mechanical stress on loss characteristics of electrical steel sheets and interior permanent magnet machines. *IEEE Transactions on Magnetics*, 54(3):1–4, 2018.

- [82] X. Zhang, Q. Zhao, Z. Cai, and J. Pan. Effects of magnetic field on the residual stress and structural defects of ti-6al-4v. *Metals*, 10(1):1–12, 2020.
- [83] Y. Zhang, H. Wang, K. Chen, and S. Li. Comparison of laser and TIG welding of laminated electrical steels. *Journal of Materials Processing Technology*, 247(February):55–63, 2017.

